

**A Study of High Transverse Momentum
Direct Photon Production from Beryllium and Copper
Targets with 530 GeV/c Incident π^- and Proton Beams**

by

Eric Jon Prebys

Submitted in Partial Fulfillment
of the
Requirements for the Degree
DOCTOR OF PHILOSOPHY

Supervised by: Professor Frederick Lobkowicz

Department of Physics and Astronomy
College of Arts and Sciences

University of Rochester
Rochester, New York

1990

CURRICULUM VITAE

Eric Jon Prebys was born in South Bend, Indiana on April 4th, 1963, but does not remember this and considers his hometown to be Phoenix, Arizona, where he moved, along with his mother, when he was 2 years old. In 1979, after his sophomore year of high school, the author began attending Arizona State University in Tempe, where he majored in Physics with the help of a scholarship from the E. Blois du Bois Foundation. In 1982, he transferred to the University of Arizona, in Tucson, where he was partially supported by a scholarship from the Cubic Corporation. Upon losing his job at a local gas station, the author was hired by Dr. Kwan Wu Lai to help analyze data from a high energy physics experiment. This prompted him to chose high energy physics as a career. In 1984, the author graduated from the University of Arizona with a B.S. in Engineering Physics and began attending graduate school at the University of Rochester. For the last 6 years he has been involved with Fermilab experiment E706, primarily working with electronics. In the course of his graduate studies, the author received his M.A. in Physics (1985), and was supported for a time by the Sproull Fellowship (1984-86) and the Messersmith Fellowship (1986-87).

Acknowledgements

There are many people involved at all levels with an experiment of this size, so I'll apologize in advance to those who I will almost certainly slight in this all-too-brief section.

First and foremost, I would like to thank my fellow graduate students and post-docs on E706, the people who worked long and hard to make this experiment a reality. In this category, George Ginther deserves singular mention, for devotion above and beyond the call of duty in all facets of the experiment. I'm personally grateful to Bill Desoi for providing many illustrations and compiling much technical information. In addition to being dedicated and hard working, I'll always remember this as a very enjoyable group to be around, both in and out of the lab.

My thesis advisor, Fred Lobkowicz, has been a well spring of information, assistance, and guidance throughout my graduate career. In addition, Rochester professors Tom Ferbel and Paul Slattery have always maintained a high profile in the experiment as a whole, as well as always being very helpful on the personal level.

It has become customary to thank Betty Cook in all graduate theses, but this should not give anyone the impression that it is not sincere in every case. In the same breath, all students of Fred Lobkowicz owe thanks to Betty Bauer. Without the help of these two people in sheltering me from cold bureaucratic realities, I certainly would have starved and/or been expelled long before now.

Over the years, we have received much technical assistance from people whose names will not appear on any publications. Bud Koecher, Bud Dickerson, Gene Olsen, Kevin Jenkins, Tom Haelen, Ernie Buchanan, and Larry Kuntz are a few of the names that are high on my own list, but there have been many others too numerous to mention here.

While on the subject of unsung heroes, we all owe a debt of gratitude to the

American taxpayer, who foots the lion's share of the bill for scientific advancement*.

I am eternally grateful to the Fox Valley Folk Music Society for holding square dances once a month at the Fermilab Village Barn. It is at one of these that I had the good fortune to meet Debbie Swanson, whom I will soon marry. I would like to thank her for her patience, understanding, and hard work over the last few difficult months. In addition to diligently proofreading thesis chapters and making wedding arrangements, she has been a source of personal strength without which I would certainly have gone crazy.

Last but definitely not least, I wish to dedicate this thesis to my mother, Janet Prebys, for her love and support over the years, and for never once pressuring me to get a real job.

* I have been supported by a grant from the N.S.F. (National Science Foundation) during most of my graduate studies. The experiment has been funded both by the N.S.F. and the D.O.E. (Department of Energy).

Abstract

Single photon production has been studied using 530 GeV/c hadronic beams incident on nuclear targets. Data were collected during the 1987-88 run of experiment 706 (E706) at Fermilab*, which employed a large liquid argon sampling calorimeter. Incident π^- beam was used to measure inclusive direct photon cross-sections from beryllium and copper targets, in the transverse momentum (p_T) range $3.5 < p_T < 10$ GeV/c. An incident proton beam was used to measure inclusive direct photon cross-sections from copper and beryllium targets in the range $4.25 < p_T < 10$ GeV/c. These cross-sections are presented, averaged over the rapidity interval $-.7 < y < .7$. The ratio of direct photon production to π^0 production is measured. The dependence of the direct photon cross-section on atomic number (A) and beam sign is investigated. Results are compared both to previous experiments and to theoretical predictions.

* Fermi National Accelerator Laboratory

Table of Contents

Curriculum Vitae	ii
Acknowledgements	iii
Abstract	v
Table of Contents	vi
Figure Captions	viii
Table Captions	xiii
1. Introduction	1
1.1 Physics Motivation	1
1.2 Overview of E706	1
1.3 Units and Conventions	2
1.4 Structure of this Thesis	2
2. Background and Motivation	4
2.1 Hadronic Interactions	4
2.2 Direct Photons	8
2.3 Experimental Considerations	10
2.4 Other Experiments	15
2.5 Goals of E706	16
3. Experimental Setup	19
3.1 Electromagnetic Liquid Argon Calorimeter (EMLAC)	19
3.2 The Hadronic Liquid Argon Calorimeter (HALAC)	31
3.3 The Gantry	33
3.4 The Forward Calorimeter (FCAL)	37
3.5 The Tracking System	39
3.6 The Target	42
3.7 Beamline and Cerenkov Detector	43
4. Instrumentation	49
4.1 The RABBIT System	49
4.2 LAC Amplifiers (LACAMPs)	50
4.3 E706 RABBIT Configuration and Usage	58

4.4 Tracking System	59
4.5 Data Acquisition	60
5. The Experimental Trigger	63
5.1 Principle	63
5.2 Image Charge	64
5.3 The p_T System	66
5.4 Trigger Logic	70
6. Event Reconstruction	74
6.1 Overview	74
6.2 Electromagnetic Reconstruction	75
6.3 Charged Track Reconstruction	80
7. Analysis	84
7.1 Data Selection	84
7.2 Muon Bremsstrahlung	86
7.3 Quality and Fiducial Cuts	92
7.4 $\gamma\gamma$ Mass Spectrum	94
7.5 Event Simulation	96
7.6 Effect of Cuts	97
7.7 Trigger Efficiency	99
7.8 Single Photon Cross-Section	102
7.9 π^0 Cross-section	108
7.10 Direct Photon Background	111
8. Results	123
8.1 Direct Photon Cross-Section	123
8.2 Systematic Errors	134
8.3 Nuclear Dependence	135
8.4 Beam Dependence	136
8.5 Comparison with Other Experiments	136
8.6 Comparison with QCD	144
9. Summary	150
References	152

FIGURE CAPTIONS

1)	Electron scattering in QED.....	5
2)	QCD concept of hadronic interactions.....	8
3)	Lowest order direct photon processes.....	9
4)	Conversion method of direct photon study. Statistically, π^0 's are more likely to have at least one pair conversion in the absorber material than are single photons.	13
5)	Some examples of quark bremsstrahlung as a source of single photons. In the first case, no high- p_T photons are expected, while in the second, high- p_T photons should be accompanied by jets.	15
6)	M-West detector hall.....	20
7)	Principle of liquid argon calorimetry.....	22
8)	Structure of the EMLAC.....	23
9)	EMLAC cell.....	25
10)	Signal summing within the EMLAC. Signals from each quadrant were summed to form front and back sections, each with four separate views.	26
11)	EMLAC readout boards.....	27
12)	Front-back separation as an aid to di-photon resolution. Showers will tend to have a narrower profile in the front section of the calorimeter. This can help to resolve di-photons which might otherwise coalesce.	28
13)	The hadronic calorimeter. Steel "Zorba Plates" acted as absorber material. Noninteracting beam passed through the beam hole, shown in the front view (left).	32
14)	HALAC readout cell, or "cookie".....	33
15)	HALAC pad configuration. Pads from the individual cookies were summed to form front and back towers.	34
16)	The LAC gantry.....	35
17)	The forward calorimeter.....	38

18) The SSD system.....	40
19) M-West secondary beamline. Beamline devices are represented by their optical equivalents.	44
20) E706 Cerenkov detector.	47
21) Cerenkov detector pressure curves. The contribution from the individual beam particle types is indicated.	47
22) Hadron shield. A removable central blade allowed calibration of the LAC.	48
23) Block diagram of a LACAMP module. Each module handled 16 LAC channels, providing pulse height and time-of-arrival information, as well as calibration circuitry.	52
24) Schematic of single LACAMP channel.	53
25) LACAMP EVENT sequence. In this case, one event occurs which does not satisfy the experimental trigger requirements. Shortly thereafter, a second event comes which does satisfy the trigger.	54
26) TVC Channel.....	57
27) E706 Data Acquisition System	61
28) The effect of image charge.....	65
29) p_T summing within one EMLAC octant. Energy depositions were weighted according their value of $\sin(\theta)$, so as to represent p_T .	67
30) Local p_T module. These modules produced p_T signals for groups of 8 and 32 strips.	68
31) Local discriminator module. These modules detected localized deposition of p_T within the EMLAC.	69
32) Summed p_T signal using only right-sign pulses. Notice that image charge is still an issue.	70
33) Scintillation counter configuration	71
34) TVC distributions for non- μ (a) and μ (b) events.	88
35) Concept of photon "directionality". The relative r positions of showers in the front and back of the EMLAC are used to flag muon bremsstrahlung.	89

- 36) Photon directionality vs. p_T . No cuts have been applied to this plot. The muon bremsstrahlung events are clearly visible in the band with directionality greater than .4 cm. 90
- 37) Photon directionality vs. TVC time. The lines indicate the experimental cuts which have been placed on these variables. 91
- 38) Photon directionality vs. p_T . In this case, all direct photon cuts beside directionality have been applied. 93
- 39) Two photon mass spectrum for all photon pairs falling within triggering octants. Entire data sample is represented. 95
- 40) *Single-Local* trigger turn-on curve for a typical octant. 101
- 41) Illustration of a direct photon event. The dashed line represents the direct photon candidate. The lengths of the lines indicates the relative magnitude of the particle momenta projected onto the X-Y plane. 104
- 42) Cross-section for single photons from π^- incident on beryllium. At this point no background subtraction has been done. 107
- 43) π^0 asymmetry. Distributions are shown for the mass region (a) and the sideband region (b) separately. The dotted line on the subtracted plot (c) shows the present asymmetry cut. 109
- 44) π^0 invariant cross-section as measured in E706. 112
- 45) π^0 asymmetry distribution. The points represent the measured asymmetry distribution for a sample of the data. The dashed line is the asymmetry distribution predicted by Monte Carlo. Detection efficiency corrections have been applied to both. 115
- 46) Ratio of single photons to π^0 's. Background expected from misidentified π^0 's and η 's is indicated. 116
- 47) Time distribution for photons which formed a π^0 mass with an asymmetry less than .75. The p_T cut is on the individual photon p_T . All direct photon cuts have been applied to this distribution. 118
- 48) Time distribution for photons which did not combine with any other photon to form a π^0 mass. 119

49) Time profile for muon induced events. A high directionality is required to select muons. The veto wall cut has been imposed to insure an unbiased time distribution. This has the unfortunate effect of reducing statistics.	121
50) Time profile for high- p_T photons. Tails are consistent with tails from π^0 photons, indicating negligible muon contamination.	122
51) Ratio of the cross-section for $\pi^- + Be \rightarrow \gamma + X$ to the cross-section for $\pi^- + Be \rightarrow \pi^0 + X$.	124
52) Direct photon inclusive invariant cross-section per nucleon for π^- beam on beryllium.	125
53) Ratio of the cross-section for $\pi^- + Cu \rightarrow \gamma + X$ to the cross-section for $\pi^- + Cu \rightarrow \pi^0 + X$.	126
54) Direct photon inclusive invariant cross-section per nucleon for π^- beam on copper.	127
55) Ratio of the cross-section for $p + Be \rightarrow \gamma + X$ to the cross-section for $p + Be \rightarrow \pi^0 + X$.	128
56) Direct photon inclusive invariant cross-section per nucleon for proton beam on beryllium.	129
57) Ratio of the cross-section for $p + Cu \rightarrow \gamma + X$ to the cross-section for $p + Cu \rightarrow \pi^0 + X$.	130
58) Direct photon inclusive invariant cross-section per nucleon for proton beam on copper.	131
59) Nuclear dependence of direct photon production. The ratio of the invariant cross-section per nucleon from a copper target to that from a beryllium target is shown in (a) for incident π^- and (b) for incident proton. Assuming a scaling of the form A^α , the equivalent α representations are shown in (c) and (d) respectively.	137
60) Comparison of direct photon cross-sections between incident π^- and incident proton.	138
61) Comparison of π^- data with previous results.	139
62) Comparison of proton data with previous results.	140
63) Comparison of direct photon production from incident π^- . Cross-sections have been scaled in an attempt to cancel \sqrt{s} dependence.	142

- 64) Comparison of direct photon production from incident proton. Cross-sections have been scaled in an attempt to cancel \sqrt{s} dependence. 143
- 65) QCD predictions for $\pi^- + Be \rightarrow \gamma + X$ with arbitrary scaling ($Q = .5p_T$). 146
- 66) QCD predictions for $p + Be \rightarrow \gamma + X$ with arbitrary scaling ($Q = .5p_T$). 147
- 67) QCD predictions for $\pi^- + Be \rightarrow \gamma + X$. In this case, the Q^2 dependence has been determined using PMS optimization. 148
- 68) QCD predictions for $p + Be \rightarrow \gamma + X$. In this case, the Q^2 dependence has been determined using PMS optimization. 149

TABLE CAPTIONS

1: Quark generations.....	5
2: Quark content of common hadrons.....	5
3: A summary of direct photon experiments to date. Incident beam energy is shown for fixed target experiments. Center of mass (\sqrt{s}) energy is shown for collider experiments.	17
4: Strip numbering in the EMLAC. r positions are given at the front the EMLAC. ϕ positions are given relative to the quadrant boundary.	29
5: E706 tracking modules.....	42
6: Beam content for 530 GeV secondary beam.....	46
7: Trigger threshold setting by run number.....	72
8: Data sample from the E706 '87-'88 run which has been considered in this analysis. This represents about 350 tapes of data.	85
9: High- p_T data streams. Events were categorized according to the highest p_T photon or di-photon.	85
10: Data sample available for direct photon analysis.....	86
11: Number of events surviving each successive event cut.	98
12: Number of photons surviving each successive photon cut.	98
13: Corrections applied to observed single photons to compensate for losses due to cuts.	100
14: Final reaction dependent corrections.....	106
15: Direct photon cross-sections for incident π^- beam. The background due to π^0 and η decays has been subtracted.	132
16: Direct photon cross-sections for incident proton beam. The background due to π^0 and η decays has been subtracted.	133
17: Dependence of direct photon production on beam type.....	136

1. Introduction

1.1 PHYSICS MOTIVATION

A detailed discussion of the physics of interest to E706 is found in chapter 2. Put very simply, the experiment was designed to study “direct photons”, that is, photons which are produced directly in interactions between hadrons (protons, neutrons, etc.), as opposed to photons which are decay products of other particles. This is interesting because, for reasons which will be explained, most high-energy hadronic interactions give rise to very complicated events containing *jets* of particles. In contrast, direct photons provide a method of using single particles to probe fundamental interactions between the constituents of hadrons. These photons are expected to be produced with relatively more transverse momentum, or p_T , than most other products of hadronic interactions. It is therefore the study of these *high- p_T* photons to which E706 has been optimized.

1.2 OVERVIEW OF E706

The experimental setup will be discussed in great detail in chapter 3. E706 is a fixed target experiment located in the Meson West (M-West) detector hall at the Fermi National Accelerator Laboratory (Fermilab). This hall is serviced by a beamline which can deliver positive (p, π^+, K^+) or negative (π^-, K^-, \bar{p}) beams of up to 800 GeV.

The centerpiece of the E706 spectrometer is a large electromagnetic calorimeter to study the photons themselves. This calorimeter has very good energy and position resolution to distinguish single photons from multiple photon decays. Charged tracking is provided, including a precision system for reconstructing vertices in the experimental target. To complete the spectrometer, hadron calorimetry is provided, both for neutral hadrons, which would not be detected by the tracking system, and for particles produced too close to the beam direction to be resolved by the other spectrometer components.

1.3 UNITS AND CONVENTIONS

The following conventions will apply unless specified to be otherwise.

All mechanical specifications will be in cgs units. Theoretical equations will use high energy physics units (i.e. $c = \hbar = 1$). Following this convention, all particle masses and energy will be expressed in eV (KeV, MeV, etc.). For the sake of convention, momenta will usually be expressed in GeV/c; however GeV should be considered equivalent in this context.

Cross sections will always be quoted in picobarns ($\text{pb} \equiv 10^{-36} \text{ cm}^2$) per nucleon. In the case of nuclear targets, the measured cross section per nucleus will be divided by the atomic weight to obtain this form.

Coordinates will be in terms of a right-handed system, with its origin near the target, the Z -axis roughly aligned with the incident beam direction, the Y -axis vertical, and the X -axis horizontal. Coordinates r and ϕ will be used to express nominal positions within the electromagnetic calorimeter, uncorrected for alignment.

The terms "upstream" and "downstream" will frequently be used to describe relative positions within the detector hall. These refer to directions in relation to the incoming beam of particles. Downstream means in the direction of the beam, and upstream means opposite the direction of the beam.

1.4 STRUCTURE OF THIS THESIS

Because this is a study of direct photons, the experimental apparatus can in some sense be viewed as the electromagnetic calorimeter and "everything else"*. Some information from the tracking system will also be used in the analysis. A brief discussion of the hadronic calorimetry will be included for the sake of completeness, but it is not relevant to this study.

* Admittedly, this somewhat ethnocentric view is rooted in part in the author's personal involvement with this device.

Theoretical motivation and background will be given in chapter 2. This chapter will also discuss previous direct photon experiments, and the specific contributions E706 can make to the body of knowledge. Chapter 3 will describe E706 spectrometer, including the theory of operation of the electromagnetic calorimetry. The fourth chapter covers the instrumentation of the electromagnetic calorimeter and tracking system. Chapter 5 describes the experimental *trigger*, i.e. the hardware system for selecting physics of interest. Offline reconstruction of events is covered in chapter 6. Again, this will focus primarily on the reconstruction of photons. The details of the analysis are covered in chapter 7. Much attention will be given to the π^0 signal, both as an indicator of detector performance and as a source of direct photon background. Finally, the direct photon cross-sections will be presented in chapter 8. Comparisons will be made, both to theoretical predictions, and to existing experimental data. Chapter 9 will summarize and present conclusions.

2. Background and Motivation

2.1 HADRONIC INTERACTIONS

It has long been known that except at low energies, hadrons (protons, pions, etc.) could not be treated as pointlike particles but rather as having structure. Thus, interactions at energies of current interest (>10 GeV in center-of-mass frame) must be viewed as actually taking place between the sub-particles (historically called “partons”) out of which the familiar particles are composed.

The generally accepted Standard Model describes the structure of hadrons in terms of Quantum ChromoDynamics (QCD). This model was inspired by Quantum ElectroDynamics (QED), which has been very successful in describing electromagnetic interactions. In QED, the electromagnetic force is mediated by photons. Figure 1 shows an interpretation of simple electron scattering in this model. In this case the intermediate photon couples to the electrons each with an amplitude $\sqrt{\alpha}$, where α is the *fine structure constant* ($\approx \frac{1}{137}$). Any charged particle may interact via the electromagnetic force.

In QCD, there are six spin- $\frac{1}{2}$ fermions called “quarks”, arranged in three “generations”, as shown in table 1. These quarks interact via the “strong” force, which is mediated by vector bosons called “gluons”. The charge is now the so-called “color charge”, having of course nothing to do with actual color. Quarks exist in three colors: *red*, *green*, and *blue*. For each quark, there exists an anti-quark, with opposite electric charge and color. The gluons exist in states of mixed color and anti-color, forming an SU(3) octet. The quarks combine to form “colorless” SU(3) singlet particles called “hadrons”. Put simply, this means either three quarks of different colors combine, or a quark and an anti-quark combine. These form classes of particles known as “baryons” and “mesons” respectively. Table 2 shows the quark content of some of the familiar hadrons.

This theory has had much qualitative success in explaining the observed spectrum of hadrons; however, several things complicate actual quantitative predictions. For one, because gluons themselves carry color, they can interact

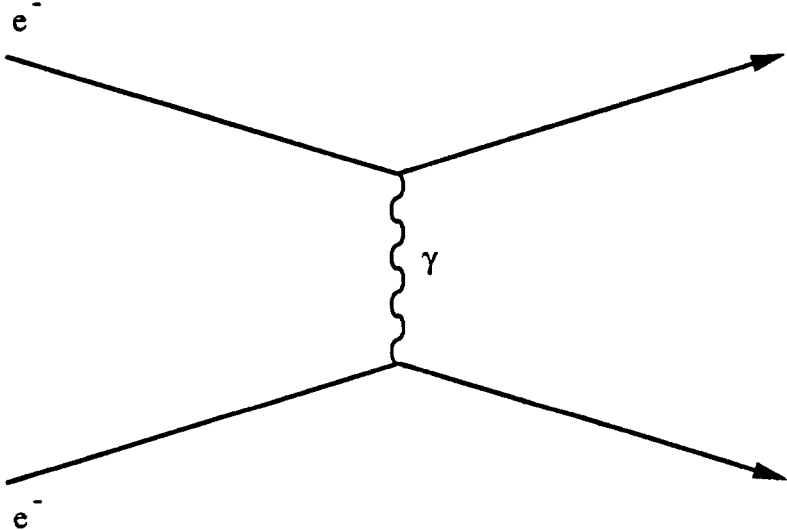


Figure 1 – Electron scattering in QED.

Charge	Quarks		
$+2/3e$	u (up)	c (charm)	t (top)
$-1/3e$	d (down)	s (strange)	b (bottom)

Table 1 – Quark generations.

Particle	p	n	π^+	π^-	K^+	K^-
Quark Content	uud	udd	$u\bar{d}$	$\bar{u}d$	$u\bar{s}$	$\bar{u}s$

Table 2 – Quark content of common hadrons.

with other gluons. This results in an effective force so strong that naked, or unaccompanied, color cannot exist on a time scale which may be studied. This has two consequences. The first, termed “confinement”, is that stable particles must be colorless. This is just the restatement of the fact that quarks and

gluons must combine in SU(3) singlet states. The other consequence is called “hadronization”. This means that if a reaction does impart enough energy to separate a hadron into colored fragments, these fragments will interact with the virtual “sea” particles to ultimately form colorless objects. This results in a *jet* of particles. Neither confinement nor hadronization is currently understood in any fundamental way.

The coupling strength in QCD is given by α_s , which is a function of the momentum transfer (Q^2). This “running coupling constant” is typically expanded in terms of $\log(Q^2)$, with the first order, or “leading log” value given by^[1]

$$\alpha_s(Q^2) = \frac{\alpha_s(\Lambda^2)}{1 + \frac{\alpha_s(\Lambda^2)}{4\pi}(11 - \frac{2}{3}n_f)\log(Q^2/\Lambda^2)} \quad (2.1)$$

where n_f is the number of quark flavors kinematically available to the reaction and Λ is a scale factor required by the expansion.* The implication of equation (2.1) is that as $Q^2 \rightarrow \infty$, $\alpha_s \rightarrow 0$, i.e. it becomes reasonable to expand reactions in powers of α_s . This implies that at high enough energy, the effects of confinement may be ignored and reactions may be considered as simple interactions between constituent partons. This phenomenon is known as “asymptotic freedom”.

Consider a general hadronic interaction ($A + B \rightarrow C + X$), illustrated in figure 2, where A and B are interacting hadrons, C is a specific product of the reaction, and X is anything else which is produced in the reaction. The invariant cross-section for this process may be written in terms of the contributing sub-processes as

$$E_C \frac{d\sigma}{d^3p_C}(AB \rightarrow CX) = \sum_{abcd} \int dx_a dx_b dz_c G_{a/A}(x_a, Q^2) G_{b/B}(x_b, Q^2) \times D_{C/c}(z_c, Q^2) \frac{\hat{s}}{z_c^2 \pi} \frac{d\sigma}{dt}(ab \rightarrow cd) \delta(\hat{s} + \hat{t} + \hat{u}) \quad (2.2)$$

* It is believed that if the expansion of α_s could be done to all orders, the result would be independent of the choice of Λ ; however, because of the complexity of such a task, present experiments must choose a value which best fits the data.

Here, the sum is over the constituent partons a and b of the original hadrons A and B , respectively, and over all possible products c and d which could result from their interaction. x_i refers to the fraction of the momentum of hadron I which is carried by parton i . $G_{i/I}$ is number distribution of parton i within hadron I at a given momentum fraction and Q^2 value. Note that because of singularities at $x_i = 0$, the parton distributions are usually discussed in terms of “structure functions” $F_{i/I} (\equiv x_i G_{i/I})$. The “fragmentation function” $D_{I/i}$ is the probability that a colored parton i will hadronize to produce the particle I with a fraction x_i of the original parton momentum. The $d\sigma/d\hat{t}$ term is the cross-section for the actual parton diagram. \hat{s} , \hat{t} , and \hat{u} are the Mandelstam kinematic variables, defined as

$$\begin{aligned}\hat{s} &= (p_a + p_b)^2 \\ \hat{t} &= (p_a - p_c)^2 \\ \hat{u} &= (p_a - p_d)^2\end{aligned}\tag{2.3}$$

where p_i is the four vector momentum of parton i . The Q^2 dependence of the structure functions and fragmentation functions gives rise to “scaling violations”. Stated simply, this means that the parton distribution that a gluon “sees” depends on the amount of momentum it is transferring.

One method of studying the fundamental QCD reactions is offered by the field of “jet physics”, wherein one tries to measure the total momentum of the jet of particles produced during the fragmentation of the original parton. This could also lead to a measurement of the fragmentation function if all the particles in the jet could be identified and their individual momenta measured. Unfortunately, beyond the technical difficulties of such studies, there is the theoretical uncertainty as to how well the kinematic properties of the jet mimic those of the original parton. Also, because of the non-abelian nature of the strong force, the number diagrams which may contribute becomes very large with increasing orders of α_s . Nevertheless, the field of jet physics is very interesting and is currently an active area of research.

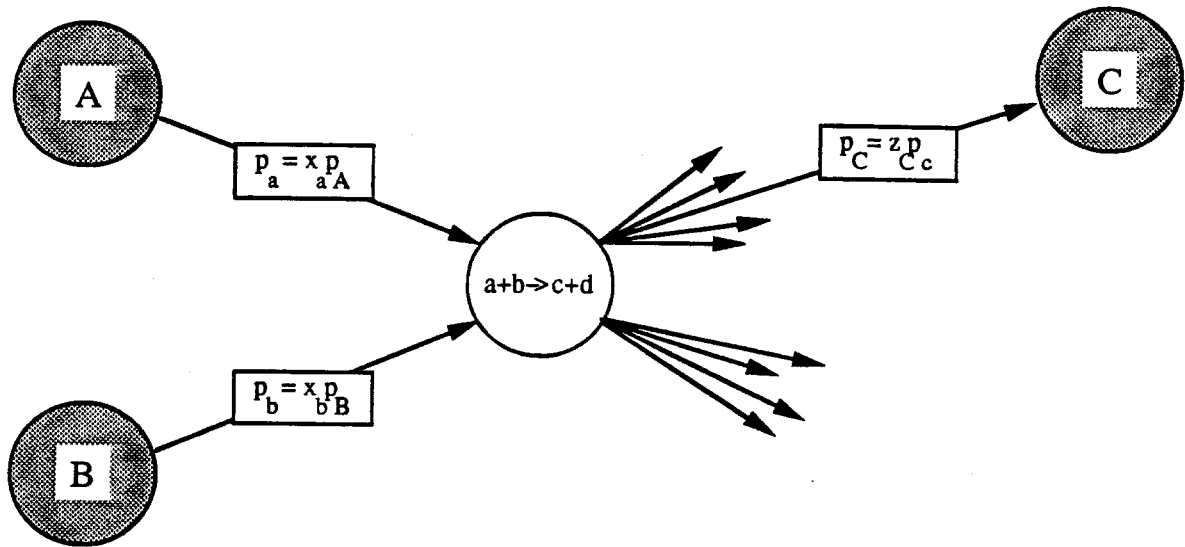


Figure 2 – QCD concept of hadronic interactions.

2.2 DIRECT PHOTONS

Because quarks carry an electric charge, they also interact via the electromagnetic force. This means that QCD interactions may produce photons *directly* rather than as the decay products of other particles. These direct photons provide an interesting and promising method of studying QCD. First of all, photons do not carry electric charge and so cannot interact directly with one another. This greatly reduces the number of subprocesses which may contribute. Lowest order direct photon production ($O(\alpha\alpha_s)$) can only arise from two diagrams, shown in figure 3. The first is called the Compton Diagram because it is analogous to Compton scattering between photons and electrons. The second is called the Annihilation Diagram for obvious reasons.

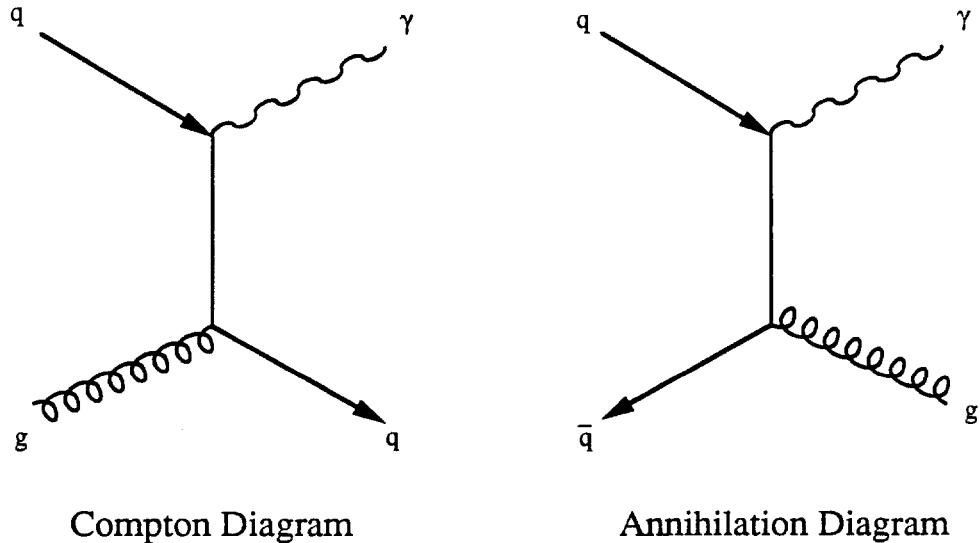


Figure 3 – Lowest order direct photon processes.

By far the main attraction of direct photon physics is, however, the fact that photons do not carry the color charge and so do not hadronize. This means that rather than being forced to work backward from a jet of particles, one can actually study the product of a QCD interaction directly. In studying the reaction $A + B \rightarrow \gamma + X$, equation (2.2) becomes

$$E_\gamma \frac{d\sigma}{d^3 p_\gamma} (AB \rightarrow \gamma X) = \sum_{abd} \int dx_a dx_b G_{a/A}(x_a, Q^2) G_{b/B}(x_b, Q^2) \times \frac{\hat{s}}{\pi} \frac{d\sigma}{d\hat{t}} (ab \rightarrow \gamma d) \delta(\hat{s} + \hat{t} + \hat{u}) \quad (2.4)$$

where the fragmentation function is now removed. As mentioned earlier, to lowest order the sum is over just two reactions, with cross-sections given by^[2]

$$\frac{d\sigma}{d\hat{t}} (qg \rightarrow q\gamma) = -\frac{\pi \alpha \alpha_s}{3 \hat{s}^2} e_q^2 \frac{\hat{u}^2 + \hat{s}^2}{\hat{u}\hat{s}} \quad (2.5)$$

$$\frac{d\sigma}{d\hat{t}} (\bar{q}q \rightarrow g\gamma) = \frac{8\pi \alpha \alpha_s}{9 \hat{s}^2} e_q^2 \frac{\hat{u}^2 + \hat{t}^2}{\hat{u}\hat{t}} \quad (2.6)$$

The major drawback to direct photon studies is the low rate relative to jet production. The cross-section is reduced by approximately α/α_s for every contributing diagram in which a photon replaces a gluon. This combines with the smaller number of contributing diagrams to make the relative rate much lower. This necessitates either recording (and rejecting) a very large amount of data, or implementing an experimental trigger which will favor this type of physics.

2.3 EXPERIMENTAL CONSIDERATIONS

The first consideration is of course how to study such physics. One can take advantage of the fact that the direct photons carry the entire energy of the original reaction, whereas in a jet the energy must be divided amongst the constituent particles. Fragmentation functions have been measured to fall off rapidly with increasing z . Thus, if jet production is assumed to behave similarly to photon production, both falling off with increasing Q^2 , then it is high- Q^2 reactions which would tend to increase the ratio of direct photons to other single particles. Experimentally, such reactions manifest themselves most clearly in the *high- p_T* region, where p_T is the component of momentum perpendicular to the collision path of the two particles. This is primarily because p_T is Lorentz invariant along this path. The parallel component of the momentum is more sensitive to boosts arising from differences in parton momentum between the two hadrons than to the actual Q^2 transfer of the reaction. It is in the region of $p_T > 4 \text{ GeV}/c$ where the first unambiguous evidence for direct photons has been seen^[3]. Thus, it is desirable to design a detector which is optimized to study single photons in this region.

The fact that photons are neutral means that they can only be studied using some sort of *calorimetry*, wherein they interact with matter, producing an electromagnetic *shower* and ultimately depositing all of their energy. There are many methods for doing electromagnetic calorimetry. The method used must be tailored to the priorities of a given experiment.

Because direct photons are produced at relatively low rate, the issue of experimental background is very important. Various external effects can cause background in individual experiments, but there are several types of "physics" background which must be considered in the design of any direct photon experiment.

One very large source of background is expected to come from the π^0 meson, which decays primarily (99%) to $\gamma\gamma$ ^[4] and is copiously produced in hadronic interactions. Because of the low mass of the π^0 , the decay photons are usually produced with a very small opening angle, making them difficult to resolve. There are two experimental techniques for handling this problem, which will now be discussed.

The first, known as the "conversion method", relies on the fact that photons can *pair convert* into e^+e^- pairs in the presence of matter. If a photon passes through some thickness of material, the probability that it will not pair convert is given by

$$P_{NC}^\gamma = \exp\left(-\frac{7}{9}X\right) \quad (2.7)$$

where X is the thickness of the material in radiation lengths. If the photons from a π^0 pass through the same sheet, the probability that neither one of them convert is therefore

$$\begin{aligned} P_{NC}^{\pi^0} &= (P_{NC}^\gamma)^2 \\ &= \exp\left(-\frac{14}{9}X\right) \end{aligned} \quad (2.8)$$

One can imagine an experiment such as the one shown in figure 4, consisting of a thin converter sheet, a hodoscope (detector of charged particles) and some sort of electromagnetic shower detector. Assuming that the shower detector has too coarse of a granularity to resolve two photons from a π^0 decay, then one can determine the relative content of single photons to di-photons statistically. Based on equations (2.7) and (2.8), the total number of showers which have have

at least one e^+e^- pair, as recorded by the hodoscope, is given by

$$N_{pair} = N_{\pi^0}(1 - P_{NC}^{\pi^0}) + N_{\gamma}(1 - P_{NC}^{\gamma}) \quad (2.9)$$

which means that if N_{tot} is the total number of observed showers, then the total number of single photons can be extracted as

$$N_{\gamma} = \frac{N_{tot}(1 - (P_{NC}^{\gamma})^2) - N_{pair}}{(P_{NC}^{\gamma} - (P_{NC}^{\gamma})^2)} \quad (2.10)$$

assuming that all showers are either from a single photon or a di-photon decay.

The advantage of the conversion method is that it is simple and relatively inexpensive to build such a detector, and several of the earlier experiments used this technique. One disadvantage is that because it is purely a statistical method, there is no way to differentiate between single and di-photons on the event level, so beyond simple counting it is difficult to say much about the differences between π^0 events and direct photon events. Also, if the converter is made thick enough to get a statistically significant number of e^+e^- pairs, then it will begin to degrade the resolution of the system by absorbing a large amount of energy before the shower counter.

The other method is known as the “Direct Method”. It involves building a detector capable of resolving as many of the photon pairs as possible, in an attempt to reject them and produce a “clean” direct photon sample. This has the advantage that it is now possible to say things about single photons versus di-photons on the event level. The disadvantage is that it requires a much finer grained detector than the conversion method, which necessitates more channels of electronics and more complex reconstruction algorithms. Also, because of the width of electromagnetic showers, this method favors putting the detector far away from the interaction to get the maximum photon separation. This would make the detector unmanageably large if any reasonable coverage were desired, so some sort of practical compromise must be reached. In addition, even with the best detectors it is virtually impossible to reconstruct all two-photon decays,

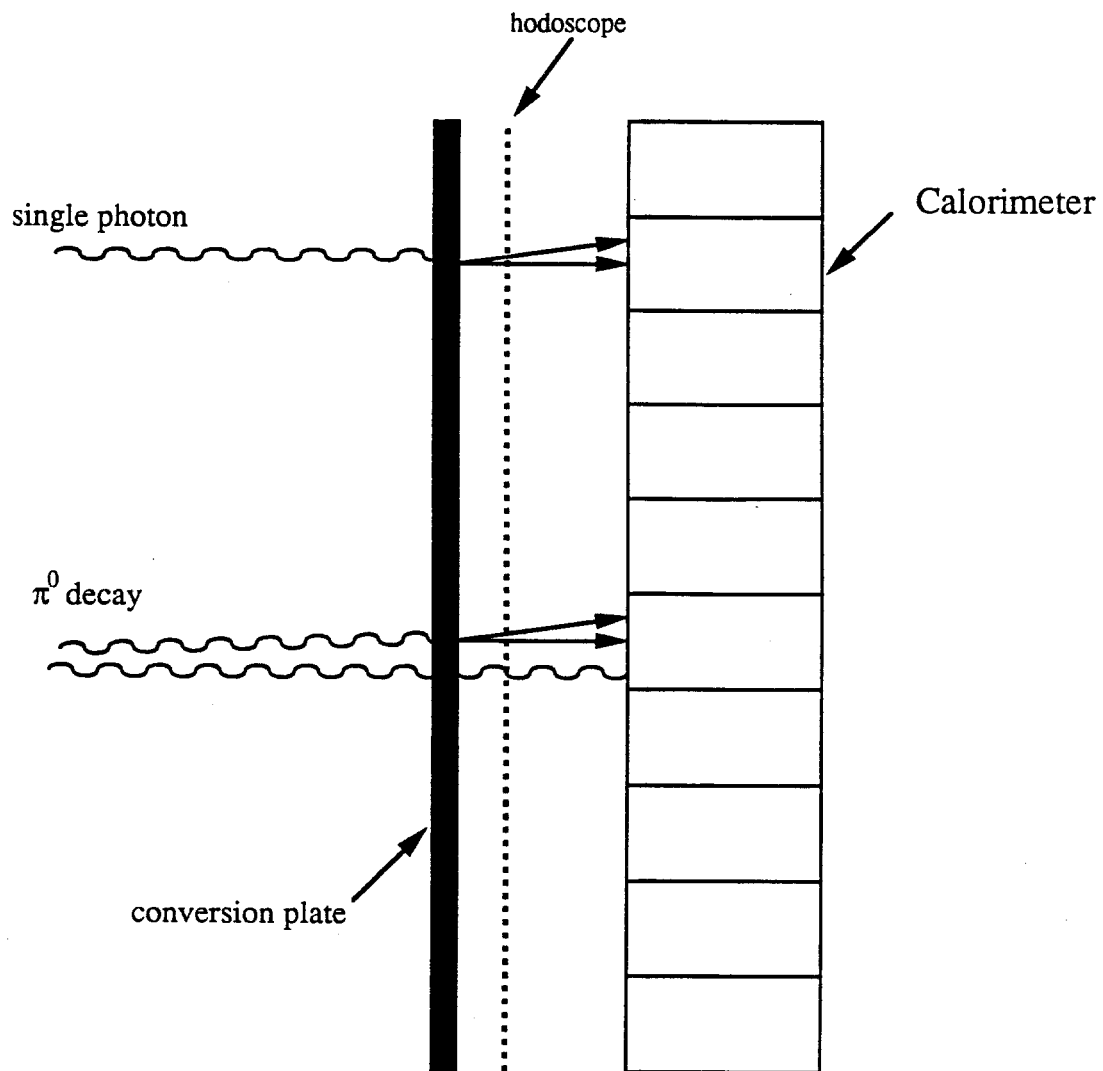


Figure 4 – Conversion method of direct photon study. Statistically, π^0 's are more likely to have at least one pair conversion in the absorber material than are single photons.

so ultimately some statistical correction must still be done. Nevertheless, this is seen as the only method of making truly precision measurements of direct photon properties, and it is this path that E706 has chosen.

After the π^0 , the next largest source of photons is expected to be the decay of the η meson, which decays to $\gamma\gamma$ with a branching ratio of .39^[5] and is produced at a rate of about 1/2 of the π^0 ^[6]. Fortunately, the higher mass of the η means that the decay photons are produced with a larger opening angle. This means that η 's can usually be identified even with the coarser calorimetry used for the conversion method. On the other hand, the larger opening angle also means that it is more likely that one of the photons from the decay will miss the detector entirely. Other decays also contribute, but because of much smaller production rates, these are usually not a factor at high- p_T .

Background may also come from particles other than photons. Electrons, for example, produce showers almost identical to photons. It is therefore desirable to have some sort of charged track detection so they may be identified. This track detection can also identify charged hadrons, but neutral hadrons might still be a problem, so some form of hadronic calorimetry would be useful. Beyond the issue of direct photon background, the additional information about charged particles and hadrons would be very useful in its own right, as it would provide information about direct photon event topology. A direct photon should usually be accompanied by at least one jet, resulting from the fragmentation of the accompanying parton in the final state. It would be very interesting to study these associated jets.

Photons may also be produced through *quark bremsstrahlung*, as illustrated in figure 5. This is a complex background to handle, as it does produce a single photon which, from the experimental standpoint, comes directly from the interaction. In the case shown in 5a, the bremsstrahlung photon should be produced more or less parallel to the incident parton, i.e. not at large p_T . In the second case, the highest p_T photons are expected to accompany the resulting jet. Thus, comparing photons which are isolated to those which are accompanied

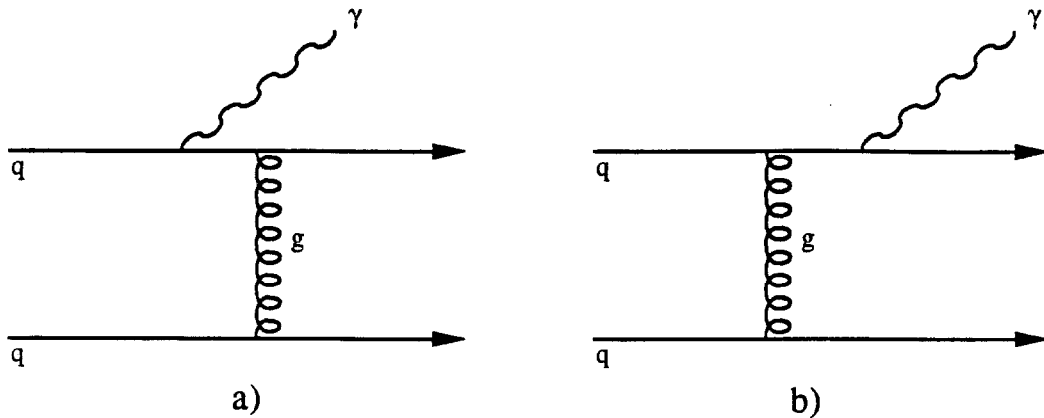


Figure 5 – Some examples of quark bremsstrahlung as a source of single photons. In the first case, no high- p_T photons are expected, while in the second, high- p_T photons should be accompanied by jets.

by other particles could give some measure of the bremsstrahlung component; however, the exact interpretation of such a comparison is very model dependent. For this reason, no attempt is made to distinguish bremsstrahlung photons from direct photons in this analysis. Likewise, no attempt is made to identify *higher twist* photons, or photons arising from coherent scattering of particles.

2.4 OTHER EXPERIMENTS

This is by no means a new field of study. It has aroused interest since the 1970's. Early experiments sought only to demonstrate evidence for the existence of direct photons. The first experiments to publish direct photon results were experiments R412^[7] and R107^[8], both performed at the CERN ISR. These experiments had many systematic problems and presented contradictory results,

but did spark interest in further study. More recently, several experiments at both CERN and Fermilab have published direct photons cross-section measurements, at \sqrt{s} values ranging from 19.4 GeV in fixed target experiments to 1.8 TeV at the Collider Detector at Fermilab (CDF). Table 3 gives summary information on major direct photon experiments. Of these experiments, E705, R110, CDF, and this experiment have not yet published final results.

2.5 GOALS OF E706

In light of all of the work which has been done, direct photon physics must be regarded as a mature field of study. Clearly any present generation experiment must be a dedicated, precision study. In this regard, E706 offers several new insights.

Most of the previous data have come either from $\sqrt{s} \approx 20$ GeV or $\sqrt{s} \approx 65$ GeV. With $\sqrt{s} = 31.6$ GeV, E706 bridges the gap between these two regimes.

This is one of the few experiments to use nuclear targets, and it is the first time that different targets have been used in a single experiment. Thus, nuclear effects may be studied. If one measures the cross-section per nucleus for two different targets a and b , the ratio may be parametrized as

$$\frac{\sigma_a}{\sigma_b} = \left(\frac{A_a}{A_b} \right)^\alpha \quad (2.11)$$

where σ_x is the cross-section per nucleus for target x and A_x is the atomic number. It is then interesting to study the behavior of α with p_T , target types, etc*. If direct photons are produced purely from hard scattering with nucleons, then one expects α to be close to 1, because it is the relative numbers of nucleons in each nucleus which determine the relative cross-sections. If, on the other hand, nuclear shadowing plays an important role, one expects α to be closer to 2/3, because the relative cross-sections are determined by the relative cross-sectional areas of the nuclei.

* This definition of α should not be confused with the previous definition, i.e. the electromagnetic coupling constant. This ambiguous usage of α results from historical convention.

Collaboration	P_{beam} GeV	\sqrt{s} GeV	Beam	Target
E95 ^[9]	200,300		p	Be
E629 ^[10]	200		p, π^+	C
NA3 ^[11]	200		p, π^\pm	C
NA24 ^[12]	300		p, π^\pm	H ₂
WA70 ^[13]	280		p, π^\pm	H ₂
E705 ^[14]	300		p, \bar{p}, π^\pm	L ₇
UA6 ^[15]		24.3	p, \bar{p}	p
R108 ^[16]		62.4	p	p
R110 ^[17]		63.0	p	p
R806 ^[18]		63.0	p	p
AFS ^[19]		53.0	\bar{p}	p
UA2 ^[20]		546,630	\bar{p}	p
UA1 ^[21]		546,630	\bar{p}	p
CDF ^[22]		1800	\bar{p}	p
E706	530		$p, \bar{p}, \pi^\pm, K^\pm$	C,Cu,Be

Table 3 – A summary of direct photon experiments to date. Incident beam energy is shown for fixed target experiments. Center of mass (\sqrt{s}) energy is shown for collider experiments.

It is interesting to compare direct photon production from various incident beam particles. By having several types of incident beam particles in the same experiment, E706 can hope to make such a comparison with a minimum of systematic uncertainty. For example, referring again to (2.5) and (2.6), we see that the contribution of the Compton diagram should be the same in $\pi^- p$ and $\pi^+ p$ reactions, while the annihilation term should be 8 times greater in $\pi^- p$ reactions. The difference comes from the difference in charge between u and d quarks and the larger number of u quarks in the proton (note that if an isoscalar target is used, this ratio is reduced to 4. Thus, one could in principle compare data from the two reactions to extract the separate diagrams. This over-simplified picture is of course complicated by higher order corrections.

In this analysis, cross-sections will be presented for direct photons produced by 530 GeV/c π^- and proton beams incident on beryllium and copper targets. Comparisons will be made between the two beam types, as well as between the different targets. Theoretical QCD predictions will be tested against the data. Also, comparisons will be made with existing direct photon data.

3. Experimental Setup

The E706 experimental spectrometer was divided into several subsystems, which will be described throughout this chapter. Figure 6 shows the relative positions of the various devices within the M-West hall. Also shown is the spectrometer for experiment E672, which ran concurrently with E706. As the E672 data had no relevance to this analysis, their spectrometer will not be discussed. Data from the E706 hadronic calorimeter and forward calorimeter were also not used in the analysis, but a short discussion of each is included for the sake of completeness. The final section of the chapter gives a description of the M-West beamline, which delivered beam to the detector hall. This beamline included a Cerenkov detector which determined beam particle type.

3.1 ELECTROMAGNETIC LIQUID ARGON CALORIMETER (EMLAC)

Because the purpose of E706 was the study of direct photons, the entire spectrometer was more or less designed around the electromagnetic calorimetry, which was provided by the EMLAC. For a detailed discussion of the factors which went into choosing liquid argon calorimetry and the determination of the EMLAC design parameters, the reader is referred elsewhere^[23]. Suffice to say that liquid argon calorimetry provided the most practical, affordable method of achieving the fine granularity, good energy resolution, and high rate capability necessary for this study.

Charge Collection

The principle of liquid argon calorimetry is illustrated in figure 7. When a charged particle passes through argon, it loses energy through ionization. This liberates a total amount of charge (Q_0) given by

$$Q_0 = \frac{E}{\epsilon} e \quad (3.1)$$

where E is the energy deposited, ϵ is the ionization potential of argon (≈ 13 eV), and e is the electron charge. If a voltage is applied, this liberated charge drifts

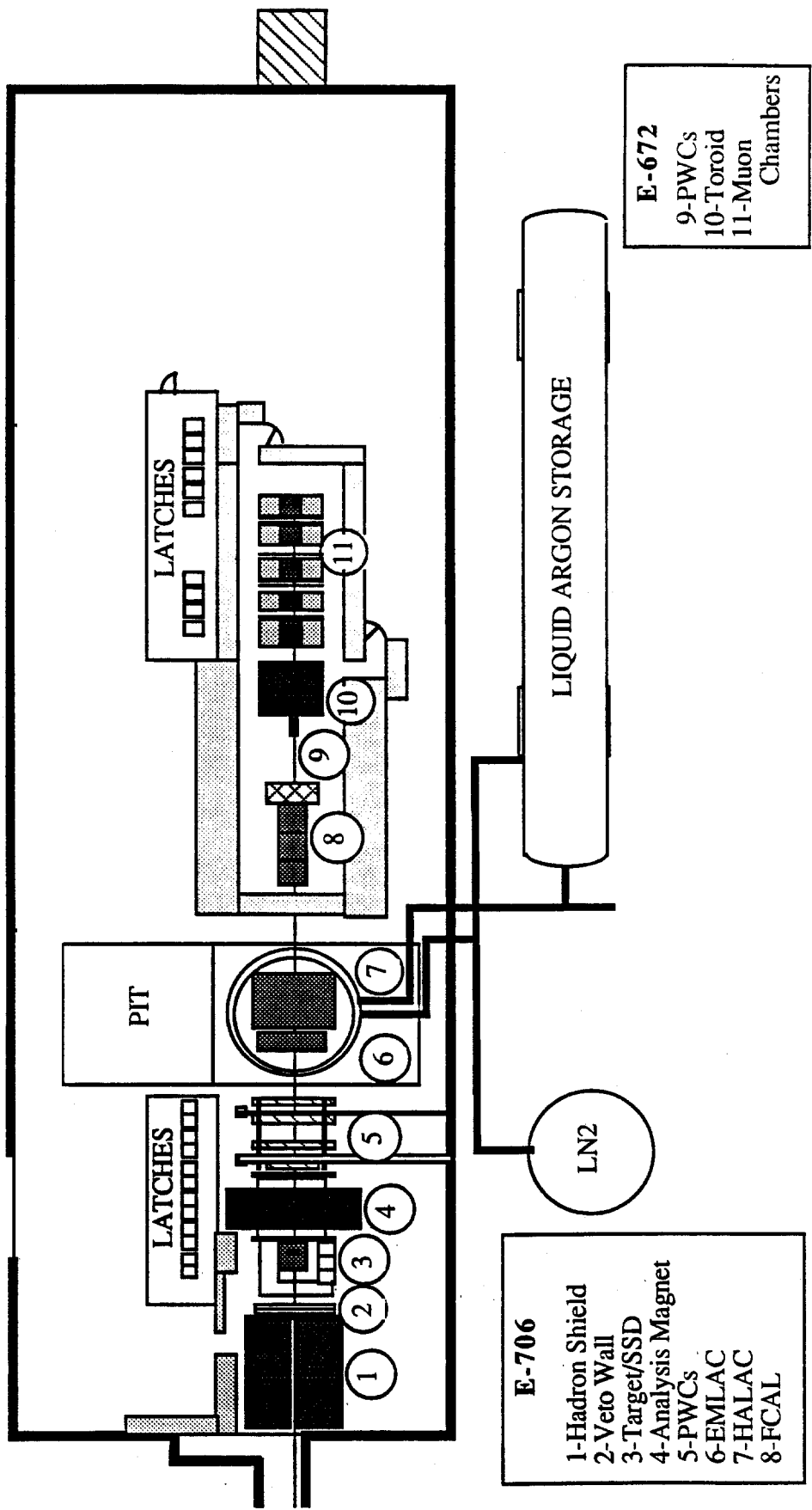


Figure 6 – M-West detector hall

toward one side of the gap. If one assumes a uniform distribution of charge and that none of the electrons are absorbed, then this induces a current between the anode and the cathode which is given by^[24]

$$\begin{aligned} I(t) &= Q_0 \frac{v_d}{d} \left(1 - \frac{v_d}{d} t\right) \quad ; t \leq \frac{d}{v_d} \\ &= 0 \quad ; t > \frac{d}{v_d} \end{aligned} \quad (3.2)$$

where v_d is the drift velocity, d is the gap width, and t is time. This means that the integrated charge is given by

$$\begin{aligned} q(t) &= Q_0 \frac{v_d}{d} \left(t - \frac{1}{2} \frac{v_d}{d} t^2\right) \quad ; t \leq \frac{d}{v_d} \\ &= \frac{Q_0}{2} \quad ; t > \frac{v_d}{d} \end{aligned} \quad (3.3)$$

Thus, one can measure the total amount of deposited energy with some sort of charge integration amplifier.

EMLAC Structure

The structure of the EMLAC is shown in figure 8. It was cylindrically shaped, with the axis along the beamline. The upstream face was roughly 9 m downstream of the target. There was a hole through the center of the EMLAC. This was because of the high particle flux produced at small angles relative to the beam. This left an active region from approximately 20 cm to 150 cm in radius.

For construction purposes, the EMLAC was divided into four functionally equivalent *quadrants*. Each quadrant was longitudinally divided into 33 *cells*. The cross section of a single cell is shown in figure 9. In downstream order, each consisted of a 2 mm thick lead sheet, a 1.6 mm thick copper-clad G-10 board*, a second 2 mm lead sheet, and a second copper-clad G-10 board. The first

* G-10 is a form of epoxy fiberglass which was used extensively in the construction of the LAC.

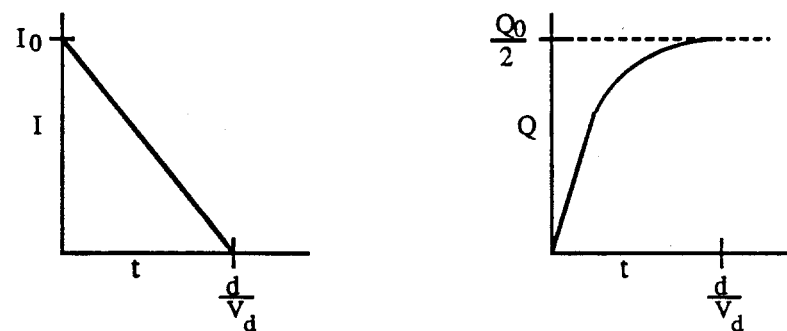
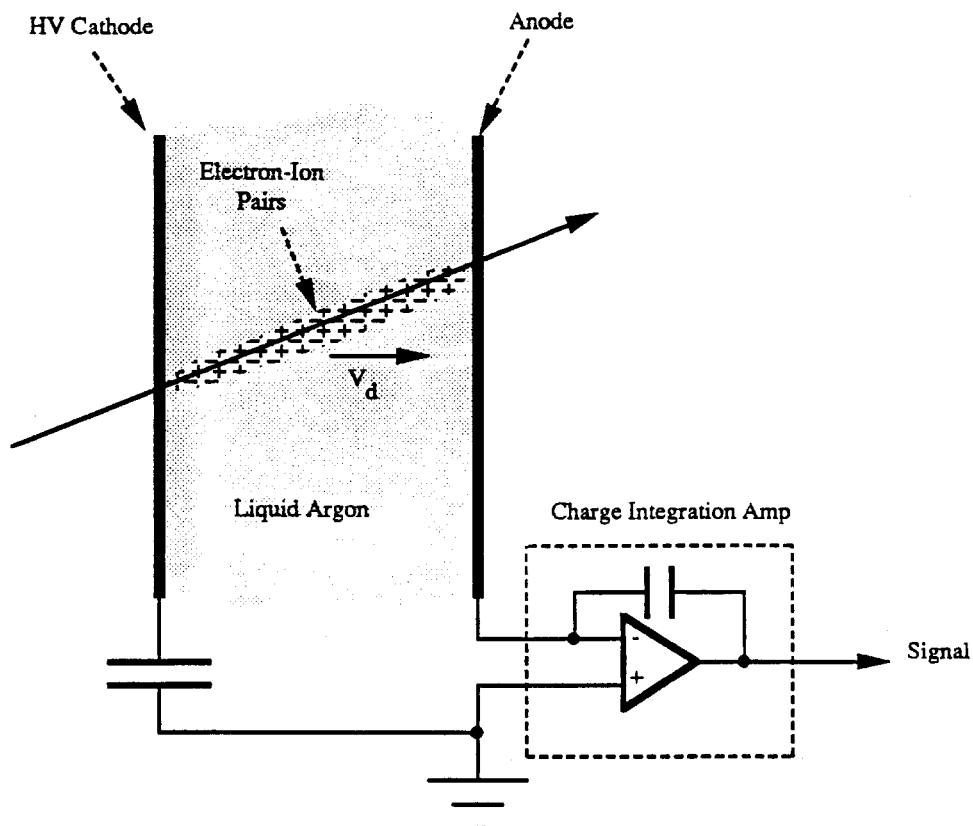


Figure 7 – Principle of liquid argon calorimetry.

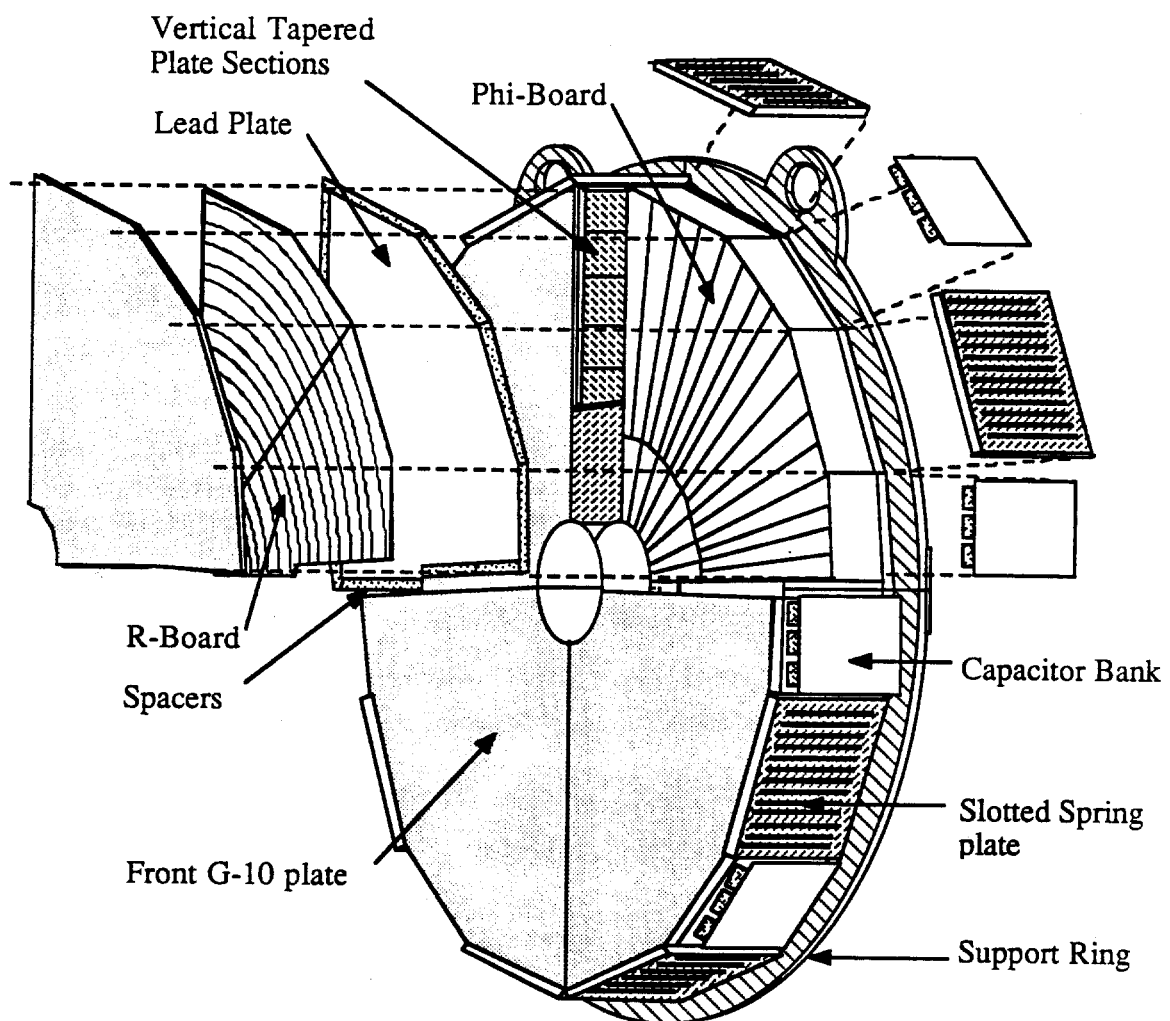


Figure 8 – Structure of the EMLAC.

copper-clad G-10 board was radially etched on both sides to form strips which indicated ϕ position. The second was etched on both sides to form strips which indicated r position. These layers were separated by 2.5 mm argon gaps which also separated each cell from the one behind it. The r -strips were focused such that a particle originating at the target would pass through the same sequential r -strip in each successive cell. The lead plates served both as absorber material and as high voltage cathodes. When electromagnetic particles interacted within the calorimeter, the resulting shower caused ionization within the argon, which induced signals on the r and ϕ strips.

Figure 10 illustrates how the EMLAC signal summation was arranged. The ϕ signal boards were divided into inner- ϕ strips and outer- ϕ strips, with twice as many outer- ϕ strips as inner- ϕ . If single strips had been used, they would either have been too large at the outer edge, or so small at the inner edge that the signal would ultimately have been dominated by electronic noise. The inner- ϕ /outer- ϕ boundary was at a radius of 40 cm at the front of the EMLAC and was focused like the r -strips. Actually, there were two r signal boards and two ϕ signal boards in each cell, effectively dividing the quadrant into two *octants*, each covering a nominal azimuthal angle of $\pi/4$ rad. Corresponding r -strips from each cell in the front section were connected, or *ganged*, together by wires called "connector strings". These added the current signals together and channeled the sum to the front of the quadrant. This was done along both sides of the quadrant to handle the signals from both octants. The inner- ϕ strips were ganged together along the inner edge of the quadrant, and the outer- ϕ along the outer edge. At the front of the calorimeter, these connector strings attached to several "readout boards" (shown in figure 11), which channeled the signals to the outer edge of the calorimeter, where cables were attached. The back section of the quadrant was ganged in the same way, except that the readout boards were at the rear of the quadrant.

The above scheme allowed signals to be read out separately from the front and back sections of the calorimeter. This was done for two reasons. First,

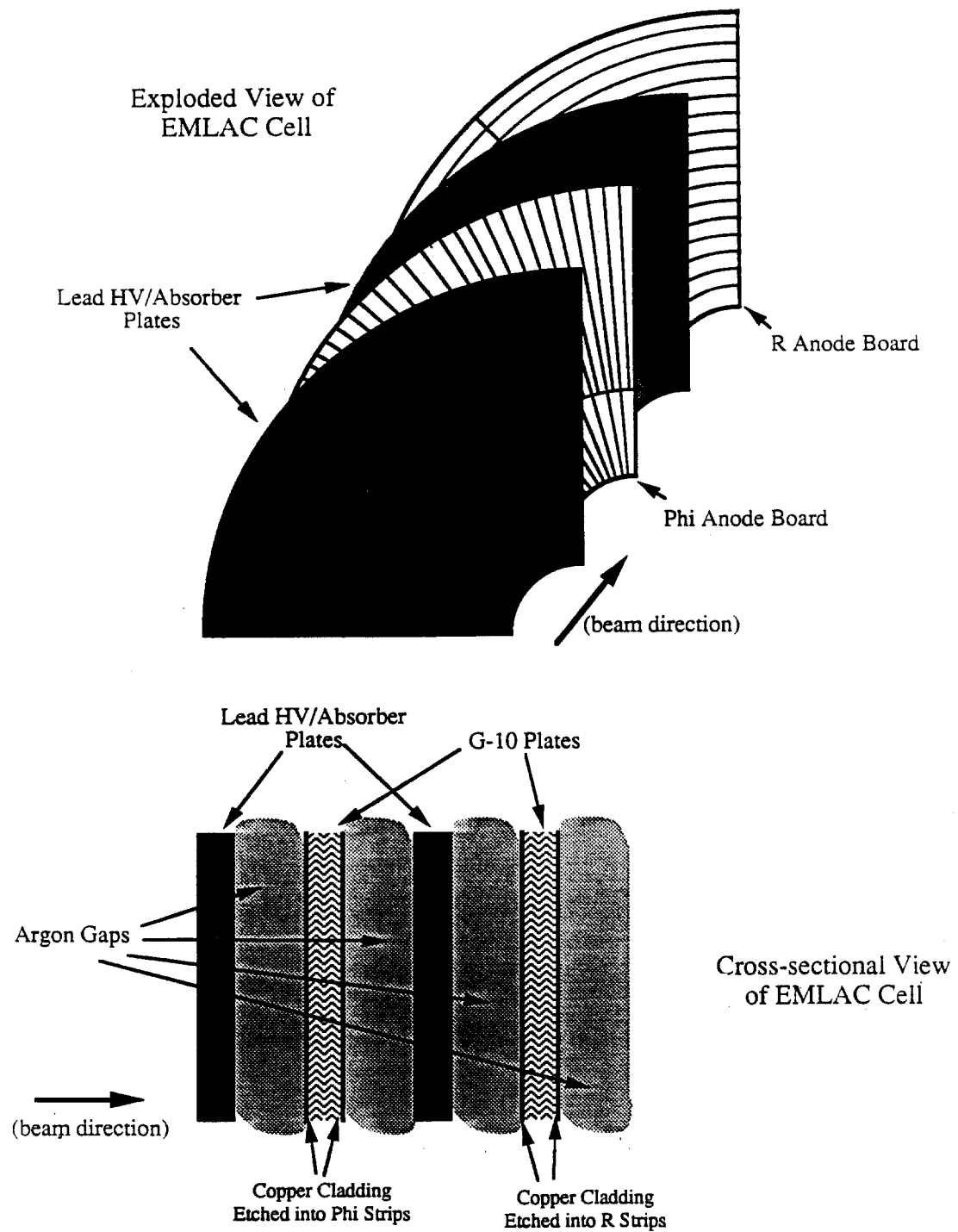


Figure 9 – EMLAC cell.

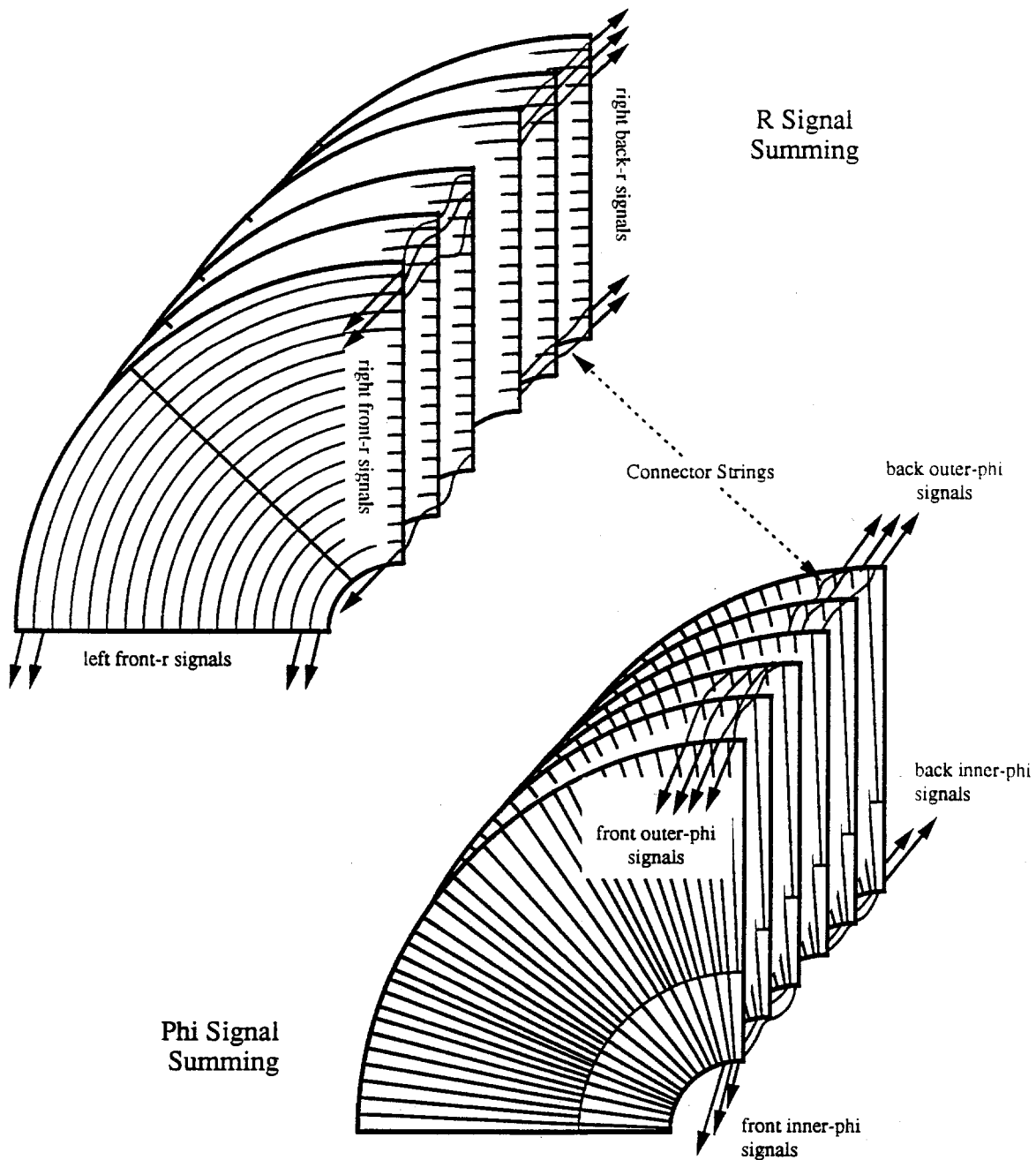


Figure 10 – Signal summing within the EMLAC. Signals from each quadrant were summed to form front and back sections, each with four separate views.

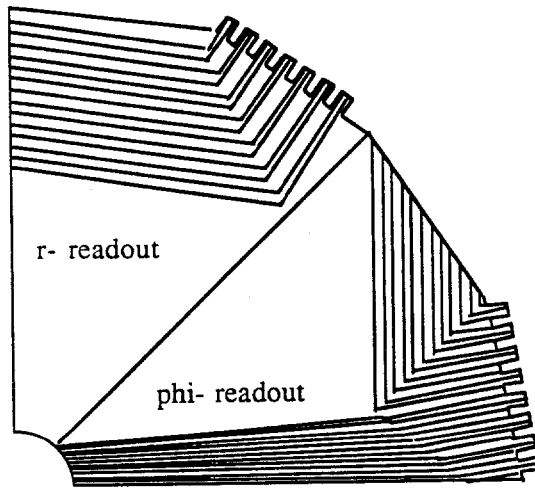


Figure 11 – EMLAC readout boards.

it gave an indication of the longitudinal shower profile as a method of hadron discrimination. Second, it improved the ability to resolve very close di-photons, as illustrated in figure 12. From the readout standpoint, each section was considered to have four *views*: (1) left-*r*, (2) right-*r*, (3) inner- ϕ , and (4) outer- ϕ . The nominal strip numbering is given in table 4. The strips were numbered such that a strip in the front section would line up with the strip in the back section with the same number. Some strips in this idealized numbering scheme were actually missing near the edges of each quadrant, due to the realities of construction.

Banks of capacitors were mounted along the sides of the EMLAC, as close as possible to the lead plates. Each lead plate was attached to ground through two 100 nF *ballast* capacitors. These served to stabilize the high voltage and to provide a low impedance return path for the signal. These capacitors were connected to the lead plates through 7 ohm resistors. This was done to damp out LC oscillations which were found to occur during electrical tests of the calorimeter. Each lead plate was supplied with high voltage by a separate wire. This provided the capability to isolate individual plates in case of problems. The detector was designed to operate with 2.5 kV on each of the plates.

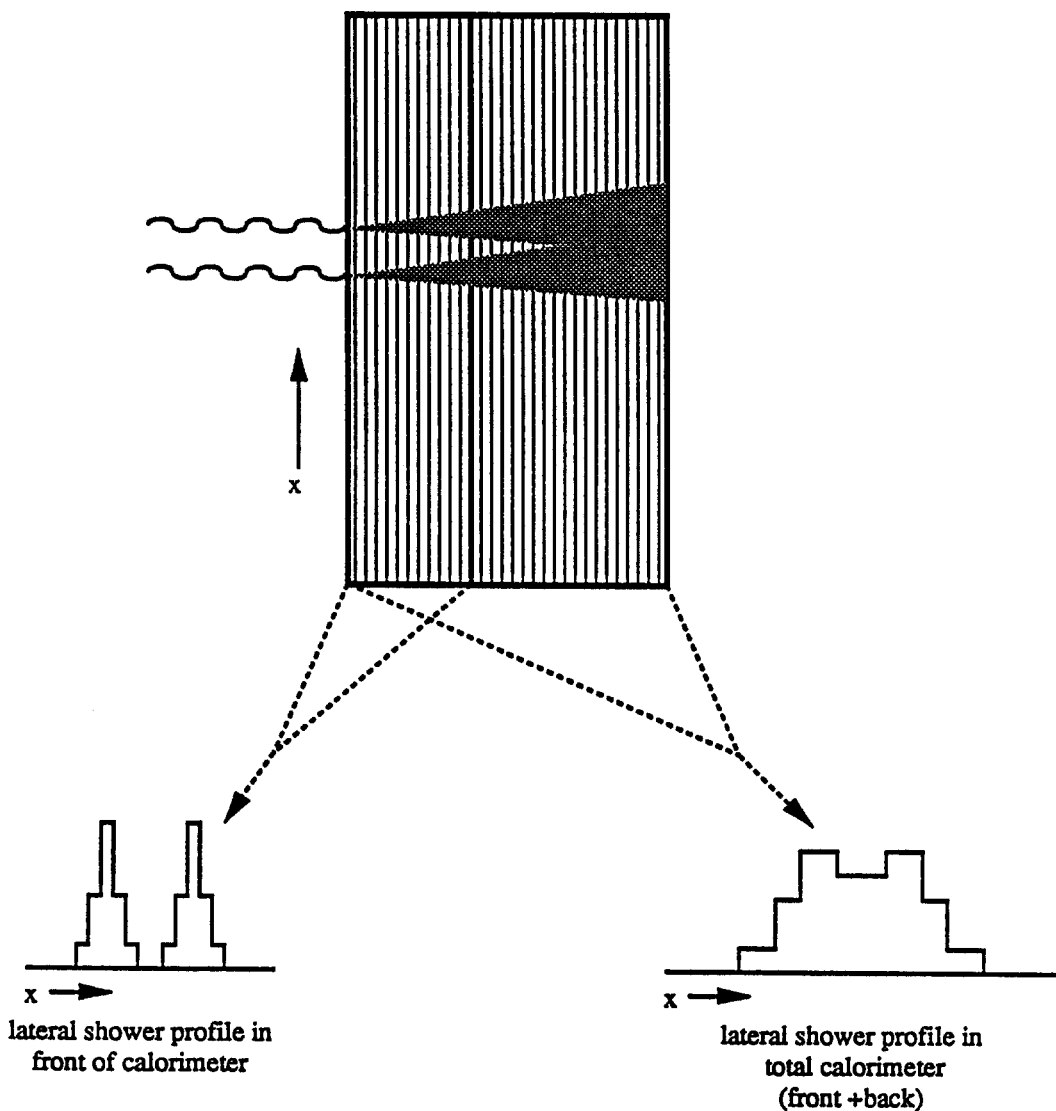


Figure 12 – Front-back separation as an aid to di-photon resolution. Showers will tend to have a narrower profile in the front section of the calorimeter. This can help to resolve di-photons which might otherwise coalesce.

View	Strip numbering	Center position of strip i
left or right- r	0 to 255	$20.23 + i * (.546)$ cm
inner- ϕ	1 to 96	$\pi * (i - \frac{1}{2})/192$ rad
outer- ϕ	1 to 192	$\pi * (i - \frac{1}{2})/384$ rad

Table 4 – Strip numbering in the EMLAC. r positions are given at the front the EMLAC. ϕ positions are given relative to the quadrant boundary.

The EMLAC was completely immersed in liquid argon. The method of support and cabling will be discussed shortly in the section on the LAC gantry.

Argon Purity

It is important to say a few words about argon purity. Equation (3.3) is only valid if none of the electrons are absorbed while drifting toward the anode plane. If we assume some impurity with a characteristic mean free path \bar{s} , then the actual total charge collected is given by^[28]

$$Q = \frac{Q_0}{\lambda} \left(1 - \frac{1}{\lambda} (1 - \exp(-\lambda)) \right) \quad (3.4)$$

where $\lambda (\equiv d/\bar{s})$ is the ratio of the gap width to the mean free path. In general, \bar{s} is a function of the drift velocity and hence of the electric field. Oxygen is a particularly worrisome impurity. First of all, its -2 valence gives it a high affinity for electrons. Also, its presence in the atmosphere means that great care must be taken at all phases of argon handling to insure purity. Oxygen contamination results in an effective mean free path which has been measured to be^[28]

$$\bar{s} = .12 \frac{E}{p} \quad (3.5)$$

where E is the applied field in kV/cm, p is the oxygen contamination in molar parts-per-million (ppm), and the result is in cm. Given the design parameters

of E706, equations (3.4) and (3.5) predict about a 10% loss of signal with a 1 ppm of oxygen contamination.

Before putting argon into the cryostat, the purity was tested. This was done by placing a sample of the argon in a test chamber which simulated the operation of the calorimeter, using a radioactive source to ionize liquid argon within a charge collection gap. The amount of charge collected as a function of applied voltage was then used to relate contamination to equivalent oxygen contamination using (3.4) and (3.5). Using this method, the contamination of the argon introduced into the cryostat was kept below that equivalent to .5 ppm of oxygen.

Because the r and the ϕ strips of the EMLAC were interleaved, the energy in each of these views was very close to half of the total energy of an incident particle. This fact was used during reconstruction to match shower profiles in r and ϕ . It was also used in the determination of resolution. Assume E_r and E_ϕ are the amounts energy which were deposited in the r and ϕ views respectively. Because energy fluctuations in each view were incoherent, the R.M.S. of $E_r - E_\phi$ was the same as the R.M.S. of $E_r + E_\phi$ (total energy E). By taking the difference rather than the sum of the view energies, the energy distribution was always centered near zero. Thus one did not have to know the actual energy of the incident particle to a great degree of accuracy to measure the resolution. Using this method, the energy resolution was measured using π^0 decay photons and found to be^[27]

$$\sigma^2(E) = (.102)^2 + (0.145)^2 E + (.022)^2 E^2 \quad (3.6)$$

where energy (E) and σ are in GeV.

3.2 THE HADRONIC LIQUID ARGON CALORIMETER (HALAC)

Figure 13 shows the structure and orientation of the hadronic calorimeter. It was centered on the beamline directly behind the EMLAC. The principle of operation was the same as that of the EMLAC, but in this case it was hadronic showers which were being studied, which have greater transverse and longitudinal profile.

The HALAC consisted of 53 2.5 cm thick steel plates, interleaved with sampling cells called "cookies". Figure 14 shows an exploded view of a single cookie. There were two anode planes, back to back, at the middle of the cookie. These were made of single-sided copper-clad G-10, with the copper side facing away from the middle. The copper was etched to form horizontal rows of triangular pads. Signals from these pads were channeled to the sides of the cookie via signal traces which ran horizontally between the rows. The two anode planes were aligned such that each row of triangles on the upstream plane corresponded to a row of signal traces on the downstream plane, and vice versa. Thus, when viewed from upstream, the triangles formed an unbroken plane, as shown in figure 15. The anode planes faced high voltage planes, which were separated from them by a 3 mm argon ionization gap. This gap width was maintained by G-10 spacer strips, which ran horizontally. Besides maintaining the gap width, these strips covered the signal traces. This was done so that no current would be induced directly onto the signal lines. The high voltage planes themselves were made of double-sided copper-clad G-10. The copper which faced the anode plane was held at high voltage while the outer layer was kept at ground.

As with the EMLAC, the readout pads of the HALAC were focused at the target. Pad size increased from ≈ 10 cm in height in the most upstream cookie, to ≈ 14 cm in height in the most downstream. Corresponding pads in the 14 upstream cookies were ganged together to form triangular *towers*, which pointed at the target. These towers made up the front section of the HALAC. Similarly, the pads in the remaining 39 cookies were ganged together to form the towers of the back section.

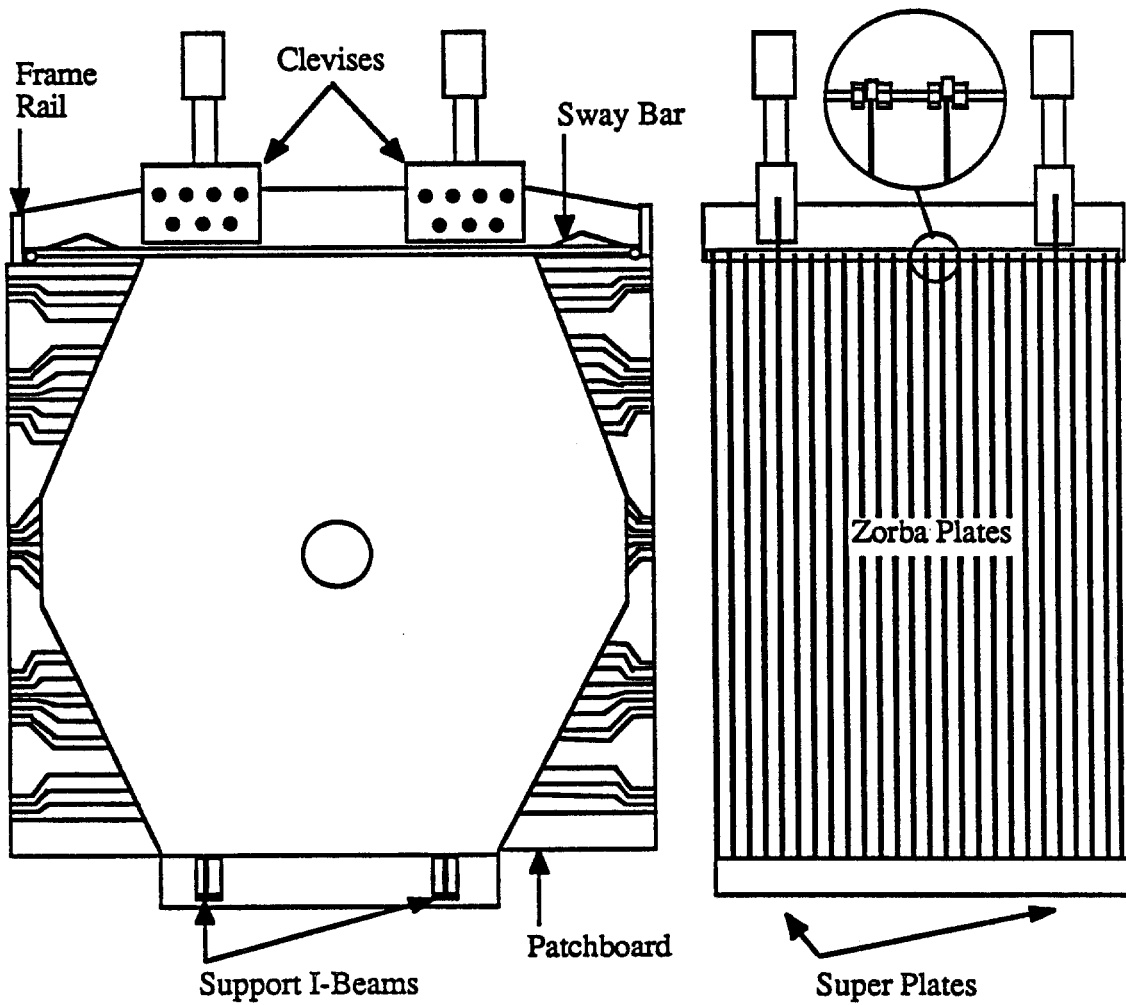


Figure 13 – The hadronic calorimeter. Steel “Zorba Plates” acted as absorber material. Noninteracting beam passed through the beam hole, shown in the front view (left).

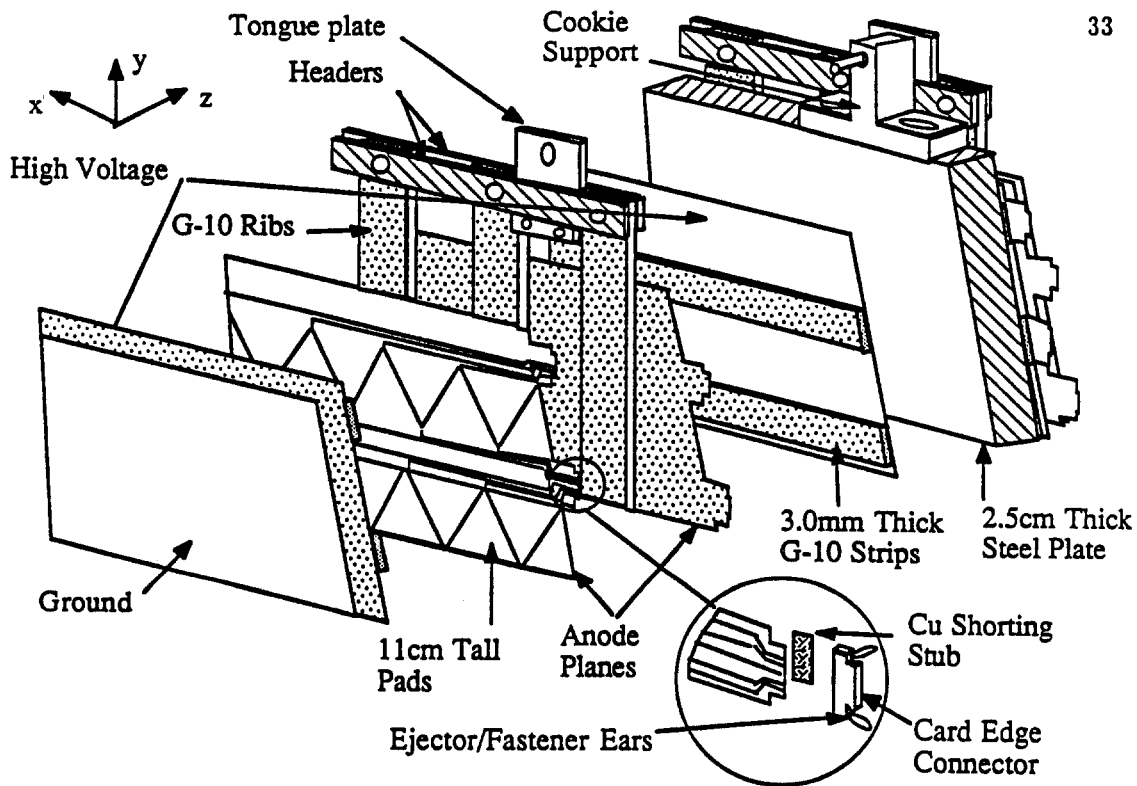


Figure 14 – HALAC readout cell, or “cookie”.

The energy resolution of the HALAC was measured using low intensity π^- beams with energies from 50 to 200 GeV, and found to be

$$\sigma(E)/E = 0.04 + 1.83/\sqrt{E} \quad (3.7)$$

where energy is in GeV.

3.3 THE GANTRY

The EMLAC and the HALAC were suspended within a common cryostat. This was done because of the practical difficulties involved in supporting them and keeping them immersed in liquid argon. The cryostat was made of 1.6 cm thick stainless steel. The entire assembly was suspended from a movable gantry, as shown in figure 16.

The uppermost portion of the cryostat, or “top hat”, was fixed to the gantry. It contained the cooling system which kept the argon in a liquid state.

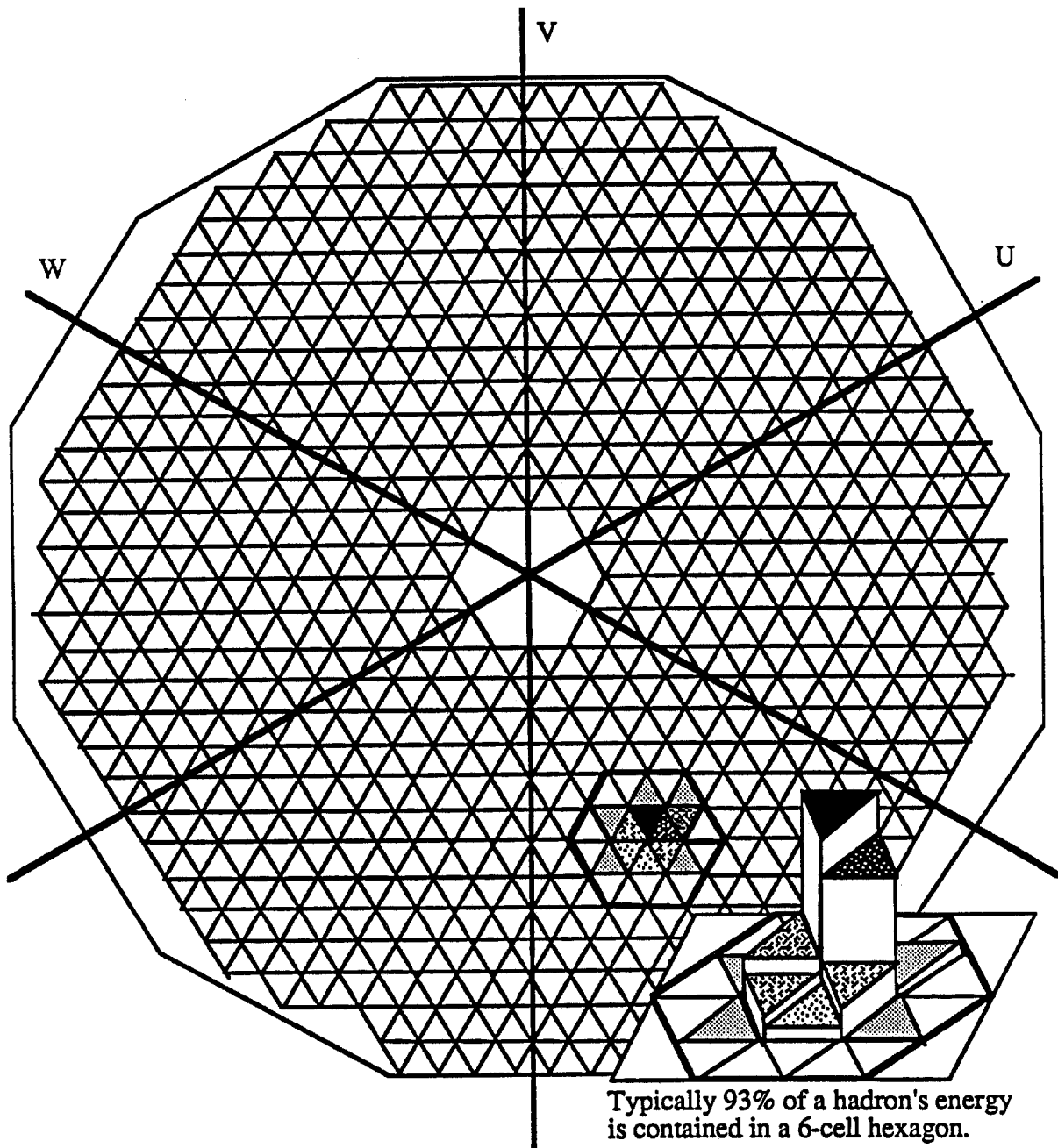


Figure 15 – HALAC pad configuration. Pads from the individual cookies were summed to form front and back towers.

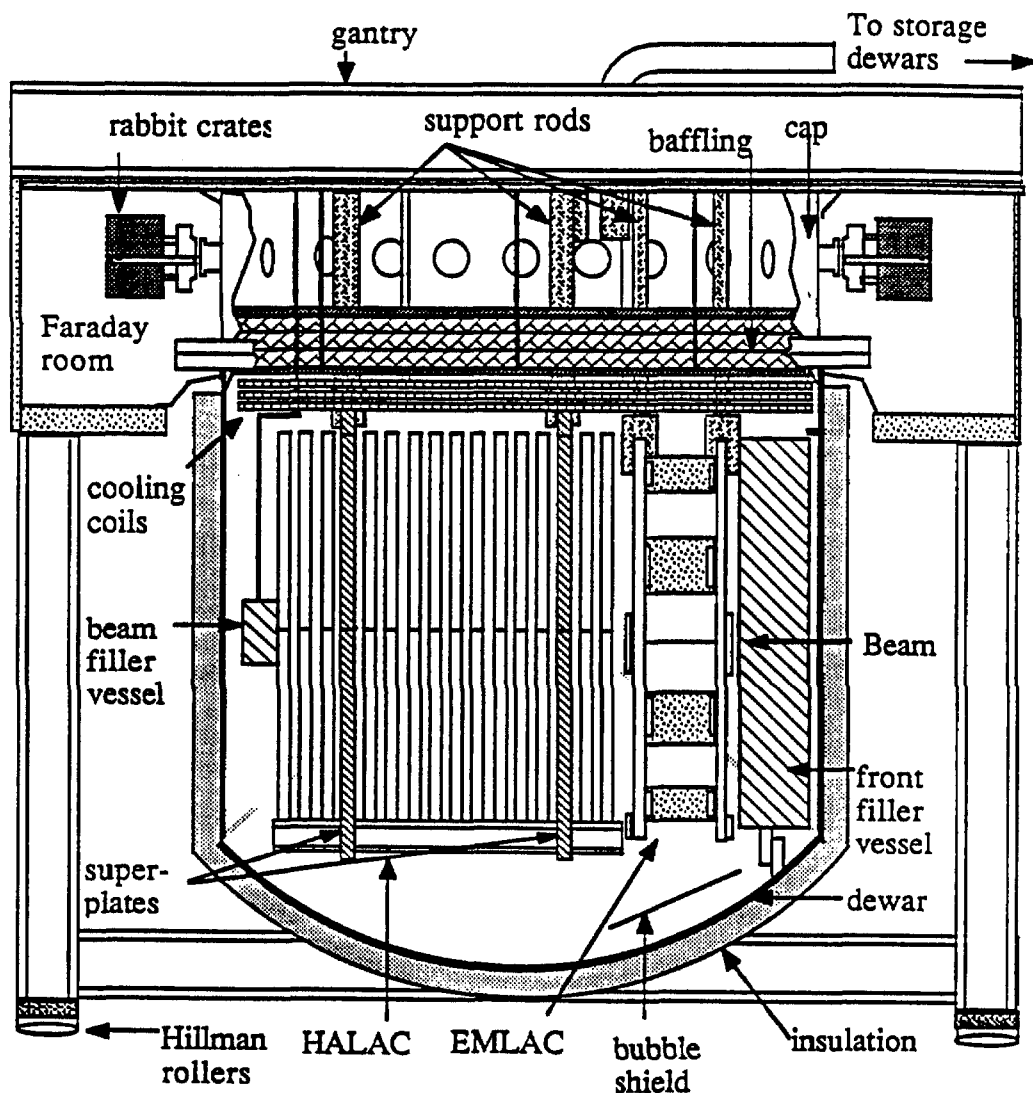


Figure 16 – The LAC gantry.

At the point where noninteracting beam struck the cryostat, there was a 5 cm diameter port made of 1.6 mm thick stainless steel. This *beam window* reduced the amount of material in the path of the beam and hence the amount of scatter into the calorimeters. It was located in the lower portion of the cryostat, which was raised into place after the calorimeters were hung.

The entire gantry was on rollers which allowed it to move laterally relative to the beam. This motion was necessary for the construction and suspension of the calorimeters. It was also useful for calibration. This will be discussed shortly.

Filler Vessels

Because it would have been very difficult to build the cryostat with a flat upstream face, it was necessary to put a low density "filler vessel" between the upstream wall of the cryostat and the EMLAC. This prevented electromagnetic showers from depositing a large amount of energy in the argon before reaching the EMLAC, thereby disastrously degrading the resolution. This vessel was made of RohacellTM, which was coated with fiberglass and epoxy. It was encased in a 1.6 mm thick stainless steel skin to provide structural rigidity.

In order to further reduce beam scatter into the calorimeters, there was a cylindrical "beam filler vessel" within the cryostat, surrounding the beamline. It extended from the downstream face of the front filler vessel to the downstream wall of the cryostat, filling the holes in the calorimeters. This vessel was made out of 3.2 mm thick stainless steel which was sealed against the surrounding argon. It was filled with gaseous helium at roughly atmospheric pressure. This vessel also served to preserve the resolution of the FCAL, just downstream of the gantry.

Faraday Room

Signal feed-through ports were distributed around the sides of the top hat. These channeled signals between the inside and the outside of the cryostat, while preserving argon purity. Cables carried the signals from both calorimeters

to these feed-throughs. On the outside of the feed-through ports, short cables carried the signals to the charge integration amplifiers (see discussion, section 4.2) Based strictly on electrical considerations, it would have been desirable to have the first amplification stage in the argon, close to the detector. However, this was deemed impractical because of the difficulty of access.

The entire top hat was surrounded by a Faraday room, which shielded the electronics from external noise. Transformers isolated the Faraday room power from the outside. All signals in and out of the room were isolated either optically or, in the case of fast logic pulses, with pulse transformers. The high-voltage supplies for the calorimeters also resided in the Faraday room. There was a separate feed-through for each lead plate in the EMLAC and for each cookie in the HALAC. The lead plates were grouped into 8 sets, each corresponding to the front or back section of a particular quadrant. Each set had its own high voltage supply, which was nominally set at 2.5 kV, although some were set as low as 1.8 kV because of electrical breakdown problems. High voltage lines from the cookies were divided into front and back, each with its own supply, set to 3 kV. Eight individual lead plates and 3 cookies were found to have serious breakdown problems and so were isolated and operated at separate, very low voltages.

3.4 THE FORWARD CALORIMETER (FCAL)

In high- Q^2 interactions, the incident beam particle will often fragment into a beam jet, which is produced at a small angle with respect to the incident direction, i.e. very forward. The high rates and high particle densities near the beam make a liquid argon calorimeter impractical for studying this jet. Indeed, resolving the individual particles would be a formidable task for any detector. On the other hand, if one could measure the total momentum of the jet, it would be a valuable tool in determining exact event kinematics. For this reason a total absorption forward calorimeter, or FCAL, was built and placed just downstream of the LAC gantry.

Details of the construction and performance of the FCAL can be found

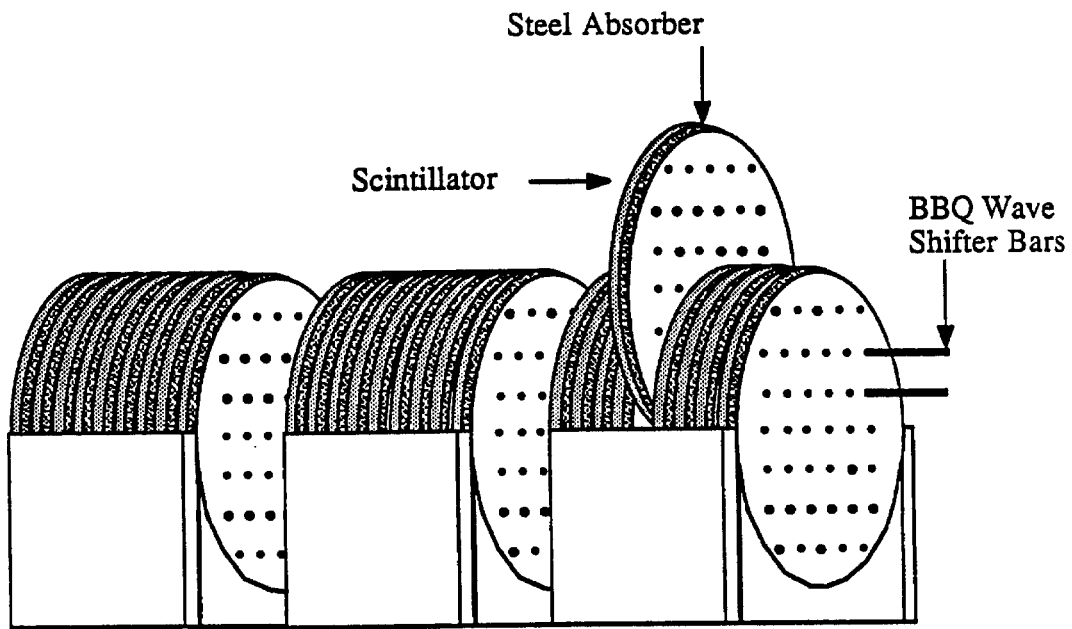


Figure 17 – The forward calorimeter.

elsewhere^[28]. As shown in figure 17, the FCAL consisted of three identical modules, one after another, centered on the beamline. These totaled 9.5 interaction lengths. Each module consisted of 28 circular steel absorber plates, each 114 cm in diameter by 1.9 cm thick, spaced 6.9 mm apart. Between the plates and on either end were 29 4.6 mm thick sheets of acrylic scintillator. Seventy six holes were drilled through the entire stack on an 11.5 cm grid. In these holes were placed wave shifter rods. These were 1 cm in diameter and ran the length of the stack. There was a phototube mounted to one end of each rod. A 2 cm diameter hole through the center of each module allowed noninteracting beam particles to pass.

Hadronic showers produced blue light in the scintillator sheets. This light propagated to the wave shifter rods, which converted it to green and transmitted it to the phototubes. The total signal should have been proportional to the amount of energy deposited in the calorimeter. The relative pulse heights in the

phototubes could be used to determine the centroid of a beam jet. However, because some light from every shower reached every phototube, it would be impossible or at least very difficult to resolve individual showers within the modules.

At the beginning of the running period, all of the phototubes were on the downstream end of each module. It was discovered that a miscalculation had been made with regard to the extinction length of the wave shifter rod. Namely, it was shorter than was thought. This had the effect that the signal was very dependent on longitudinal shower profile, which has large fluctuations for hadronic showers. In an attempt to salvage the resolution of the FCAL, half of the wave shifter rods in the two upstream modules were turned around so that the phototubes were on the upstream side. Thus, by using the total energy signal, and by making corrections based on the front/back ratio, one could minimize the effect of the extinction length problem. Nevertheless, the FCAL resolution was dominated by these systematics.

3.5 THE TRACKING SYSTEM

In order to study the jets associated with direct photon production, E706 included a charged tracking system, including precision tracking to locate vertices within the target*. For the purpose of this analysis, the tracking system was also used to identify showers within the EMLAC which were caused by electrons or charged hadrons. This was done by projecting each reconstructed track to the upstream face of the EMLAC and checking if the projected track position matched the position of a reconstructed shower. Such showers could then be rejected as direct photon candidates.

Upstream Tracking

Beam tracking and tracking upstream of the analysis magnet (including the

* The term "vertex" refers to the point of origin of a group of particles. The point where the incident beam particle interacts with the target is referred to as the *primary* vertex. *Secondary* vertices can arise either from the decay or interaction of the particles produced at the primary vertex.

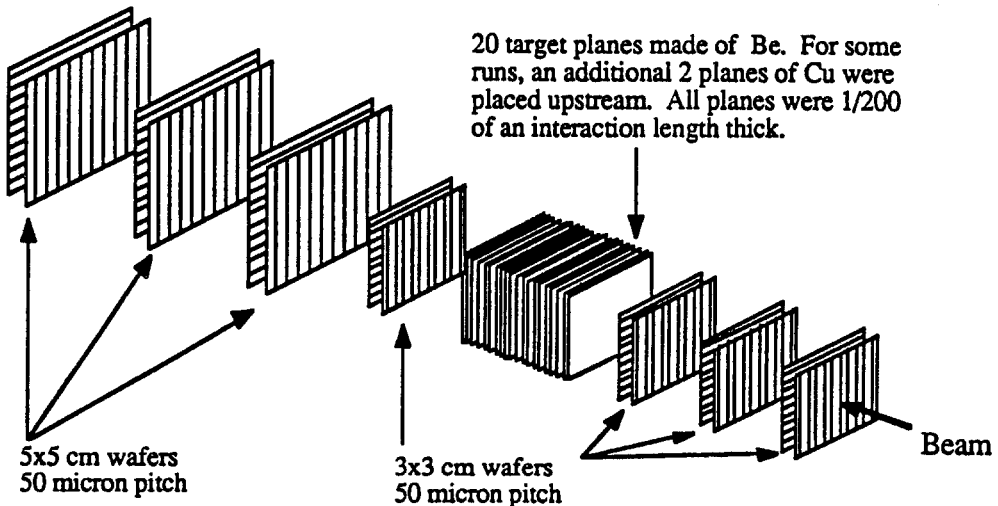


Figure 18 – The SSD system.

tracking used for vertex finding) were provided by a Silicon Strip Detector (SSD) system^[28]. SSDs measure charged particle position by means of signals induced on strips which have been etched onto a silicon wafers. The E706 SSD system, shown in figure 18, consisted of 14 planes of SSDs. Each plane was mounted on a fan-out board to channel the signals from the strips to the front-end electronics. The planes were arranged in pairs consisting of an X plane (i.e. a plane with the strips running horizontally) and an orthogonal Y plane. All planes had 50 μm pitch. Three 3 cm \times 3 cm XY pairs were upstream of the target to measure incident beam position. Immediately downstream of target was one more 3 cm \times 3 cm pair followed by three 5 cm \times 5 cm pairs.

The SSDs were placed in a steel box, along with their front-end electronics, to physically protect them and shield them from electronic noise. The target was also contained in this box. The angular resolution of the SSDs was estimated to be .08 mr. The vertex position resolution was measured to be 24 μm in x and y , and 500 μm in z ^[29].

Analysis Magnet

The analysis magnet itself was a vertical dipole, with an aperture that expanded from 35.6 cm \times 25.4 cm at the upstream end to 137.2 cm \times 124.5 cm over

a length of 3.9 m. The current was adjusted to give a 450 MeV kick[†]. The direction of the field was reversed whenever the beam polarity was switched. This minimized systematic differences when comparing data produced by beams of different sign. It also insured that noninteracting beam particles would continue to pass through the beam window in the LAC cryostat.

Downstream Tracking

Tracking downstream of the magnet was provided by 16 Proportional Wire Chamber (PWC) planes. These were grouped into 4 modules, each with an X plane, a Y plane, a U plane (rotated by +37°), and a V plane (rotated by -53°). The offset planes were used to match tracks from the X and Y views (or vice versa). All of the planes had a pitch of 2.5 mm, which gave the system an angular resolution of .03 mr.

Note that there were no offset planes in the SSDs. This means that there was no way, within the SSD system, to match tracks from the X-view SSD planes with tracks from the Y-view SSD planes. Therefore, during reconstruction, downstream track positions were used to match X-view and Y-view SSD tracks. This will be discussed in more detail in chapter 6.

Table 5 shows the nominal z positions of the tracking modules. The term "module" here refers to either SSD pairs or groups of four PWC planes. Precise positions and alignment were determined during offline analysis by optimizing track fits.

[†] The term "kick" is a measure of magnetic flux for a dipole field. It is defined as the amount of momentum, orthogonal to the beam direction, which is imparted to a charged particle traversing the field at approximately the speed of light. The change in direction that this kick causes is used to measure the particle momentum.

Station	z-position	Size	Pitch	Description
SSD 1	-128.5 cm	$3.0 \times 3.0 \text{ cm}^2$	$50 \mu\text{m}$	beam tracking
SSD 2	-32.5 cm	$3.0 \times 3.0 \text{ cm}^2$	$50 \mu\text{m}$	beam tracking
SSD 3	-15.0 cm	$3.0 \times 3.0 \text{ cm}^2$	$50 \mu\text{m}$	beam tracking
SSD 4	-2.0 cm	$3.0 \times 3.0 \text{ cm}^2$	$50 \mu\text{m}$	upstream tracking
SSD 5	3.5 cm	$5.0 \times 5.0 \text{ cm}^2$	$50 \mu\text{m}$	upstream tracking
SSD 6	9.0 cm	$5.0 \times 5.0 \text{ cm}^2$	$50 \mu\text{m}$	upstream tracking
SSD 7	14.5 cm	$5.0 \times 5.0 \text{ cm}^2$	$50 \mu\text{m}$	upstream tracking
PWC 1	382.0 cm	$1.22 \times 1.63 \text{ m}^2$	2.5 mm	downstream tracking
PWC 2	476.0 cm	$2.03 \times 2.03 \text{ m}^2$	2.5 mm	downstream tracking
PWC 3	570.0 cm	$2.03 \times 2.03 \text{ m}^2$	2.5 mm	downstream tracking
PWC 4	661.0 cm	$2.44 \times 2.44 \text{ m}^2$	2.5 mm	downstream tracking

Table 5 – E706 tracking modules.

3.6 THE TARGET

The target was located in the SSD box, between the third and fourth SSD modules. All of the data used in this analysis were taken with a beryllium target in place. It consisted of 20 separate plates of beryllium, placed 1.6 mm apart, in the path of the beam. Each was $2 \text{ cm} \times 10 \text{ cm}$ in cross-sectional area and 2 mm thick. This thickness is equal to 1/200 of an interaction length for beryllium. Some data were taken with an additional two planes of copper just upstream of the beryllium planes. These planes had the same spacing and cross-sectional area as the beryllium planes. They were also 1/200 of an interaction length thick, which for copper is 1.6 mm. A segmented target was used so that one could distinguish between secondary vertices arising from multiple scattering and those due to particle decays. The former would tend to occur within the target layers, while the latter would tend to occur in the gaps. This is useful for the study of heavy quark physics, but has no bearing on this analysis.

3.7 BEAMLINE AND CERENKOV DETECTOR

The beam used for E706 was what is known as a *secondary* beam. During the running period, the Fermilab main accelerator or Tevatron operated with a 57 second cycle. Protons went through the various stages of injection and acceleration over a period of 34 seconds, bringing them to a full energy of 800 GeV. This was followed by a 23 second *spill*, during which these primary protons were separated and distributed to the various fixed target experiments. In the case of E706, the primary beam struck a target consisting of one interaction length of aluminum*. From here the secondary beam was extracted and conveyed to the M-West experimental hall.

The M-West Beamline

Figure 19 shows a schematic representation of the M-West Beamline. The aluminum target is labelled MW8TGT. Dipole magnets are indicated by a "D" in the name (e.g. MW8D) and an optical prism on the drawing. Quadrupoles, which are used for focusing, are indicated by a "Q" in the name and an optical lens on the schematic. A "C" in the name indicates a collimator. The inclusion of "V" or "H" in the name of a device indicates whether the action is in the vertical or horizontal direction. The beamline also included several "spoilers", indicated by an "S". These were large flux carrying steel yokes which surrounded the beamline to sweep away muons travelling parallel to the beam. The beam profile was monitored using several Segmented Wire Ionization Chambers (SWICs).

The beamline design was optimized for 530 GeV beam[†], but other momenta could be selected for calibration purposes. Beamline devices were controlled and monitored by a Digital PDP-11TM computer. Beam momentum was selected by adjusting the current to the beamline magnets. Rate and momentum spread

* Actually, the target started out at .77 of an interaction length. It was later increased to a full interaction length to increase secondary yield.

† This value of 530 GeV was chosen because pions at this momentum have approximately the same momentum per quark as protons at 800 GeV, the full energy of the Tevatron. Ultimately, however, no data were taken with 800 GeV protons, making this energy somewhat of a historical artifact.

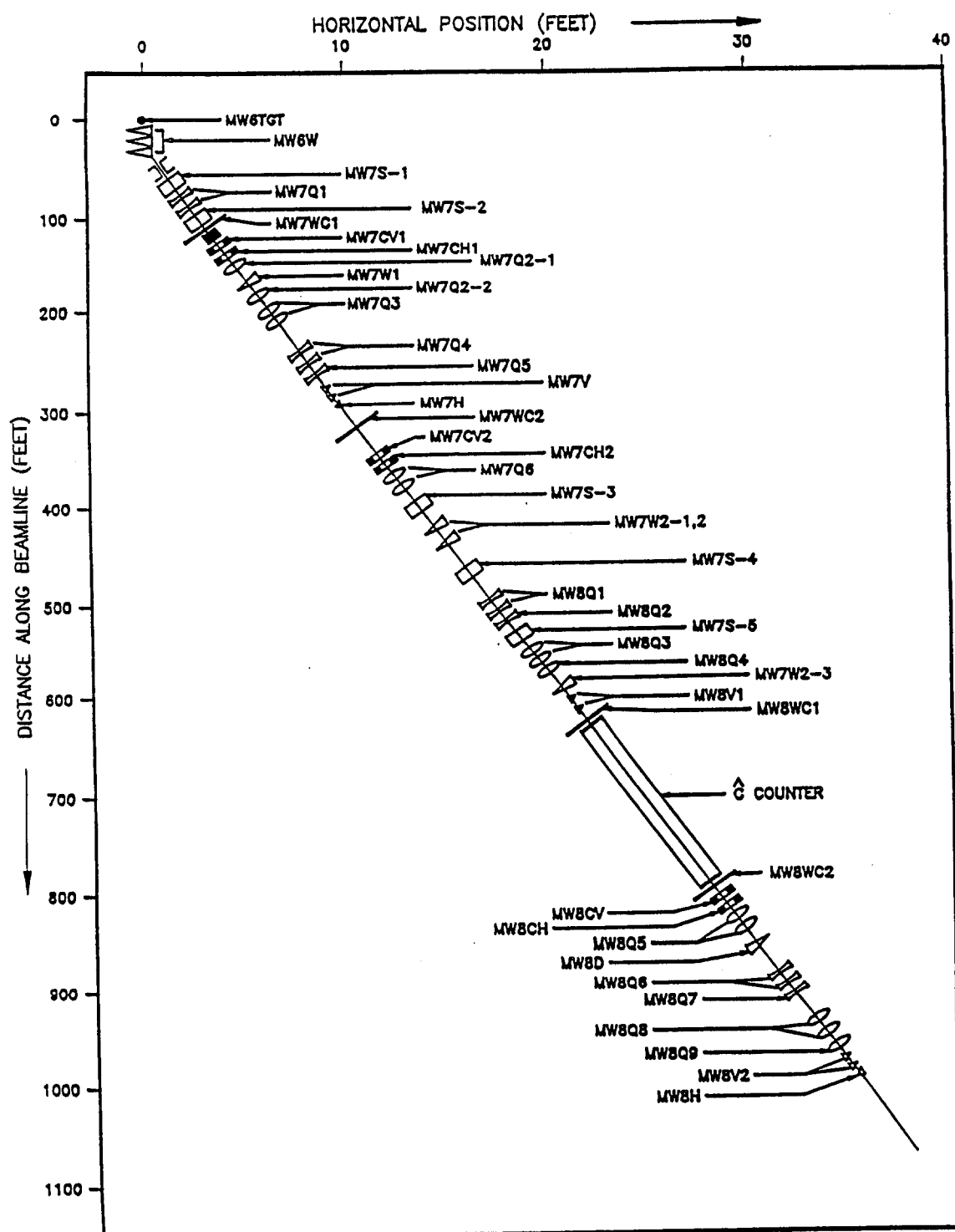


Figure 19 – M-West secondary beamline. Beamline devices are represented by their optical equivalents.

were adjusted by opening and closing the collimators. Changing beam polarity required physical rewiring of several of the beamline devices, which typically took several hours.

While running with negative beam, secondary intensity was limited by production at the target and by the efficiency of the beamline transport. For this reason, the collimators were generally fully opened to allow the maximum number of particles to pass. The maximum intensity achieved was 2×10^7 secondary particles per spill for 1×10^{12} primary protons incident on the aluminum target.

While running with positive beam, production intensity was much higher because of the positive sign of the primary beam. Thus, collimators had to be partially closed to limit the intensity to levels which the spectrometer could accept. Typical secondary intensity was about 6.5×10^7 particles/spill for positive beam.

Cerenkov Detector

The beamline included a section where the beam dispersion was minimized, such that the particles travelled parallel to one another. This section was to accommodate a 42 m long differential Cerenkov detector, shown in figure 20. This detector used gaseous helium as a radiator, at a pressure of 4-6 psia. There was a spherical mirror at the downstream end which reflected light back to a system of light guides and photomultiplier tubes near the upstream end. The detector was designed to detect particles with a Cerenkov angle (Θ_c) of 5.00 mrad. By varying the pressure of the helium, one was able to vary the index of refraction, and thus determine which particles triggered the detector. Figure 21 shows the Cerenkov detector response for both beam signs as a function of helium pressure. A study of such curves determined the relative particle content of the beams^[31]. The results are shown in table 6. While direct photon data were being taken, the Cerenkov detector pressure was set to tag K^- during negative running and π^+ during positive running.

Negative beam		Positive beam	
π^-	97.0%	p	91.3%
K^-	2.9%	π^+	7.2%
\bar{p}	0.2%	K^+	1.5%

Table 6 – Beam content for 530 GeV secondary beam.

Hadron Shield

Surrounding the downstream end of the beamline was a steel hadron shield, shown in figure 22. Its function was to absorb hadrons travelling parallel to the beam. This beam halo could mimic high- p_T photons in the EMLAC. The beam pipe passed through a vertical blade in the hadron shield. This blade could be removed to allow vertical movement of the beam. By coordinating this movement with the lateral movement of the LAC gantry, the entire face of the LAC could be illuminated with beam for calibration purposes. For full vertical motion of the beam, several downstream beam devices had to be removed, as did the analysis magnet.

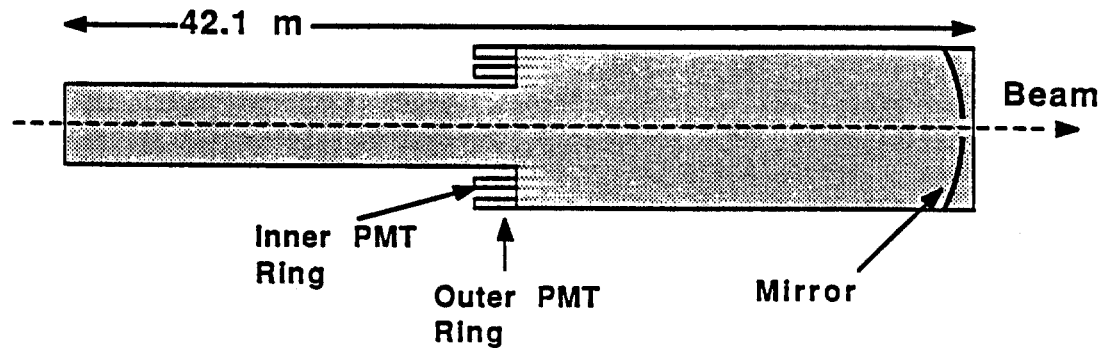


Figure 20 - E706 Cerenkov detector.

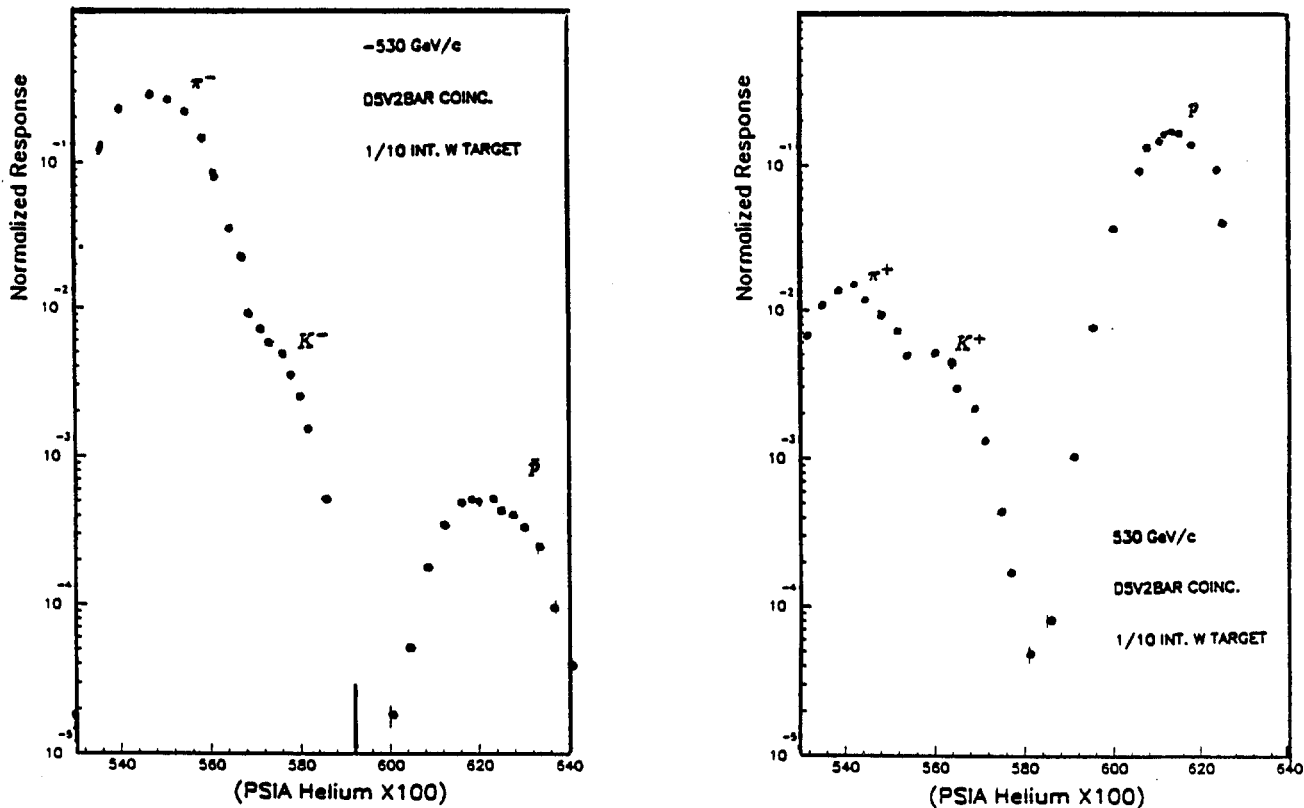


Figure 21 - Cerenkov detector pressure curves. The contribution from the individual beam particle types is indicated.

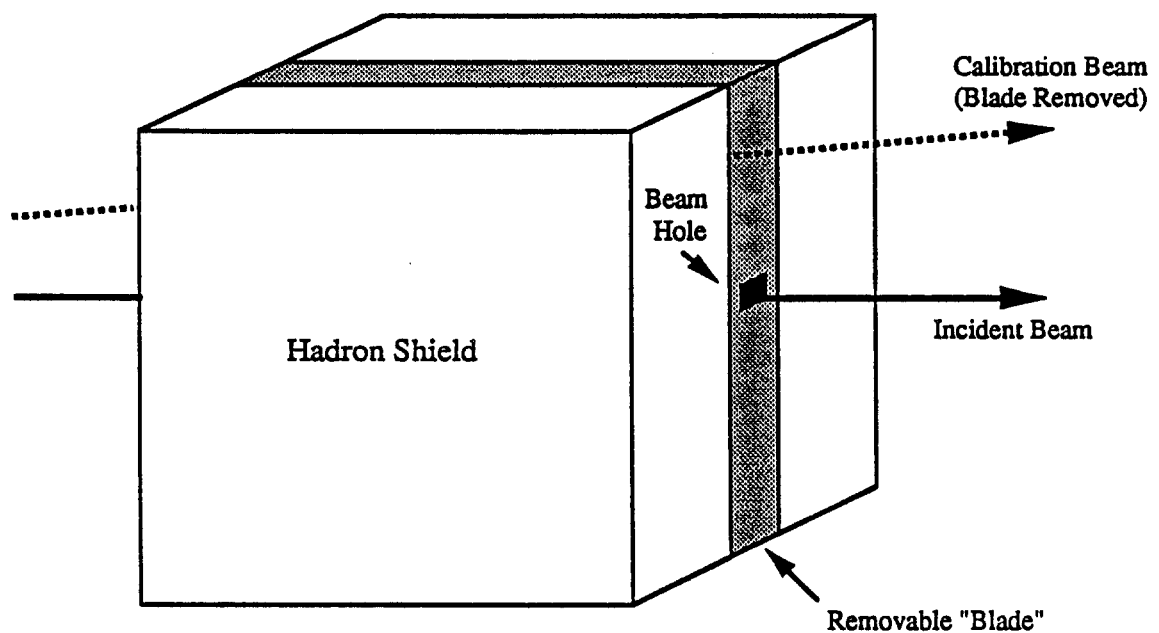


Figure 22 – Hadron shield. A removable central blade allowed calibration of the LAC.

4. Instrumentation

Reading the data out of the various parts of the spectrometer and transferring them to tape was a complex task, involving many steps. The electronics of the LAC were read out using a system known as the RABBIT system, which will be discussed in the first section of this chapter. The custom amplifiers designed to operate within this system are covered in section 2, while the exact configuration is of the system for this experiment is found in the following section. In the case of the tracking system, an entirely different system was used, which is discussed in section 4. Finally, section 5 describes the data acquisition system which collected this information, along with information from the other parts of the spectrometer, and wrote it to tape.

4.1 THE RABBIT SYSTEM

The electronics which read out EMLAC and HALAC were designed to operate within the standards of the Redundant Analog-Bus Based Information Transfer (RABBIT) system^[32], developed at Fermilab. This system is based on crates, called *hutches*, which have two more or less redundant busses over which analog and/or digital data may be passed. The busses are referred to as the “top bus” and the “bottom bus”. Each has a separate controller, called a EWE. There is also a special purpose Before After Timer (BAT) module which terminates the bus and provides several crate-wide timing and voltage signals. The 22 remaining slots are available for general purpose modular electronics.

The RABBIT protocol defines locations within the crate by module number and subaddress, with up to 64 subaddresses in each module. In general, either EWE may select any location within the crate. An analog signal from the selected location is transmitted to the EWE, where it may be digitized by a 16-bit analog-to-digital converter (ADC). Analog data are transmitted to the EWE differentially; that is, a reference value is sent along with the signal, to reduce the effects of coherent noise pickup.

This central digitization greatly simplifies the job of building electronics. However, because each digitization requires about 17 μ sec, one pays a price in speed, since at most two channels per crate may be digitized at one time. For this reason, there is a provision for "zero-suppression", whereby the digitization sequence is halted if the signal does not exceed some user-defined threshold. This decision takes about 3 μ sec.

In addition to analog data, digital data may be passed to and from the modules in the RABBIT crate. As with the analog addressing, each module may contain up to 64 digital subaddresses, accessible to either EWE.

In the original conception, the redundant busses were designed for low-access environments, such as colliders, so that the system could keep running in the event that one bus had a failure. In E706, however, the redundancy was used rather to speed up the readout by allowing two channels to be digitized simultaneously in each crate.

EWEs are controlled by dedicated processor/buffer units known as MXs. An MX may be up to 100 m away from the EWE it controls, again with low-access environments in mind. Each MX controls up to four crates, with separate cabling for top bus EWEs and the bottom bus EWEs. Thus, for every location within the RABBIT crate, there are two completely separate paths to and from the controlling MX. If redundancy and/or speed are not issues, each crate can be controlled by a single EWE. In this mode, each MX can control up to eight crates.

4.2 LAC AMPLIFIERS (LACAMPs)

Because the EMLAC and the HALAC operated on the same principle, one type of amplifier was used to read out both detectors. These amplifiers were configured in custom RABBIT modules, called LACAMPs. Each LACAMP handled 16 detector channels, either from EMLAC strips or HALAC towers. In addition to measuring energy depositions, the LACAMPs provided timing information about the event.

Figure 23 shows a block diagram of a LACAMP module. Short cables connected the signal feed-throughs of the LAC cryostat to connectors on the back of the RABBIT crate, which were mounted around the sides of the cryostat top hat. Through these cables, signals were transmitted to the LACAMP modules within each crate.

Charge Integration

Figure 24 shows a schematic representation of a single LACAMP channel. The incoming charge was collected on a capacitor; thus the voltage across the capacitor was proportional to the integrated current, and hence the energy of the deposition. The risetime was dominated by the electron drift velocity within the detector, and was of the order of 300 ns. A large value resistor was included to return the circuit to its ambient state with an RC of about 150 μ sec.

Within the LACAMP module, the integrated signal was connected to a chip which delayed it by a total of 800 ns. If the event satisfied certain requirements of the experimental trigger (see chapter 5), the electronics of the trigger system sent a logic pulse to the BAT modules, initiating the EVENT timing sequence (see figure 25). In this sequence, the BATs broadcasted two logic signals to the modules within each crate. The first, called the BEFORE signal, arrived at the LACAMP at the time at which the output of the delay chip represented the integrated value just *before* the event occurred, causing this value to be held. The AFTER signal then arrived at a time at which the output of the delay chip represented the full value of the integration, and this value was also held. When the appropriate analog location was selected, these values were sent to the EWE, which measured their difference. By taking the difference between the integrated signal before and after the event occurred, the effects of low frequency noise subtracted out, as well as the effects of *pileup*, i.e. when a second event arrived before the several hundred microseconds needed for the circuit to return to its ambient state.

The states of the BEFORE and AFTER signals were held, i.e. the values of the integrated charge signals were retained, until the entire system was read

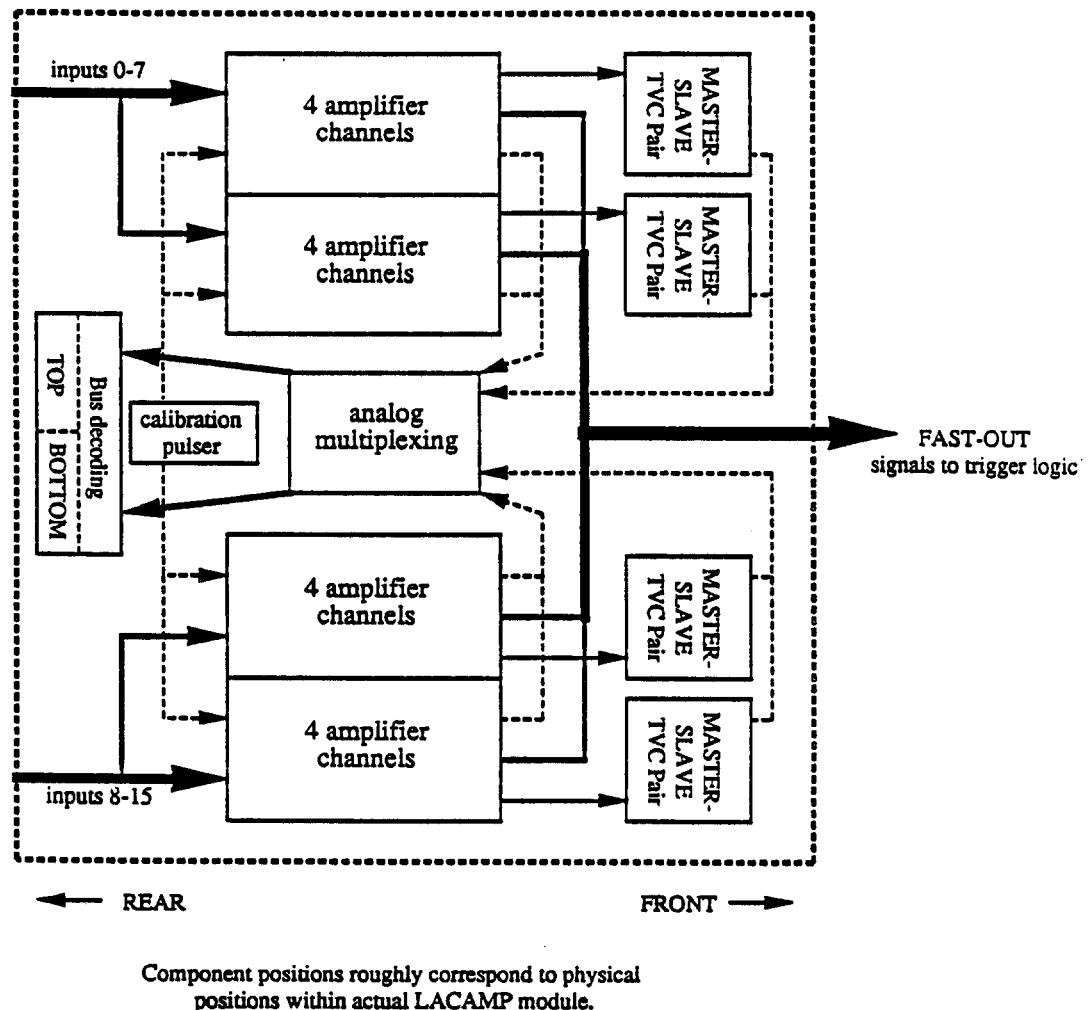


Figure 23 – Block diagram of a LACAMP module. Each module handled 16 LAC channels, providing pulse height and time-of-arrival information, as well as calibration circuitry.

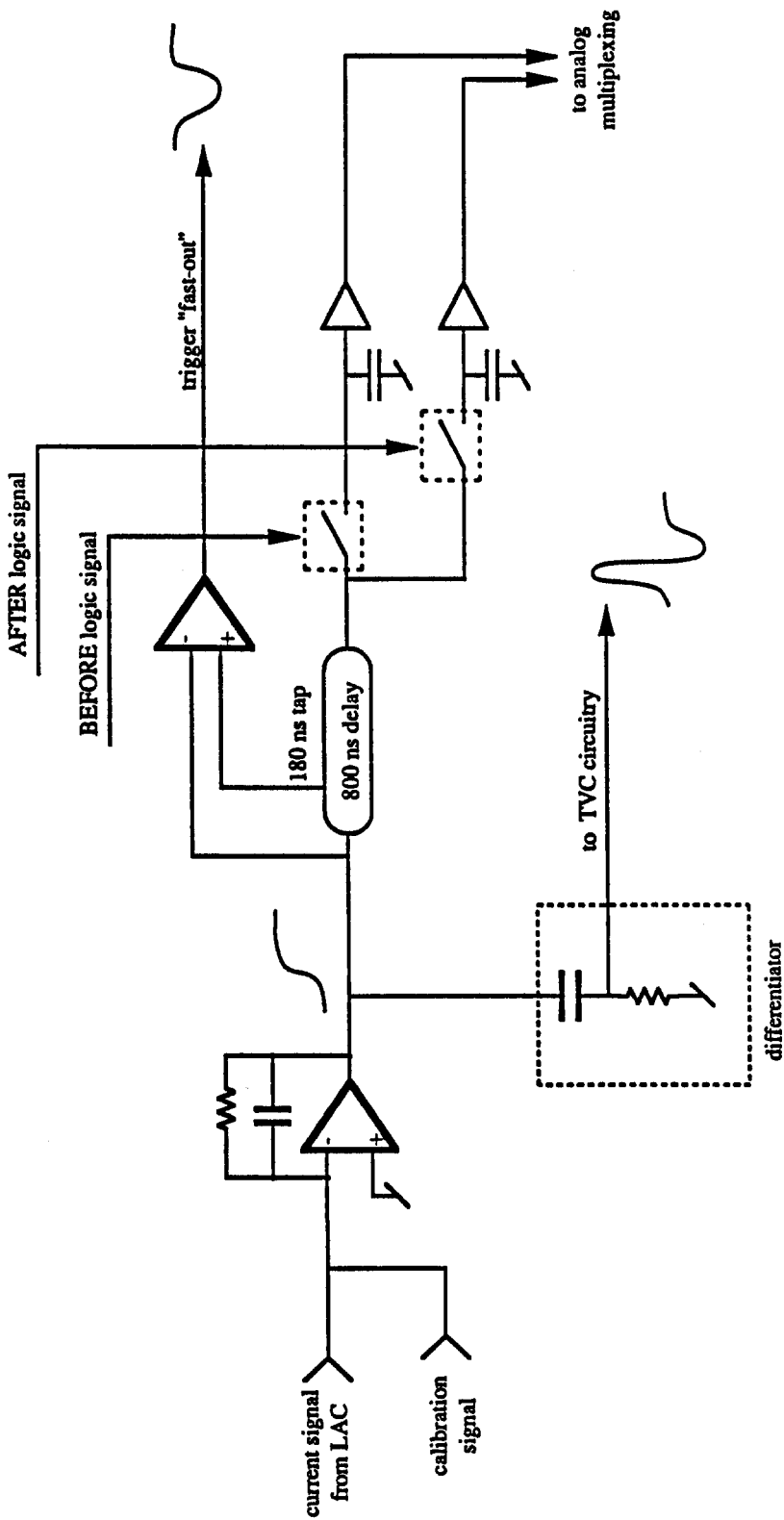


Figure 24 – Schematic of single LACAMP channel.

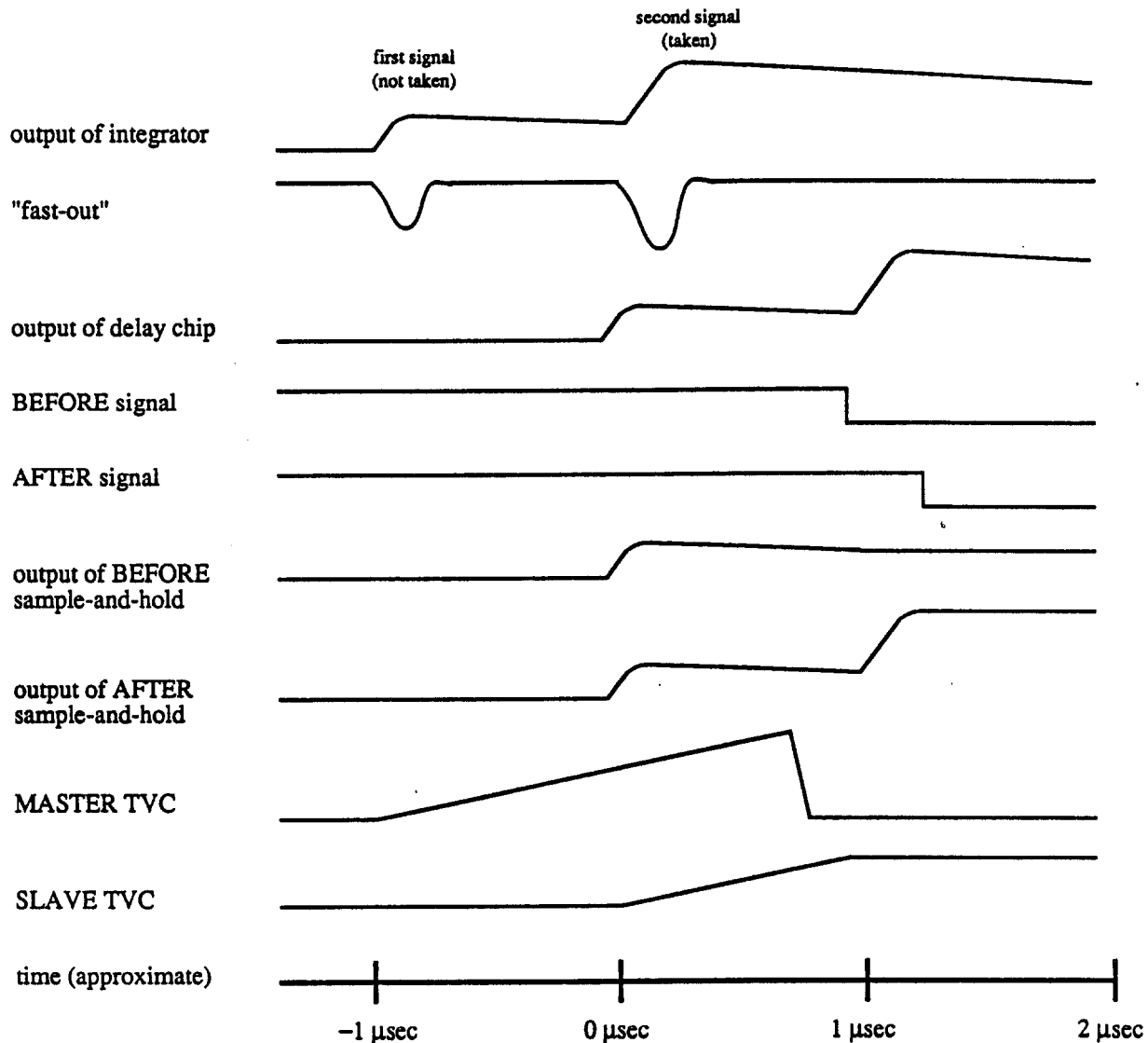


Figure 25 – LACAMP EVENT sequence. In this case, one event occurs which does not satisfy the experimental trigger requirements. Shortly thereafter, a second event comes which does satisfy the trigger.

out, at which point a reset pulse was sent to the BAT modules. This cleared the BEFORE and AFTER signal and thus re-enabled the amplifiers*.

Fast-out Signals

Referring again to figure 24, we see that the delay chip also provided an output with 180 ns of delay, relative to the input, so the value of this output was always equal to the value the input had 180 ns earlier. By taking the difference between these two values, a short, negative polarity pulse was produced, with a pulse height proportional to the integrated signal*. This pulse, called a "fast-out" was transmitted through a connector at the front of the LACAMP module to be used in making the trigger decision, as will be discussed in the next chapter.

Event Timing

Even with the BEFORE-AFTER subtraction, the LACAMP channels were still sensitive to multiple events if they occurred within a few hundred nanoseconds of the triggering event. For this reason, Time-to-Voltage Conversion (TVC) circuitry was built in to the amplifier module.

The operation of the timing circuitry is illustrated in figure 26. The value of each integration amplifier was differentiated to provide a very short pulse. These pulses were then summed for each four adjacent amplifier channels. The sums were compared to a crate-wide threshold set by the BAT. If a sum was over this threshold, the MASTER TVC circuit was triggered. This caused a current source to charge a capacitor at a constant rate. The current was stopped by the arrival of the BEFORE signal, i.e. when the trigger requirements were satisfied. Thus, the voltage across the capacitor represented the amount of time between the deposition of energy in the calorimeter and the arrival of the trigger signal. If no BEFORE signal arrived (i.e. the event did not satisfy the trigger

* Actually, the trigger pulse was sent to the BAT electronics after only the preliminary trigger requirements had been satisfied, so most of the time the system was reset without actually reading out the event.

* This is because the shape of the integrated signal was the same for different size pulses. In other words, the signal value at 180 ns always represented roughly the same fraction of the final signal value.

requirements), the circuit reset itself after $\approx 1.5 \mu\text{sec}$. The BEFORE signal was timed to always arrive $\approx 800 \text{ ns}$ after the triggering event, so the TVC value would be roughly half of full scale for energy depositions which were "in-time" with the correct interaction. While the MASTER TVC was active, a functionally identical SLAVE TVC was enabled in case another event occurred before the $1.5 \mu\text{sec}$. Referring again to figure 25, we see the function of the two TVC circuits. In this illustration, one event arrives, triggering the MASTER TVC, but failing to satisfy the experimental trigger. Shortly thereafter, a second signal arrives, which does satisfy the experimental trigger. Its time is then recorded by the SLAVE TVC.

Since there was one MASTER/SLAVE pair for every four amplifier channels, there were a total of four pairs or eight TVC channels per LACAMP module. The value of each of these TVC channels was selected and transmitted to the EWE during readout of the event.

Calibration Circuitry

In order to measure the relative gains amplifier channels, the LACAMP modules included built-in charge injection circuitry. Under the control of the MX processor, a pulse could be injected into a specified amplifier channel within a given crate. This was done by initiating a BAT timing sequence called the CALIBRATION sequence. In this sequence, the injection of the pulse was followed by the standard EVENT sequence, so that the response of the amplifier to the pulse could be measured. The height of the pulse was adjustable, as was the time between the pulse and the subsequent EVENT sequence. By varying the pulse height, the amplifier channels could be calibrated. Similarly, by varying the time between the pulse and the EVENT sequence, the timing circuitry could be calibrated. Optionally, two pulses could be sent to the same channel, a few hundred nanoseconds apart. This was so that both the MASTER TVC and the SLAVE TVC would be triggered. Otherwise, there would have been no way to calibrate the SLAVE TVC.

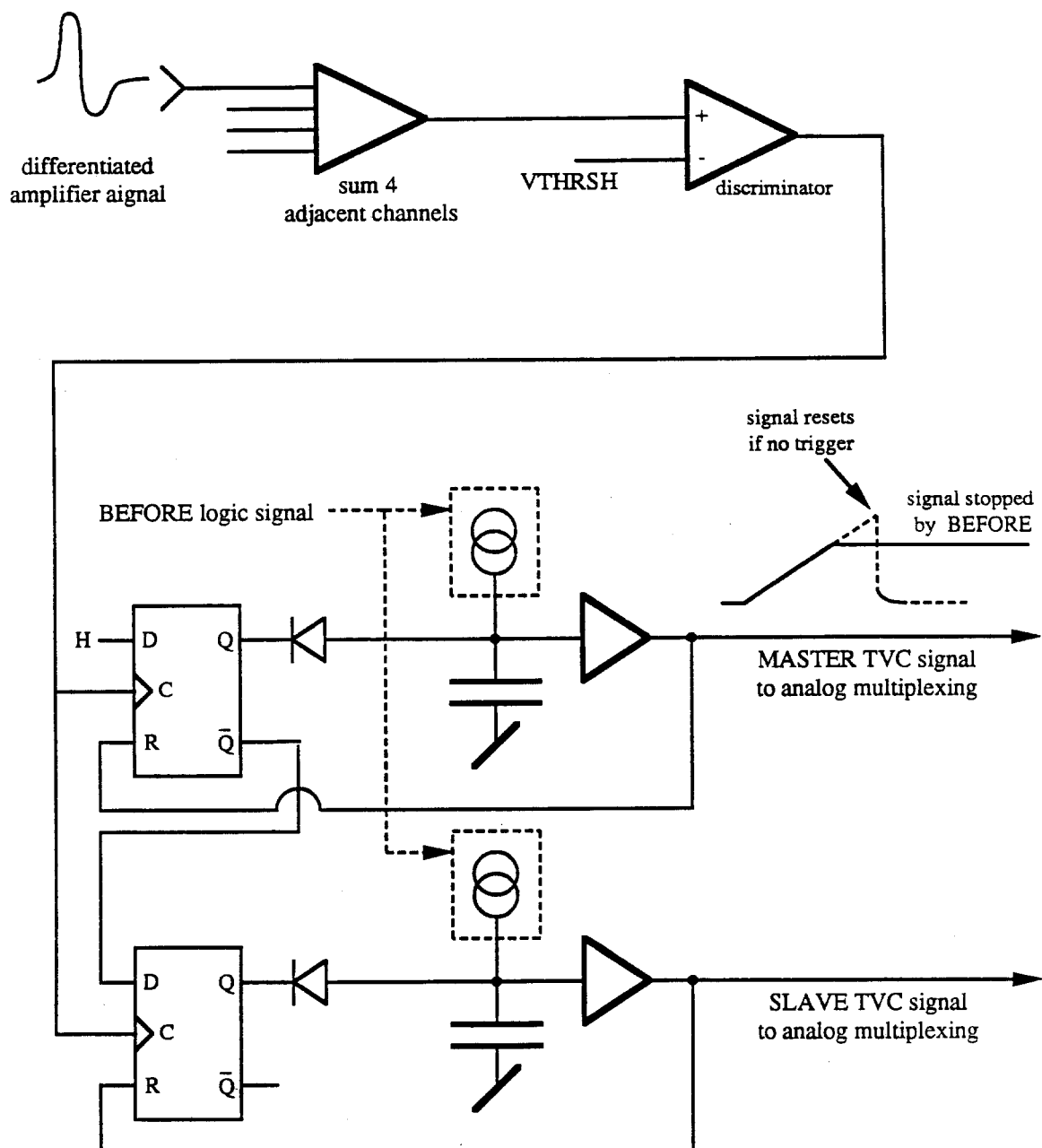


Figure 26 – TVC Channel

4.3 E706 RABBIT CONFIGURATION AND USAGE

Recall that there were approximately 6200 channels in the EMLAC and 2350 in the HADLAC. With 16 channels in each LACAMP module, this required about 540 modules. These were arranged in 28 RABBIT crates mounted around the perimeter of the LAC cryostat within the Faraday room. Twenty of the crates were dedicated to the EMLAC and the remaining eight were dedicated to the HALAC.

All communication with the RABBIT crates was mediated by a system of *optical couplers* at the North wall of the Faraday room. These converted logic levels to optical pulses, which crossed the Faraday room wall, and were then converted back to logic levels, thus filtering any transient electronic noise which might have been transmitted into the Faraday room along the cables.

The LACAMP crates were controlled by a total of nine MXs, eight handling three crates each, and one handling 4 crates. The MXs were located outside the Faraday room, some distance away. The crates were configured in the redundant manner described above, i.e. two EWEs in each crate. In general, each EWE was used to read out half the modules in its crate. The MXs performed several *tasks*, related to the control and readout of the crates:

- LACREAD - was the most crucial MX task. It performed the actual readout of the detector. The MX would direct each of EWEs under its control to begin a digitization sequence on one channel (i.e. two channels per crate). It would then monitor the status of the EWEs. If a channel did not exceed the zero-suppression threshold, the MX would direct the EWE to start a digitization on the next channel in its half of the crate. If the channel did exceed the threshold, the digitization would be completed and the resulting value stored in memory buffer within the MX. The EWE would then be directed to start the digitization sequence on the next channel. This task was complete when all of the EWEs had completely scanned the channels assigned to them. Because only values which exceeded the

zero-suppression threshold were stored, it was necessary to store a unique number with each digitized value, indicating the location in the detector from which it came.

- PEDSET - determined the pedestals of the LAC channels, i.e. the value on the amplifier when no signal was present. This was done by initiating a EVENT sequence within the crate, and then digitizing all the amplifier channels. An average was taken of 128 reads to determine the pedestal values.
- CALSUB - calibrated the amplifier and TVC channels. By using the pulse injection circuitry, described in the last section, this task calibrated the amplifier channels by taking an average of 8 readings for each of 5 calibration pulse heights to each channel. To calibrate the TVC channels, two pulses were sent to the appropriate amplifier channel, thus triggering both the MASTER and the slave TVCs. The position of the EVENT sequence relative to these pulses was then varied. Again, an average of 8 readings was taken for each of 5 different time values.

The MXs were in turn controlled by a PDP-11/45TM computer, which was part of the data aquisition system. When an experimental trigger was satisfied, this computer would instruct all of the MXs to begin the LACREAD task in parallel. It typically took about 17 milliseconds to read out the entire LAC in this way. The other MX tasks were performed about once every four hours, or when there were changes in the LAC electronics.

4.4 TRACKING SYSTEM

The individual SSD modules were mounted to fan-out boards, which channeled signals from the actual strips to preamplifiers mounted around the sides of each board. These amplified and shaped the signals to make them similar to the signals from the PWC modules. The was done so that the entire tracking system could be read out by a common system.

The tracking system was read out by the MWPC-1TM system, built by Nanometric Systems, Inc.^[33] This system included 16 channel amplifier/discriminator modules to convert the current pulses from the planes into logic pulses. These logic pulses were then sent to *latch* modules which delayed the signals by a programmable amount to allow a trigger decision to be made. After the delay, the state of the signals was held, or latched, if the trigger is satisfied. The latch modules resided in crates which followed the CAMAC standard^[34].

Note that data from the SSD and PWC planes were treated as digital, i.e. information was only recorded as to whether a strip or wire was "hit" by a passing track, with no information as to actual pulse height.

4.5 DATA ACQUISITION

Figure 27 shows the E706 Data Acquisition system as it was configured during the running period. The various individual systems were read out by four Digital PDP-11TM computers, referred to as: "MX", "ROCH", "NEU", and "MU". Their individual tasks were as follows:

- MX - communicated with the MXs controlling the LAC electronics. This PDP-11 sent instructions to the MXs and read out the memory buffers containing event data. This PDP-11 also controlled the configuration of the p_T system (discussed in chapter 5).
- ROCH - read out data from the forward calorimeter.
- NEU - read out data from the tracking chambers, via the MWPC-1 system described above. This computer also had the important task of controlling the trigger logic (discussed in chapter 5) and recording the state of that logic, as well as the state of the Cerenkov detector, for each event.
- MU - read out data from the E672 spectrometer, which was recorded along with the E706 data.

When the requirements of the experimental trigger were satisfied, each PDP-11 would receive a logic signal, causing it to read out the devices for which it

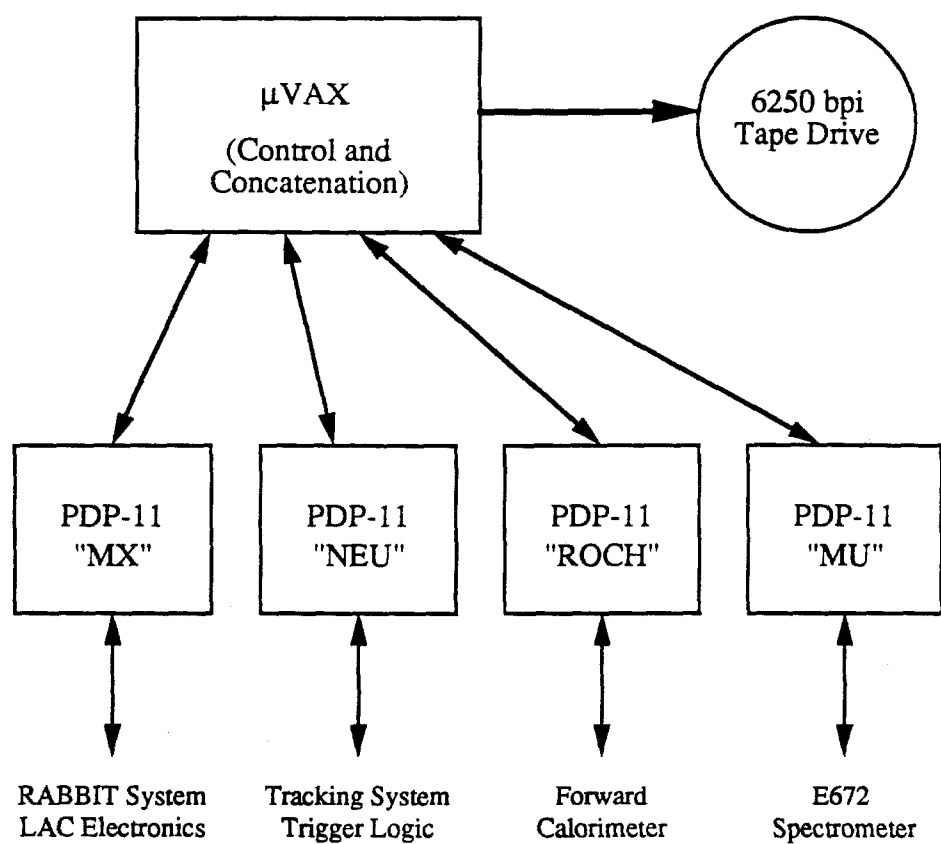


Figure 27 – E706 Data Acquisition System

was responsible. Each of these computers had the internal memory to hold information from several events. Data were then transmitted to a Digital μ VAX IITM computer. This computer ran a program called EVENT_BUILDER, which *concatenated* the information from each of the systems into single blocks, representing individual events. Because many separate systems were involved, each sending several events worth of data to the μ VAX at a time, it was necessary to have some criterion to match the data from one system to data corresponding to the same event from the other systems, e.g. to match appropriate information from the tracking system and the LAC. A device called a "Hydra-Scaler" was used for this purpose. This module stored an "event number", which could be read simultaneously by all of the PDP-11s. This number was initialized by the NEU PDP-11, and was incremented by each successive trigger pulse. The information from each event was tagged with this unique number within each PDP-11. The EVENT_BUILDER program then used this number match data for concatenation. The concatenated events were then written onto standard nine track computer tape. Each tape held data from approximately 12,000 events. To read out the entire spectrometer took on the order of 25 ms/event.

The recording of the experimental data was divided into *runs*^{*}. The maximum length of a run was the period over which experimental conditions did not change, or the length of a single tape, whichever was shorter. At the beginning of each run, the experimenters had the option of initiating a *cold start*, which performed several initialization tasks within the system, including the PEDSET and CALSUB tasks described in the previous section.

* The term "run" is ambiguous in high energy physics. It refers both to an entire period of data taking, often lasting months, and to the short divisions of that period defined here.

5. The Experimental Trigger

5.1 PRINCIPLE

The trigger was designed to select events containing a high- p_T (> 3 GeV/c) photon or π^0 . Experimentally, the signature of such events would be localized energy deposition within the EMLAC of a relatively large magnitude. Specifically, the p_T would be represented by

$$p_T = E \times \sin(\theta) \quad (5.1)$$

where E was the amount of energy which was deposited and θ was the production angle, i.e. the angle between the beamline and a line from the target to the point of deposition.

The r - ϕ geometry of the EMLAC was well suited to the measurement of p_T , and indeed that was the major motivating factor in the design. The amount of p_T in a given r region of a particular octant* was given by

$$p_T = \sum_i e_i \times \sin(\theta_i) \quad (5.2)$$

where the sum was over the front and back EMLAC strips within the region, e_i was the energy which was deposited in a given strip, and θ_i was the production angle corresponding to that strip.

Recall that the amplifier modules used for the EMLAC (section 4.2) provided short pulses proportional to the energy deposited in each strip. The trigger electronics utilized the “fast-out” signals from the EMLAC r strips to select events containing high- p_T photons or di-photons. The p_T depositions were calculated by a dedicated system of electronics called the “ p_T system”, which will be discussed in detail shortly.

* “ r ” here refers to the radius at the front of the EMLAC. Recall that the EMLAC strips were focused.

5.2 IMAGE CHARGE

At this time it is necessary to discuss an unforseen feature of the electromagnetic calorimeter, which complicated the formation of the summed p_T signal. This discussion is intended to give the reader some understanding of certain subtleties of the experimental trigger.

In the EMLAC, current signal was induced by drifting electric charge within the argon ionization gaps. Ideally, the current from a given strip was to have flowed through the signal cable to the charge integration amplifier, and then returned to the high voltage plates via the ballast capacitors, completing the circuit.

Unfortunately, because of unforseen impedances in the ground path between the amplifiers and the ballast capacitors, current tended to flow through the amplifiers connected to the other strips in the octant. The circuit was then completed via the capacitive coupling between these strips and the high voltage plates. This occurred during the early phases of pulse formation (≈ 200 ns). On a somewhat longer time scale, current would flow from the ballast capacitors to the high voltage planes to balance the charge loss. This too would cause small current signals to flow through the amplifiers of the octant.

The result was that when energy was deposited in a given strip, small signals of opposite sign would be induced on all the other channels in same octant, view, and section of the EMLAC.

For individual channels, these *image charge* signals were a negligible effect. In the p_T system, which summed large numbers of channels together, this was a major problem. Figure 28 illustrates the effect. The top curve shows the pulse from the actual shower[†]. The middle curve was the sum of the image charge induced on the other strips within the octant. The early "wrong-sign" portion of the image charge signal was due to the signal current coupling through the other amplifiers in the octant, while the later "right-sign" part was induced by

[†] Recall that the fast-out signals were of negative polarity

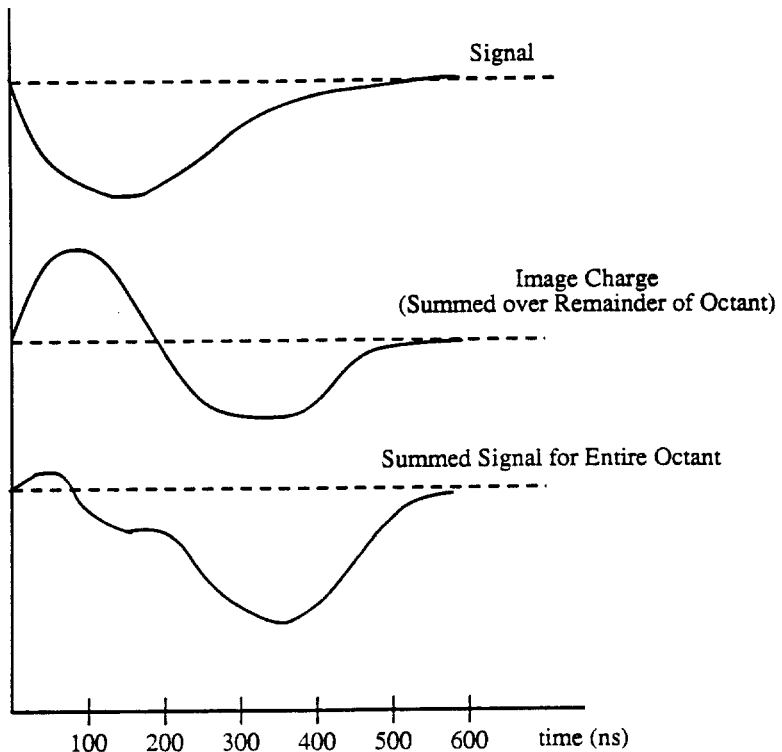


Figure 28 – The effect of image charge.

the current flow from the ballast capacitor to the high voltage plane. Clearly, the summed signal in the bottom curve would have been of little use in forming a trigger. Also, the image charge signal varied with the position in the octant. This was because the area of the r strips increased with increasing radius, thus increasing the capacitive coupling to the high voltage plates. This was compounded by the fact that in order to represent p_T , the signals were summed with a higher weight as r position increased. The effect was that in certain cases, the magnitude of the image charge “ p_T ” exceeded that of the actual p_T . In order to combat these problems, an attempt was made to only sum signals with the correct sign. This will be described in the next section.

5.3 THE p_T SYSTEM

To form the summed p_T signals necessary for the trigger decision, E706 utilized a system of custom modules, designed to operate within the RABBIT standard (see discussion, section 4.1). These modules resided in eight dedicated RABBIT crates, one for each octant, which were located just beneath the RABBIT crates containing the corresponding LAC amplifiers. A single MX processor controlled the entire p_T system.

Figure 29 shows a conceptual view of signal summing for a single EMLAC octant. The fast-out pulses from the r view amplifiers were connected to *local p_T modules* (figure 30), which weighted the signal for each r strip by a value proportional to $\sin(\theta)$, where θ was production angle, relative to the beam direction, corresponding to the strip. These modules then formed sums for each group of 8 adjacent r strips, as well as a total sum for all 32 adjacent r strips which were input. The resulting signals were referred to as the "sum-of-8" and the "sum-of-32" signals, respectively. Because of the $\sin(\theta)$ weighting, these summed signals represented the integrated amount of p_T deposited in the EMLAC over the given r region.

The sum-of-8 signals were connected to a *local discriminator modules* (figure 31). In these modules, signals from corresponding groups in the front and back of the EMLAC were added. From these, sums were formed which represented groups of 16 strips (8 cm), overlapping each other by 8 (4 cm). If one of these sums exceeded a specified threshold, the module produced a logic signal which indicated that there had been a local deposition of p_T somewhere within the octant. There were two local discriminator modules for each octant. Each monitored the entire octant with a different threshold. These produced logic signals referred to as LOCAL_PT_HI and LOCAL_PT_LO, indicating the relative magnitudes of the thresholds. Because these modules summed signals over just 32 strips, image charge effects were not a serious problem.

In each octant, the sum-of-32 signals were connected to a *global p_T module*, which formed the total p_T sum for the octant. Initially, these modules were

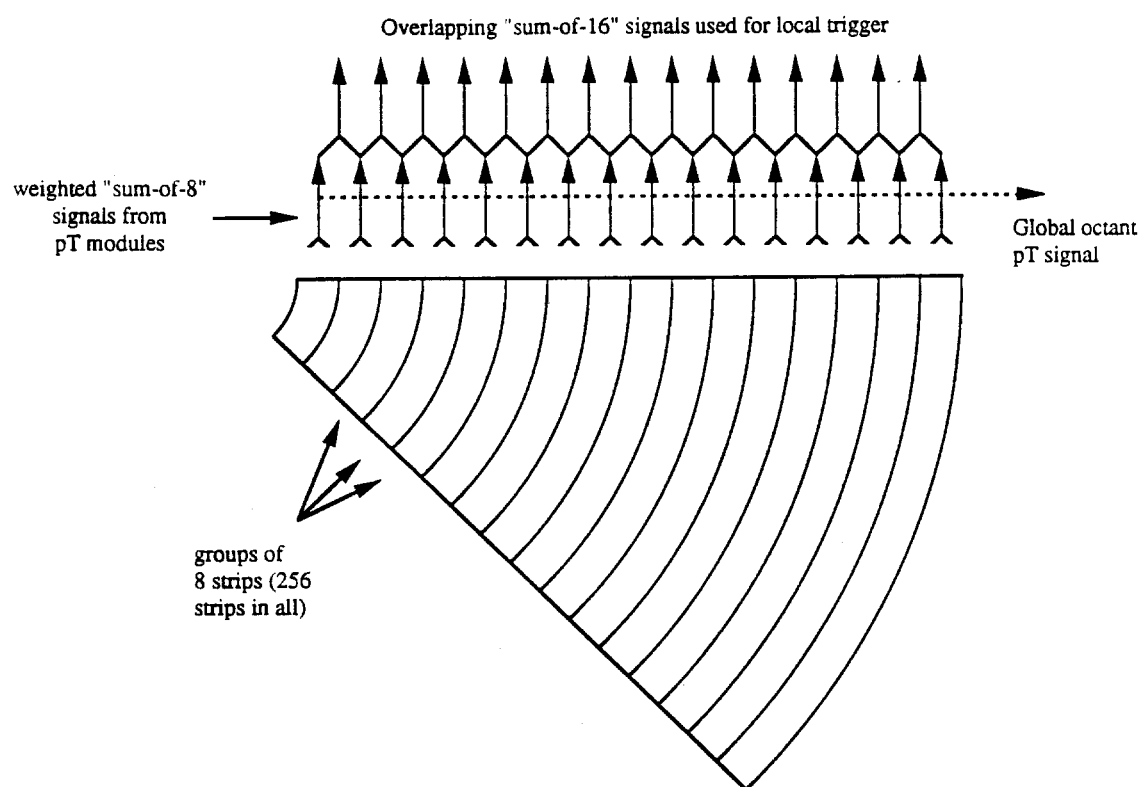


Figure 29 – p_T summing within one EMLAC octant. Energy depositions were weighted according their value of $\sin(\theta)$, so as to represent p_T .

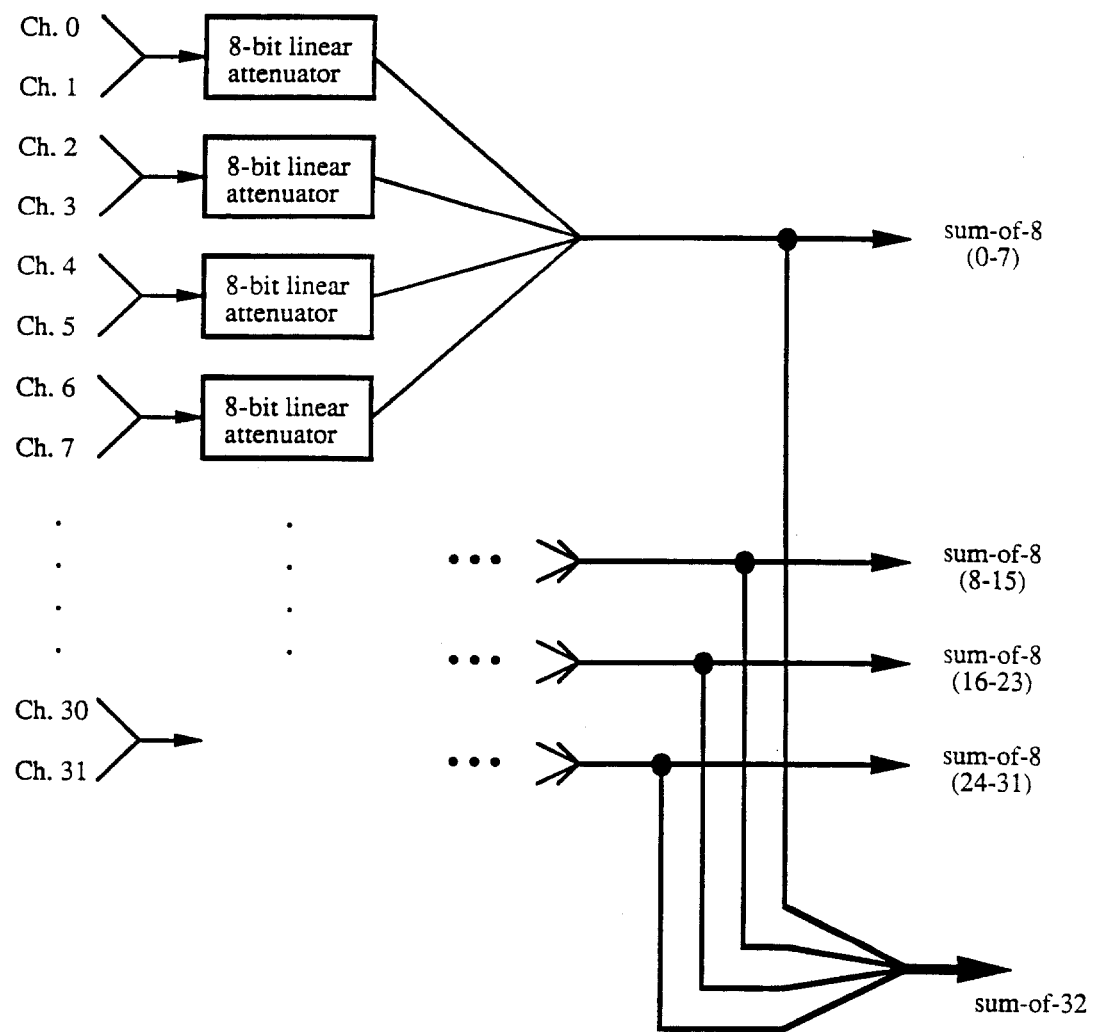


Figure 30 – Local p_T module. These modules produced p_T signals for groups of 8 and 32 strips.

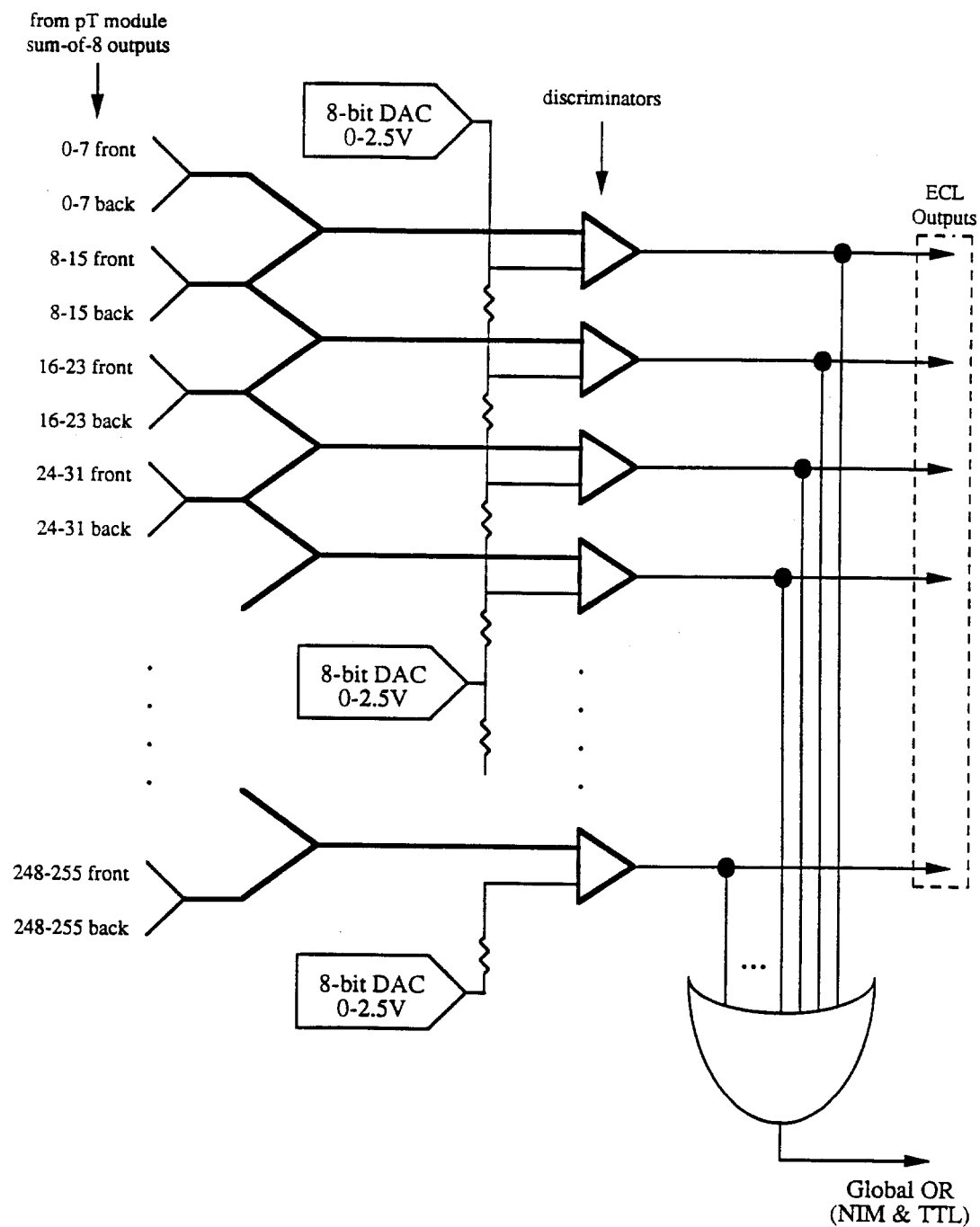


Figure 31 – Local discriminator module. These modules detected localized deposition of p_T within the EMLAC.

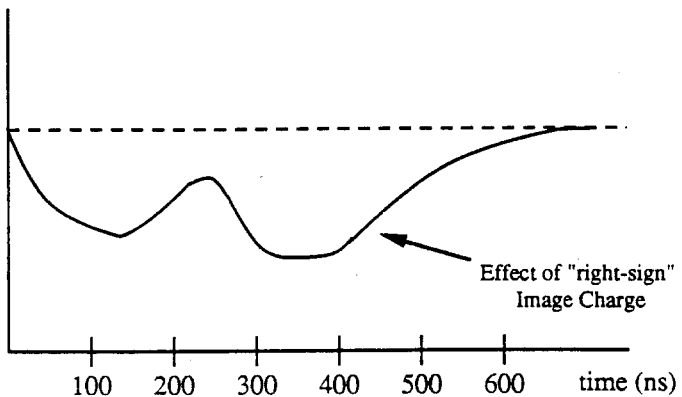


Figure 32 – Summed p_T signal using only right-sign pulses. Notice that image charge is still an issue.

identical to the local p_T modules. However, because of the large number of strips involved (≈ 500 for each octant), image charge effects made this scheme unworkable. To solve this problem, the global p_T modules were modified to reject wrong-sign signal. Of course, the later right-sign portion of the image charge still presented a problem (see figure 32), but steps were taken in the trigger logic to differentiate between this and actual p_T deposition (discussed below). Ultimately, however, the outermost 32 r strips were not used in p_T summing, because of severe image charge effects.

All the gains and thresholds within the p_T system were set by the MX which controlled it. This configuration was done during a cold start operation (see section 4.5).

5.4 TRIGGER LOGIC

The lowest order trigger definition was controlled by several scintillation counters, which are shown in Figure 33. A beam particle was indicated by a signal in the BA and BB counters. The absence of a signal in the BH counter determined that the particle did not come from the beam halo. If an interac-

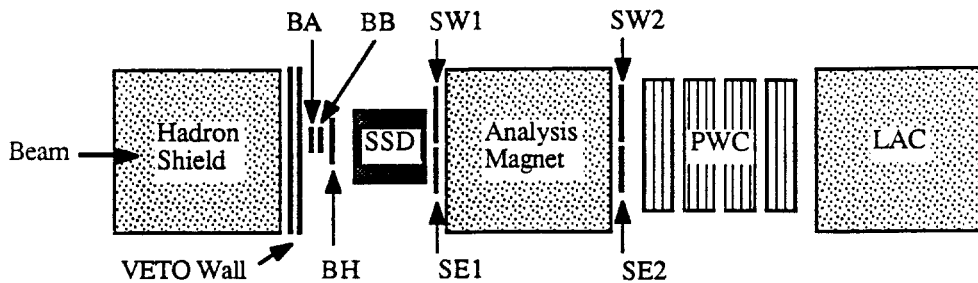


Figure 33 – Scintillation counter configuration

tion occurred, there would be a signal in at least one of the interaction counters (SW1, SW2, SE1, or SE2). Therefore, a logical interaction signal was then defined by

$$BA \bullet BB \bullet (\text{any interaction counter}) \bullet \overline{BH}$$

in coincidence with the beam clock*. This signal was rejected if there was another interaction within ± 60 ns. If not, a *clean* interaction signal was generated. If this coincided with the deposition of at least 1.7 GeV/c of p_T in any EMLAC octant, as determined by the global p_T modules, and did not coincide with the logical AND of the veto wall signals†, a PRETRIGGER strobe was issued. At this point, an EVENT sequence was initiated in the LAC electronics, latching the analog data (see section 4.2). The PRETRIGGER strobe also latched data in the tracking system.

* The accelerator delivered particles to the experimental hall in discreet bunches, called "buckets", spaced 19.4 ns apart, the beam clock logic signal was synchronized with the arrival of these buckets.

† The veto wall planes, located just downstream of the hadron shield, detected muons resulting from the decay of beam particles. These muons often deposited energy in the EMLAC through bremsstrahlung, mimicking direct photons. This issue will be discussed in detail in chapter 7.

For each quadrant, the signals from the global p_T modules of the two octants were added to form a total p_T signal. If this signal satisfied a minimum threshold, in coincidence with the PRETRIGGER strobe, a GLOBAL_PT_LO signal was generated. If a somewhat higher threshold was satisfied, a GLOBAL_PT_HI signal was also generated. The nominal values for these thresholds are shown in table 7, as are those for the LOCAL_PT signals, generated by the local discriminator modules. Notice that several changes were made while data were being taken.

Logic Signal	Threshold (GeV/c)			
	runs: 1811 - 2292	2293-2310	2311 - 2904	2905-3036
LOCAL_PT_LO	1.2			
LOCAL_PT_HI	4.2	3.6	3.0	
GLOBAL_PT_LO	2.5			
GLOBAL_PT_HI	4.0	3.6		

Table 7 – Trigger threshold setting by run number.

These logic signals were used to form several “LAC-based” triggers:

- *Local-Global-Hi*, defined by a logical AND of the GLOBAL_PT_HI and LOCAL_PT_LO logic signals, indicated that a large amount of p_T had been deposited in a quadrant, with some amount of it localized to a small region within one of the octants.
- *Single-Local*, defined simply by the LOCAL_PT_HI logic signal, indicated that a large amount of p_T had been deposited in a small region (4-8 cm in r) of a single octant. This trigger was very efficient at detecting single photons and π^0 decays.
- *Local-Global-Lo*, defined by the logical AND of the GLOBAL_PT_LO and LOCAL_PT_LO logic signals, was similar to the *Local-Global-Hi* trigger, but with a lower threshold. It was implemented to study the performance

of the *Local-Global-Hi* trigger. Because of the higher incidence of these lower p_T events, this trigger was prescaled by 10, i.e. it only triggered the detector once for every 10 times it was satisfied.

- *Two-Gamma* - defined by the logical AND of the LOCAL_PT_LO signal from one octant with the LOCAL_PT_LO signal from any of the three octants on the opposite side of the EMLAC, was designed to study massive two-photon decays.

These trigger signals would be rejected if there was coherent noise detected in the Faraday room electronics, or if there had been a previous deposition of greater than 1.7 GeV/c of p_T in the EMLAC, within the previous 300 ns. The latter was to protect from pile-up effects resulting from the relatively slow response of the LAC electronics. Also, for events which did not satisfy the trigger, this prevented the right-sign portion of the image charge signal from causing a subsequent trigger through the accidental coincidence with an interaction.

For diagnostic purposes, triggers were also defined based simply on beam and interaction definitions. These were drastically prescaled to prevent them from dominating the data rate. Triggers were also generated by the E672 experiment, but these have no relevance to this analysis.

If a trigger was satisfied, a pulse was sent to the data acquisition system to read out the event. Further triggers were blocked until this was complete. If a PRETRIGGER pulse had been sent, but no trigger satisfied, a signal was sent to reset the electronics for the LAC and tracking system, enabling them for future events. Otherwise, all electronics would be reset when the readout of the spectrometer was complete.

Trigger logic was implemented primarily using programmable logic modules, which operated within the CAMAC standard. The system allowed the state of the trigger logic to be read out and recorded along with the data from every event.

6. Event Reconstruction

6.1 OVERVIEW

The software framework for event reconstruction in E706 was provided by the MAGIC program, written primarily by George Alverson and Ed Pothier of Northeastern University. The program was based on the ZEBRA memory management package^[35] developed at CERN.

The first task of the MAGIC program was to read the data which were written to tape by the data acquisition system and *unpack* them into a meaningful form, e.g. a pulse height in a particular channel of the EMLAC. A separate routine unpacked the data from each part of the detector.

A reconstruction routine was executed for each part of the spectrometer. The routines of interest to this analysis are EMREC, which reconstructed electromagnetic showers within the electromagnetic calorimeter, and PLREC, which reconstructed charged tracks and located the interaction vertex. These routines will be discussed in the following sections.

Through the use of various software "switches", routines within MAGIC could be "turned on" or "turned off". For example, if one wished, only charged tracks could be reconstructed, thus saving time in program execution. There was also the provision to store data at various stages of the process, e.g. after unpacking and before reconstruction. Likewise, data could be input in any form - initial, unpacked, or fully reconstructed. There was also the capability to use simulated, or *Monte Carlo*, data to test software performance.

To reconstruct the data used in this analysis, the MAGIC program was run using the Fermilab Advanced Computing Project (ACP)^[36]. This consisted of a digital μ VAX computer, which controlled many (\approx 20-60) dedicated processor *nodes*, which were based on Motorola 68000TM processor chips. The μ VAX read the spectrometer data from tape and downloaded data from one event to each processor node. Each node would then perform the unpacking and reconstruction for a single event. When a node completed this task, the results

would be sent back to the μ VAX, which would write them to an output tape and load the node with another event.

6.2 ELECTROMAGNETIC RECONSTRUCTION

It was the job of the electromagnetic reconstruction program to use the data on energy deposition in the EMLAC to reconstruct the energy and position of the incident photons which gave rise to it. From the reconstruction standpoint, the quadrants of the EMLAC were treated as independent entities. Recall that each quadrant was divided into front and back sections. The sections were each divided into four views: left- r , right- r , inner- ϕ , and outer- ϕ , numbered respectively.

Unpacking

In the unpacking routine, called EMUNP, the raw datum from each strip was converted to deposited energy e_i , based on the formula:

$$e_i = A_{em} G_i (N_i - N_i^0) \quad (6.1)$$

where N_i was the digitized value of the pulse height in the channel. N_i^0 was the pedestal for the channel, as returned by the PEDSET routine (see discussion, section 4.3). A_{em} was the nominal normalization of the EMLAC, which was roughly determined from electron beam data to be about 3.1 MeV/(ADC count)^{*}. G_i was the relative value of the channel gain, as determined from the CALSUB routine. At this point, there was also a correction for bad strips. There were some strips in the calorimeter which were known to have problems, either shorts or bad connections, rendering them unusable. In addition, amplifier channels occasionally stopped functioning. This was indicated by anomalous result from the calibration task. In these cases, the strip was deemed “dead”, and it was given a value equal to the average of the two adjacent strips.

* Ultimately, the energy scale was precisely determined by requiring the π^0 mass, as measured with $\gamma\gamma$ decays, to have the accepted value of 135 MeV. This resulted in corrections to the reconstructed photon energies, which were applied at a later stage in the analysis.

Also in the unpacking routine, signals from corresponding strips in the front and back sections are added together. This formed a conceptual third section in the EMLAC, called the "summed section". Except where otherwise noted, the pattern recognition code operated on these summed signals.

Position and Energy Reconstruction

The general philosophy of the electromagnetic reconstruction routine (EMREC) was to find clusters of energy corresponding to photon depositions separately in r and ϕ views. It would then match these based on the fact that photons would deposit roughly the same amount of energy in each view.

The first stage of reconstruction was to find *groups* within each view. A group was defined as at least three adjacent strips (two in outer- ϕ) which had an energy above a specified threshold. Constraints were also made on the total energy of the group and on the average energy per strip.

At this point, each group was searched for *peaks*. A peak was defined as the point where the derivative of the energy distribution changed from positive to negative. Each peak was located between two *valleys*, defined as either the low point between two peaks, or the end strip of the group. The position of each peak was calculated using the three central strips. For each peak found in the summed section, the peak finding algorithm was applied again, this time using only the energy from the front section. This was to see if it was in fact two peaks which had coalesced. If this was the case, the energy of the original peak was divided between two new peaks with the positions and relative energies determined by the peaks in the front section.

These peaks were then used to form "gammas", or single-view photons[†]. For single-peak groups, this was just a matter of fitting a parametrized shower shape to the peak and using this to determine the energy. For all fitting algorithms,

[†] To avoid confusion arising from this ambiguous term, the word "gamma" will always appear in quotes when used in this context.

the error on each strip was given by

$$\sigma_i = \sqrt{(.1)^2 + (0.14)^2 e_i} \quad (6.2)$$

where e_i was the energy in the strip. This function represented the predicted energy resolution of the EMLAC. For multiple peak groups, the following function was minimized

$$\chi^2 = \sum_i \frac{1}{\sigma_i^2} (e_i - \sum_k E_k f_k^i)^2 \quad (6.3)$$

where f_k^i was the fraction of the energy from shower k which would be deposited in strip i , based on the parametrized shower shape. This minimization could be explicitly solved for the individual shower energies E_k ^[37]. Once the energies were found, the energy distribution for each individual shower was found by subtracting the contribution from all other showers in the group. The resulting distribution was used to calculate a new position for the shower. Using these new positions, (6.2) was recalculated and minimized to yield the final "gamma" energies. For r view "gammas", an attempt was made to find the position in both the front and the back sections, to be used in determining the direction of the incident particle. This will be discussed in the next chapter.

The final stage of reconstruction was to correlate the "gammas" from different views to form final photons. This procedure took advantage of the interleaved structure of the EMLAC, which meant that showers would have roughly the same longitudinal energy profile in r and ϕ . Therefore, both the total energy, and the ratio of the front and back energies would be very close in the two views. The correlation algorithm used these as its matching criteria. The process was conceptually simple but was complicated by several things in practice. If a photon fell near the inner- ϕ /outer- ϕ boundary, for example, one r view "gamma" had to be correlated with two ϕ view "gammas". Similar problems occurred at the right- r /left- r boundary. Also, two photons often had very close r positions while being separated in ϕ and vice versa. In this case they appeared as a single "gamma" in one view, which had to have its energy split between two (or more)

gammas in the other view. Final photon energies were the sum of the energies from all contributing views.

After correlation, the ϕ view "gammas" were reconstructed again. This was because the ϕ strip width varied with r position, introducing some uncertainty in the first stage shower fitting. Refitting with a known r position yielded a more accurate energy. The resulting correction was applied to the final photon energy.

Time of Arrival

Because the response of the EMLAC was slow relative to the arrival of beam particles in the hall, it was important to assign a time to each photon, so that "out-of-time" information could be rejected. This was done using information from the timing circuitry (TVCs) within the amplifier modules (see section 4.2). The task was complicated by two things. First, because the TVCs were fired by differentiated signals, there was a problem with high frequency noise, which caused random firing of the TVC circuitry. These spurious signals were eliminated during reconstruction by requiring energy in the strips associated with the TVC; however, they did result in inefficiency by blocking true signals. The second problem was to assign a "pedestal" to each channel. This was difficult because, unlike amplifier channels, the pedestal of interest was not the value when there is no signal, but rather the value when energy is deposited "in-time" with the event.

Data returned from the MX calibration routine (CALSUB, section 4.3) were used to determine TVC pedestals. Recall that this routine returned TVC readings for several values of the time interval between a calibration pulse and a trigger signal. This information was used to determine the value for each TVC which corresponded to an in-time event.

While unpacking the EMLAC data, the total energy of the four amplifier channels associated with each TVC was calculated. If it was below 4.0 GeV, the

TVC was rejected. Otherwise the time for that TVC (t_i) was given by

$$t_i \text{ (ns)} = A_{ADC}(T_i - T_i^0 - C(E_i)) \quad (6.4)$$

where A was the conversion from ADC counts to nanoseconds. T_i was the digitized value of the TVC voltage. T_i^0 was the pedestal (described above). The final term $C(E_i)$ corrected for the fact that lower energy pulses tended to trigger the TVCs somewhat later than higher energy pulses* ; thus, the time had to be adjusted based on the energy (E_i) associated with the TVC.

Each EMREC group was assigned a time based on the TVCs associated with it. Because there was often information within the group from more than one event, an attempt was made to find *clusters* of TVCs with similar readings. These clusters were formed by taking each TVC value in the group, and searching for other TVC values within 45 ns of it. Thus there was a cluster associated with each TVC from the EMREC group. An energy weighted time for each cluster (t_c) was then calculated as

$$t_c = (\sum_i t_i * E_i) / (\sum_i E_i) \quad (6.5)$$

where E_i was the energy associated with the i th TVC in the cluster. The times were then ranked for each EMREC group according to the following criteria (in descending order of importance):

- which cluster contained the most TVCs
- which cluster had the most total energy associated with it
- which cluster had the time closest to the interaction time

The two best times were then recorded for each group.

* This was because, for these lower energy signals, the TVC threshold represented a larger fraction of the total pulse height. Therefore, they exceeded the threshold at a somewhat later time than higher energy pulses.

Each "gamma" then inherited the two times of the group from which it was formed. When the final photons were formed, the two best times were calculated from the times of the (up to eight) contributing "gamma"'s, in the same way the group times were calculated from individual TVCs values and stored for the photon. Each photon time was stored with a quality word which encoded the total number of individual TVC values used in its calculation, along with the total amount of energy associated with these TVCs. Because of the problem of spurious hits, a time was not used if less than two TVC values were used in its calculation. In these cases, a photon was assumed to have come in time with the interaction.

6.3 CHARGED TRACK RECONSTRUCTION

The subject of charged track reconstruction, as provided by the PLREC routine, will only be superficially covered here, as precise momentum determination was not necessary to this analysis. The subject is treated extensively elsewhere^[38]. In general, the track reconstruction code attempted to reconstruct tracks separately upstream and downstream of the analysis magnet, then to match the tracks at the magnet to calculate momenta. Upstream track information was then used to calculate the position of the vertex, i.e. the point where the interaction occurred.

Downstream Tracking

The first step was to search for tracks in each of the 4 PWC views (X,Y,U,V). In each view, lines were projected between hits in first plane and hits in the last plane. For each line, the second and third planes were searched for hits within 1.5 wire spacings of the predicted position. If at least one such hit was found (i.e. three hits total), the line was stored along with all corresponding hit positions as a track candidate. This procedure was repeated, this time starting with the second and third planes and searching the first and fourth. Least-square fits were performed on all track candidates, to form "view tracks". Next, an attempt was made to form three-dimensional "space tracks". This was done by pairing

each X-view track with a Y-view track, then searching the U and V planes for hits within 1.5 wire spacings of the position predicted by the X/Y pair. Space track candidates were those for which there were at least two such hits in both the U and the V view, and for which there were a total of at least 13 hits in all four views. A least-square fit was then performed using all the hits from all four views which were associated with the track. This procedure was then repeated, this time starting with the U and V plane and searching the X and Y plane. Finally, a track clean-up was performed to eliminate spurious tracks. If two tracks shared more than a certain number of hits, the track with the higher χ^2 for the fit was rejected. Each of the remaining "downstream space tracks" was stored, along with the χ^2 of the fit and the number of hits (13-16) associated with the track.

Upstream Tracking

Next, view tracks were formed in SSD X and Y views downstream of the target. The algorithm was more or less identical to the algorithm used to form the PWC view tracks. As with the PWCs, a track was required to have hits in at least three of the planes of the four planes. These SSD view tracks were referred to as "upstream tracks". Because there were no diagonal planes in the SSD system, there were no "upstream space tracks". The beam track was also reconstructed in the SSD planes upstream of the target. If there was more than one beam track, then there were ambiguities which ultimately had to be resolved using the vertex position(s).

Linking

Downstream tracks were then *linked*, or matched, to upstream tracks. This was done by projecting each downstream track to the center of the magnet and attempting to find upstream view tracks which projected to match it within .7 cm in each view, correcting for the effects of the magnetic field in the X-view. Because the field bent only in the X-plane, an additional cut was made on the difference in the Y-slopes between the upstream and the downstream

tracks. Often, more than one upstream track linked with each downstream track*. In these cases, up to four upstream tracks in each view were stored for each downstream track, with the closest in each view referred to as the "space track best link". For each best-link pair, the angular difference between the upstream and downstream segments in the X-view was then used to calculate the momentum of the resulting "physics track". The sign was determined by the direction of the bend.

Vertex Finding

Vertices were re-constructed using the SSD tracks in each view. The first step was to determine which set of tracks was to be used in the calculation of the vertex. If there were more than four tracks in the view which had hits in all four planes AND linked to downstream tracks, then this set was used to calculate the vertex. If this condition could not be satisfied, then if there were at least four tracks with hits in all four planes, this set was used, regardless of whether the tracks linked to downstream tracks. If this condition also could not be satisfied, then all tracks which linked to downstream tracks were used, even if they had hits in just three of the planes.

A χ^2 was defined for a given vertex position by

$$\chi^2 = \sum_i \frac{b_i^2}{\sigma_i^2} \quad (6.6)$$

where b_i was the impact parameter of the i th track and σ_i was the error in the projection of the track. The vertex position was calculated by minimizing this sum. If the average impact parameter was less than $20 \mu\text{m}$, or the largest impact parameter was less than $50 \mu\text{m}$, this vertex was kept. Otherwise, the track with the largest impact parameter was eliminated and the vertex position was recalculated. This process was repeated until the above condition was satisfied,

* This was primarily because there were no upstream space tracks. Thus, in a given view, any upstream track could link to any downstream track with no constraints provided by the other view.

or until one track was left, at which point the search would be declared a failure and no vertex would be stored for the event.

The procedure was then repeated for the other view. The vertex found in each view was given a weight of $1/\sigma_z^2$, where σ_z was the error in its z position. The final vertex z position was then calculated by a weighted average of the z positions for the two views.

Re-linking

After the vertex was found, track-linking was performed again, this time with upstream tracks originating from the vertex given preference when there were link ambiguities. If this changed the best link for a given space track, the corresponding physics track was redefined and the momentum was corrected accordingly. Also at this point, additional physics tracks were formed from downstream space tracks for which no link had been found. In these cases, the momentum for each track was calculated assuming the downstream track originated at the vertex.

7. Analysis

7.1 DATA SELECTION

Because this was the first run of E706, much time was spent evaluating the performance of the spectrometer. Nevertheless, enough physics data were taken to do much valuable study.

The data used in this analysis were taken using the *Single-Local* trigger (see discussion, section 5.4). Recall that this trigger required the deposition of a large amount of p_T in small (8 cm), overlapping regions of r , within any of the EMLAC octants*. In the p_T range of interest, the *Single-Local* trigger was very efficient for the detection of both γ 's and π^0 's.

The data taken during the '87-'88 run were divided into 8 sets, delimited by changes in target, beam sign, etc. These were designated A through H, in reverse chronological order. Table 8 shows a breakdown of the data sample used for this analysis. Sets F, G, and H were not analyzed because these data were taken before the *Single-Local* trigger was implemented. Set B data were omitted because the tracking system was not functioning properly during that time. The table shows the total number of events written to tape for each set, along with the beam sign and target type. For runs in which there was more than one target, the reconstructed vertex position was used during analysis to define which target produced a given event.

After reconstruction, a "splitter" program divided the data into several "streams", according to specific analysis interests. At this level, events were considered direct photon or high- p_T π^0 candidates if they satisfied any of the LAC-based triggers. In each of these events, the highest p_T was calculated from among single reconstructed photons and from the vector sums of all photon

* Actually, the *Local-Global-Hi* trigger, which triggered on integrated p_T deposition over an entire quadrant, was originally to have been used for this analysis. However, it was discovered after data were taken that this trigger had hardware problems, rendering the data it produced unreliable.

set	from run	to run	beam	target	events
A	2852	3036	negative	Cu+Be	786,171
C	2588	2670	positive	Cu+Be	1,224,950
D	2062	2382	negative	Be	1,242,178
E	1728	2007	positive	Be	1,508,174

Table 8 – Data sample from the E706 '87-'88 run which has been considered in this analysis. This represents about 350 tapes of data.

highest p_T	output stream
$< 3 \text{ GeV}/c$	rejected
$\geq 3 \text{ GeV}/c$	"PT3" stream
$\geq 4 \text{ GeV}/c$	"PT4" stream
$\geq 5 \text{ GeV}/c$	"PT5" stream

Table 9 – High- p_T data streams. Events were categorized according to the highest p_T photon or di-photon.

pairs. Based on this number, events were split into the three streams shown in table 9. These data were stored in a simple, compact format, referred to as the "mini-DST" format. Each of these streams consisted of several 9-track tapes.

This analysis used the data from the PT3 stream for data set A and data from the PT4 stream for data sets C through E. The reason for the change was that the *Single-Local* trigger threshold was lowered between run 2904 and 2905 (partway through set A), thus events in the other sets did not have meaningful data below a p_T of 4 GeV/c .

Offline, a detailed study was done to eliminate unreliable data. In addition to consulting the experimental log, the data themselves were checked for indications of problems. For example, a run in which an anomalously large percentage of events were of a single trigger type would not be considered usable. Based

on this study, some runs ($\approx 5\%$) were entirely rejected. Table 10 shows the total number of events, from the appropriate streams, which were available for analysis after these rejections. This study also identified cases in which one or more of the EMLAC octants was not functioning properly. In these cases, the runs were retained, but data were only used if they came from the functioning parts of the detector.

Data Set	A	C	D	E
Number of events	321,861	207,784	168,976	111,971

Table 10 – Data sample available for direct photon analysis.

7.2 MUON BREMSSTRAHLUNG

By far the major source of background to the direct photon signal in E706 was *muon bremsstrahlung*. In-flight decays of beam particles resulted in a large number of muons travelling more-or-less parallel to the beam, but often several feet away from it. When these muons interacted with the calorimeter, they would often produce a photon through bremsstrahlung. Because this photon was at a large radius, it would mimic a high- p_T event in the trigger and in preliminary offline analysis. Eliminating these events from the data was the primary task during analysis.

Recall that an attempt to eliminate the muons was made during the running period. During data taking, an event did not trigger if there was a signal in both of the veto wall planes (see section 5.2) within a period from ≈ 35 ns before to 100 ns after the interaction^[39].

Time of Arrival

Offline, a detailed study was done of the time profiles which were recorded for each of the veto wall counters in each event. The counters were found to be less efficient than was believed. Also, it was found that the trigger was sensitive

to muons occurring more than 35 ns before the interaction, and hence such events were not vetoed by the trigger logic. Evidence of these “out-of-time” events can also be seen by studying photon times, as recorded by the EMLAC TVCs. This is dramatically illustrated in figure 34, which shows a time profile of the highest p_T object in each event*. In 34a, objects were rejected if there was a signal in either veto wall plane, in the quadrant corresponding to the trigger octant, within ± 140 ns of the interaction (this is the extent of the time profile which was recorded for the veto wall counters). In contrast, figure 34b shows the time distribution where there was such a signal. Notice the relative sizes of the two peaks. Clearly, muons were responsible for a large number of experimental triggers. The large peak before the interaction time represents the muons that arrived more than 40 ns before the event. The more gradual peak after represents the inefficiency of the veto wall when used in an AND configuration. It is interesting to note that the bucket structure of the beam is clearly visible in 34b.

Directionality

Another signature of muon bremsstrahlung was the fact that the photon produced did not originate from the target, but rather travelled parallel to the beam. To flag this, a directionality δ was defined as

$$\delta = r_{front} - Z_{front}^{LAC} / Z_{back}^{LAC} \times r_{back} \quad (7.1)$$

where r_{front} was the reconstructed r position of the shower in the front section of the EMLAC, r_{back} was the r position of the shower in the back section of the EMLAC, and Z_{front}^{LAC} and Z_{back}^{LAC} were the respective distances from the target to the upstream faces of the front and back sections of the EMLAC. Figure 35 illustrates the concept. For objects which originated in the target, the directionality would have been close to zero. For objects which came parallel to the

* Notice there is a slight positive shift in the time corresponding to an interaction. This is due to the low statistics which were available when the absolute time scale was originally calculated. This effect has been taken into account in the cuts which have since been imposed on this variable.

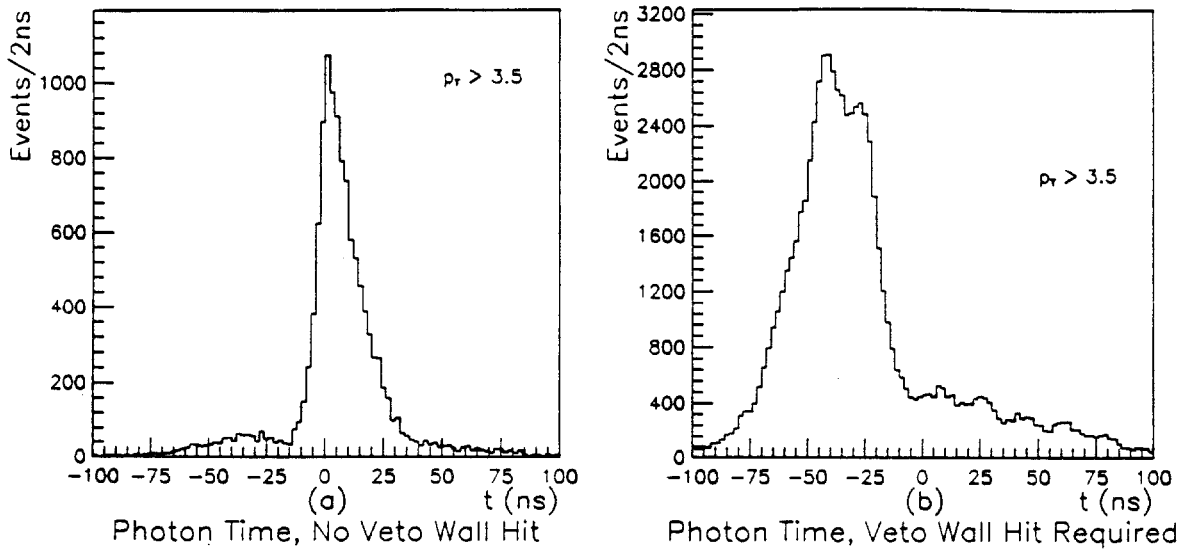


Figure 34 – TVC distributions for non- μ (a) and μ (b) events.

beam, the directionality would have a positive value. Figure 36 is a scatter plot of directionality vs. p_T for reconstructed photons. No veto wall requirements have been imposed for this distribution. For high- p_T objects, there is a clear enhancement in the positive directionality region, which dominates in the high- p_T region. The relationship between the directionality and the muon-induced events is shown in figure 37, which plots photon directionality against the time. Again, no veto wall requirements have been imposed. In most cases, the objects with high directionality were also out of time with the interaction. This figure also shows the experimental cuts which have since been placed on these values.

Longitudinal Profile

Because the radiation length for muons is much longer than the longitudinal thickness of the electromagnetic calorimeter, muons would emit bremsstrahlung photons with a flat distribution in depth. This would result in bremsstrahlung events having an anomalous amount of energy in the back section of the calorime-

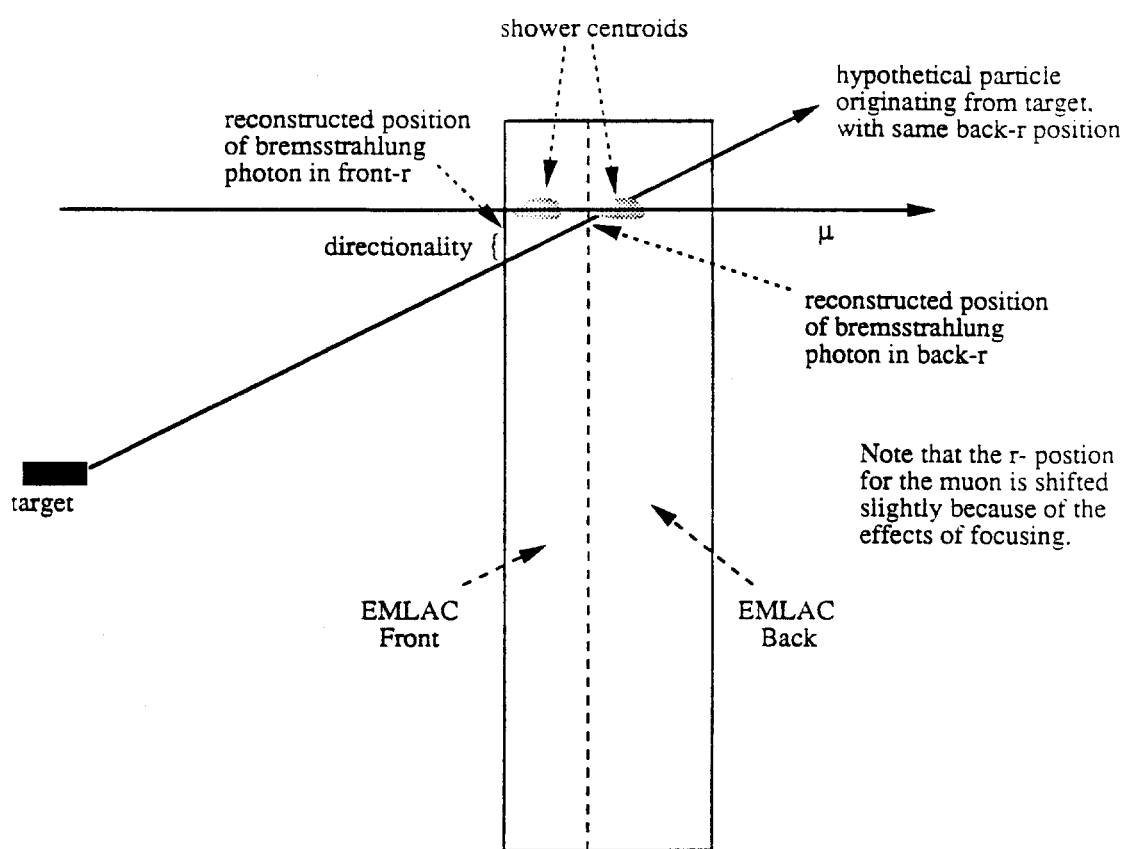


Figure 35 – Concept of photon “directionality”. The relative r positions of showers in the front and back of the EMLAC are used to flag muon bremsstrahlung.

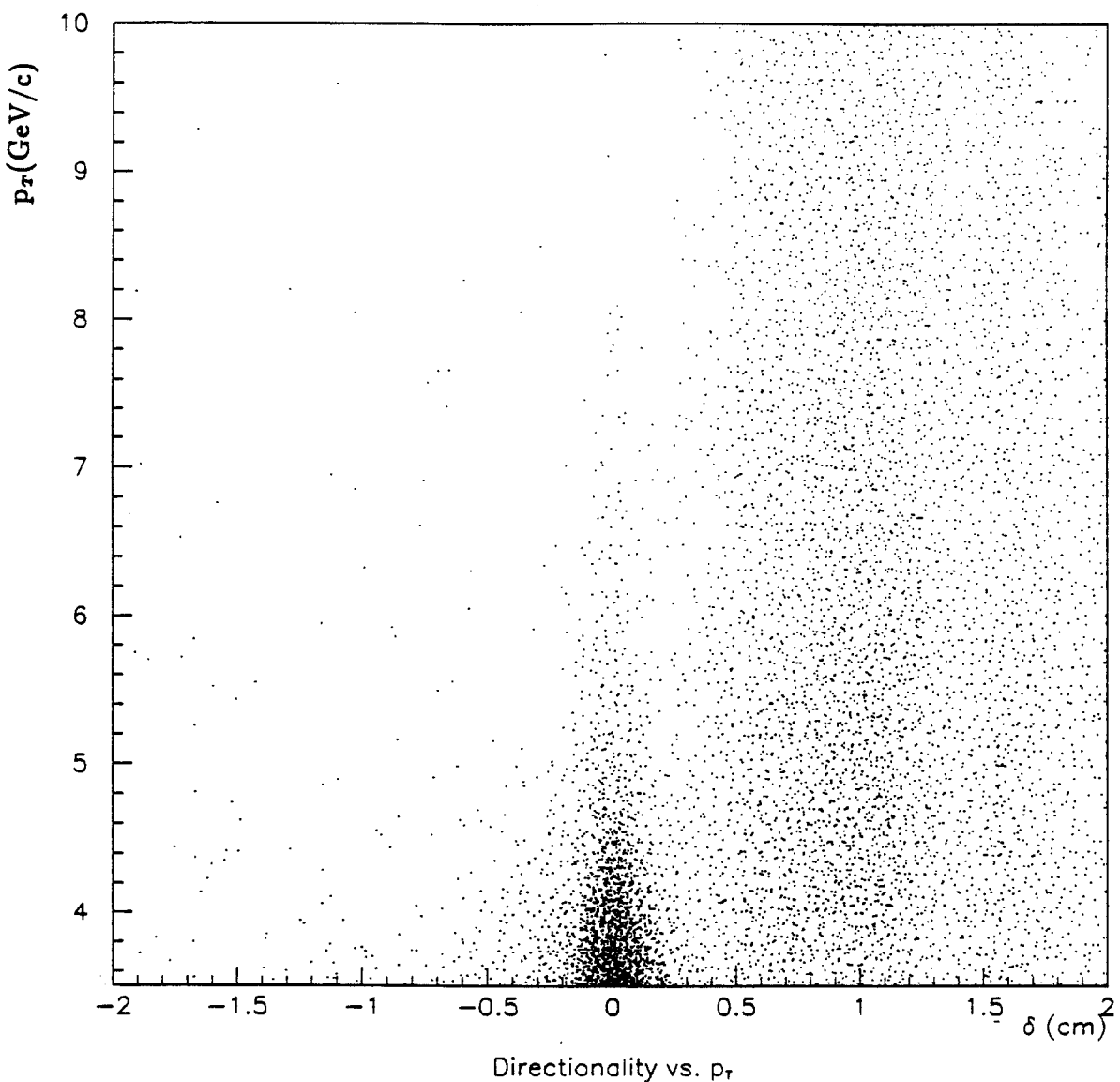


Figure 36 – Photon directionality vs. p_T . No cuts have been applied to this plot. The muon bremsstrahlung events are clearly visible in the band with directionality greater than .4 cm.

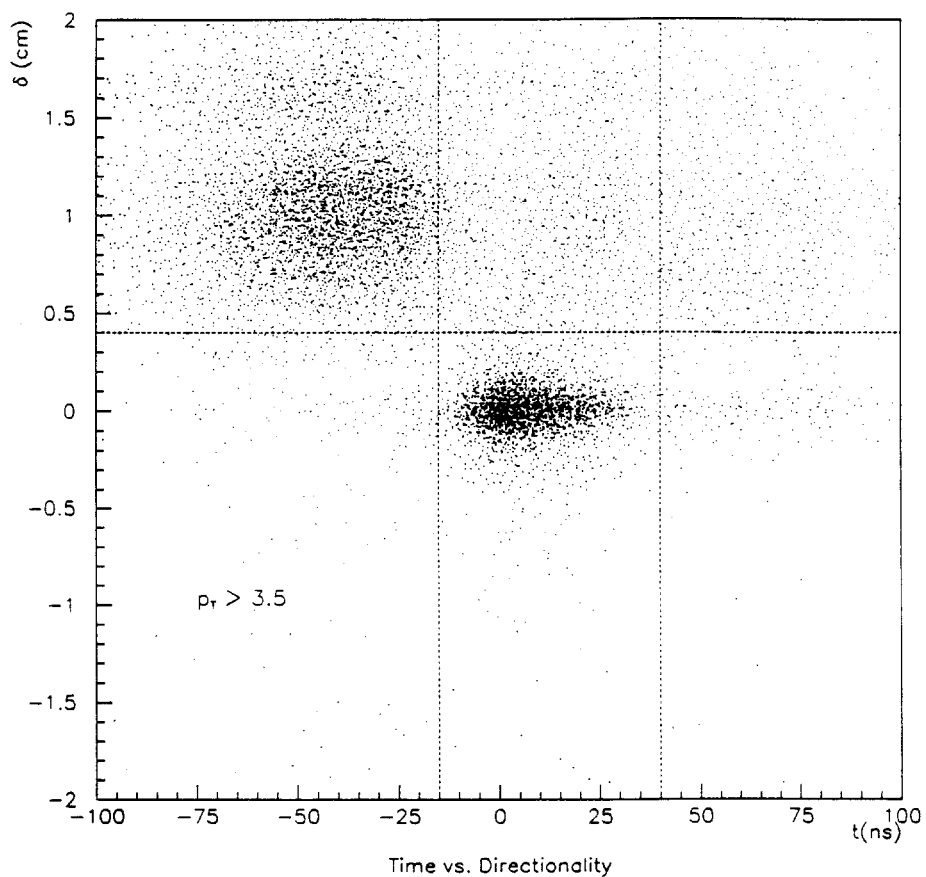


Figure 37 – Photon directionality vs. TVC time. The lines indicate the experimental cuts which have been placed on these variables.

ter. In fact, because the back section of the calorimeter was twice as thick as the front section, a large number of bremsstrahlung events would have no energy in the front section.

Summary of Muon Cuts

The list below summarizes the cuts which were done primarily to eliminate muon bremsstrahlung. Note that in some cases the whole event was rejected, while in others only the offending object was rejected.

- Events were rejected in which there was a signal in either of the veto

wall planes, in the quadrant* corresponding to an EMLAC trigger octant, within 140 ns of the trigger time.

- Events were rejected in which the vertex finding routine was unable to reconstruct a vertex within the target volume. This was to reject events where a muon came in coincidence with a false interaction signal caused by noise in the scintillation counters.
- Objects were rejected which had a directionality greater than .4 cm.
- Objects were rejected in which the energy reconstructed in the front of the EMLAC was less than 20% of the total reconstructed energy[†]. This " E_{front}/E_{total} " cut also rejected showers caused by hadrons.
- Objects were rejected which had a time, as recorded by the TVCs, more than 15 ns before or 40 ns after the nominal zero time.
- Objects were rejected in which a charged track, projected to the face of the EMLAC, fell within 1 cm of the shower. This "close track" cut also eliminated electrons and other charged tracks from the interaction.

Figure 38 again shows the p_T versus the directionality. In this case, the other muon rejection cuts have been imposed. We see that now there are far fewer events in the positive directionality region.

7.3 QUALITY AND FIDUCIAL CUTS

In addition to the cuts to eliminate muon bremsstrahlung, certain cuts were imposed to insure the quality of the data. First, events were checked to see if any of the EMLAC quadrants had an anomalously large amount of energy in any one view which had not been correlated with any other view(s) to form photons. This *uncorrelated energy* was an indication that the reconstruction code did not

* The veto wall planes were arranged in quadrants, such that each quadrant detected muons striking a particular EMLAC quadrant.

† Note that requiring energy in the front of the calorimeter also insured that the photon directionality could be calculated.

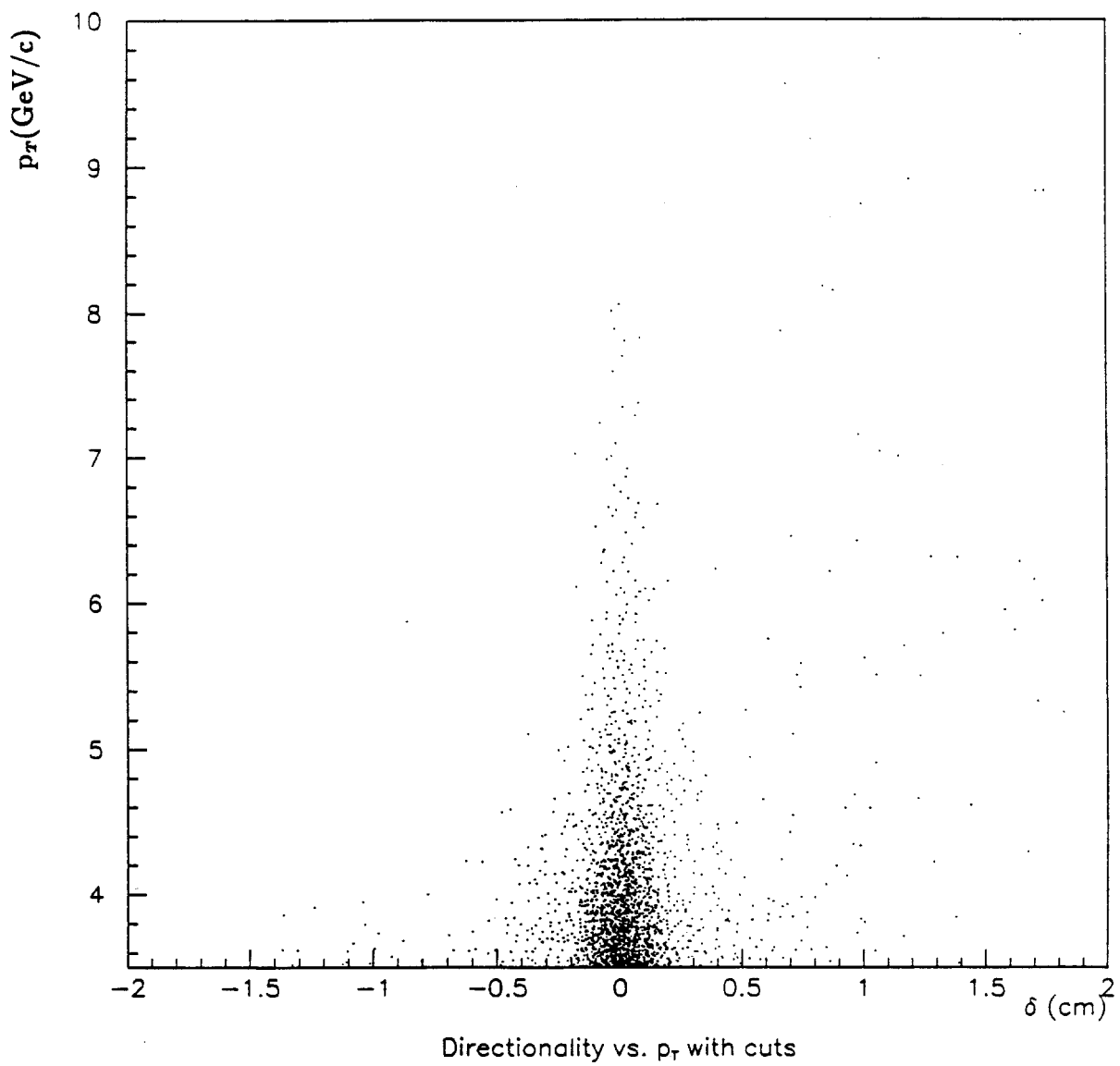


Figure 38 – Photon directionality vs. p_T . In this case, all direct photon cuts beside directionality have been applied.

work properly. If any active quadrant had more than 10 GeV of uncorrelated energy, the event was rejected. Also, fiducial cuts were made to eliminate objects which fell close enough to detector boundaries to make proper reconstruction impossible. To this end, objects were rejected if the reconstructed r position did not fall within the region $24 \text{ cm} < r < 138 \text{ cm}$ or if the ϕ position was within 3 cm of a quadrant boundary[†].

7.4 $\gamma\gamma$ MASS SPECTRUM

The derivation of the π^0 cross-section will be discussed later in this chapter, but because the π^0 signal is also important to the understanding of the direct photon analysis, the subject is introduced here.

Figure 39 shows the two photon mass distribution for photons in the data set used in this analysis. Not all of the photon cuts were applied for this plot. Specifically, the directionality, timing, close track, and $E_{\text{front}}/E_{\text{total}}$ cuts were not applied.

Pairs were only formed from photons falling within the same octant, and that octant was required to have satisfied the *Single-Local* trigger. Additionally, the vector sum p_T of the pair was required to be greater than 3.5 GeV/c. Finally, the rapidity (y) of the pair was required to be in the range $-.7 < y < .7$. This corresponds to the sensitive region of the electromagnetic calorimeter.

Note that a large mass peak corresponding to the decay $\pi^0 \rightarrow \gamma\gamma$ is clearly seen, as is the peak from the decay $\eta \rightarrow \gamma\gamma$. For the purposes of this analysis, pairs in the region $110 < M_{\gamma\gamma} < 160$ MeV were designated π^0 's. For statistical background subtraction, pairs in the regions $75 < M_{\gamma\gamma} < 100$ MeV and $170 < M_{\gamma\gamma} < 195$ MeV were designated π^0 "sideband" pairs. To correct a given distribution for background effects, the variable of interest was plotted both in the mass region and in the sideband region. The latter distribution would then be subtracted to yield the distribution due strictly to π^0 's. This was valid to the

[†] The term "quadrant boundary" here refers to the ideal quadrant boundaries corresponding to ϕ angles which are integer multiples of $\pi/2$.

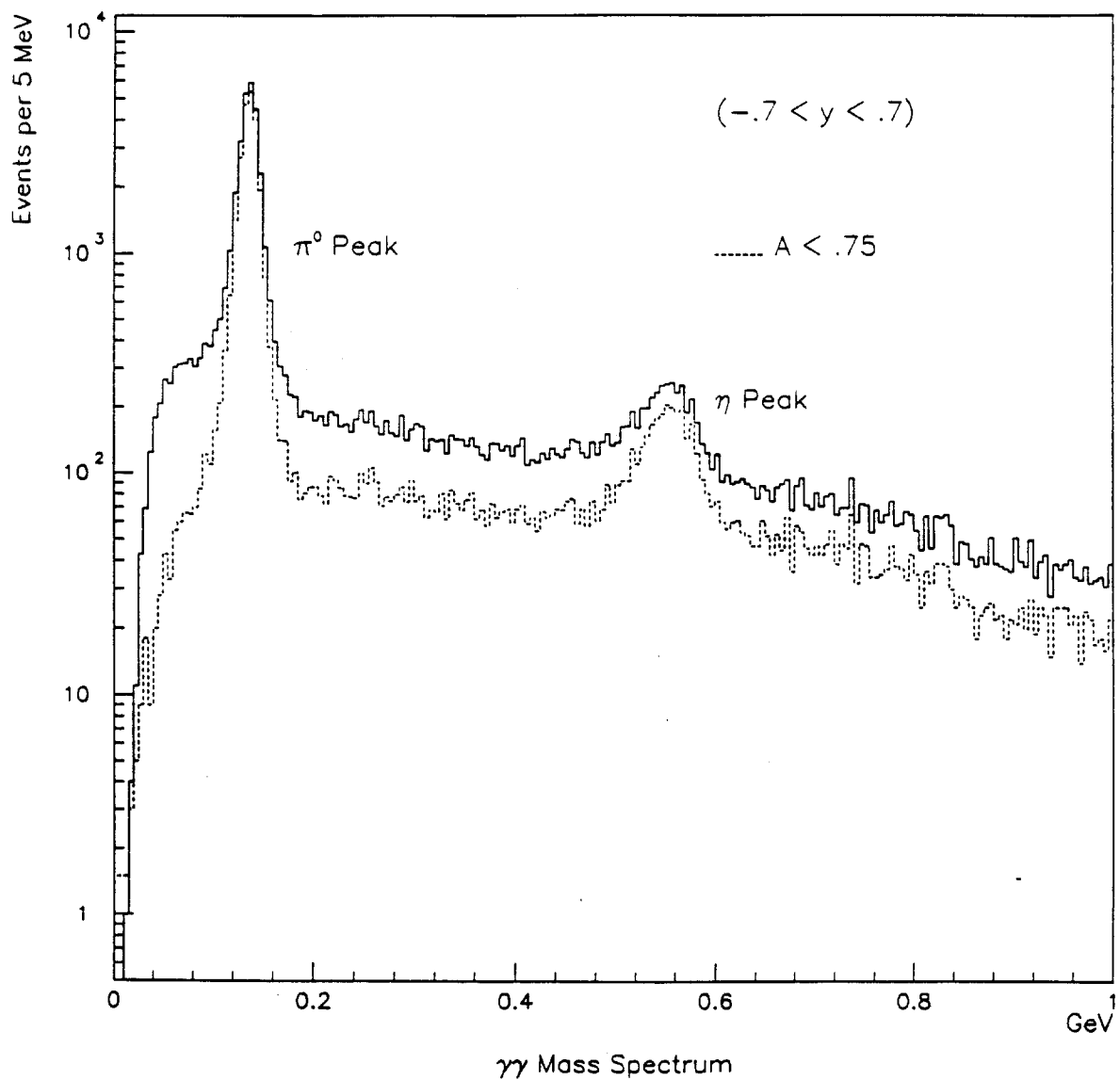


Figure 39 – Two photon mass spectrum for all photon pairs falling within triggering octants. Entire data sample is represented.

extent that any background effects had a linear dependence on the mass. Similarly, the η mass range was taken to be $450 < M_{\gamma\gamma} < 650$ MeV, with sideband ranges $340 < M_{\gamma\gamma} < 440$ MeV and $660 < M_{\gamma\gamma} < 760$ MeV.

Because the π^0 is a scalar particle, it decays with a flat distribution for $|\cos(\theta^*)|$, where θ^* is the angle between one of the decay photons and the π^0 direction, in the center-of-mass frame. In the lab frame, this distribution is approximately equal to the asymmetry A , defined by

$$A = \frac{|E_1 - E_2|}{(E_1 + E_2)} \quad (7.2)$$

where E_1 and E_2 are the energies of the decay photons. In general, detectors are less efficient for highly asymmetric decays, because one photon is produced with a very low energy and at a large angle relative to the π^0 direction. The dashed line in figure 39 shows the $\gamma\gamma$ mass distribution with the asymmetry required to be less than .75. This asymmetry cut has been applied to all π^0 measurements used in this analysis. The rationale for this particular value will be given somewhat later in the chapter.

The position of the π^0 mass peak was used during the early stages of the analysis to establish the absolute energy scale of the EMLAC, octant by octant^[40]. This resulted in corrections to the original reconstructed energies, which have been applied to all data used here.

7.5 EVENT SIMULATION

Correction for experimental efficiencies and background is very important to the analysis. Very often this involves computer simulation of the detector, wherein one attempts to model the detector response to some specific physical event. This technique, commonly called “Monte Carlo”, is a powerful tool for understanding experimental hardware and software, and in practice often requires as much or more effort as the analysis of the actual data.

Event simulation for this analysis utilized the GEANT^[41] Monte Carlo package, developed at CERN. This package allows for the complete software simulation of the E706 spectrometer. Initial event topologies may be generated in a variety of ways. Each particle is tracked through the spectrometer and allowed to interact. Each of the resulting daughter particles is then tracked in the same way. This process continues until the energies of all of the resulting particles have fallen below some user-defined value. In this way, the energy deposition in every sensitive region of the spectrometer may be calculated. This method of fully developing events within the spectrometer is referred to as the "full shower" method. Clearly, it is the most accurate way available to model detector response; however, it requires a great deal of computer time to fully develop each event. In fact, to fully model a typical high- p_T event in the E706 spectrometer takes on the order of 5 hours on a VAX 11/780TM computer^[42]. For this reason the GEANT program allows the response of the various parts of the detector to be parametrized, thus greatly reducing the amount of computer time involved. In general, full simulations were studied to develop these parametrizations, which were then used for studies in which high statistics were required.

7.6 EFFECT OF CUTS

Table 11 shows the effect that the event rejections had on the data. The total number of events remaining after each subsequent cut is shown. Of the remaining events, table 12 shows the total number of photons, and the effect of each of the object cuts.

For each of these cuts, some number of actual photons were also rejected. These losses had to be calculated in order to correct the final cross-section measurement.

For several of the cuts, the number of "good" photons lost could be measured by their effect on the π^0 peak in the $\gamma\gamma$ mass spectrum. By subtracting the number of $\gamma\gamma$ pairs falling in the π^0 sideband range from the number falling in

Set	A	C	D	E
Total	321,861	207,784	168,976	111,971
Veto Wall Cut	193,146	48,751	60,225	29,451
Vertex Cut	150,865	38,996	48,523	19,972
Unc. Energy Cut	142,111	36,778	45,257	18,364

Table 11 – Number of events surviving each successive event cut.

Set	A	C	D	E
Total	1,144,864	309,726	400,222	165,960
$p_T > 3 \text{ GeV}/c$	41,579	25,388	30,328	12,687
Fiducial Cut	34,036	20,644	24,275	10,286
Directionality Cut	33,337	20,038	23,783	9,999
Track Cut	29,765	18,397	21,786	9,196
E_{front}/E_{tot} Cut	28,839	17,726	21,229	8,880
TVC Cut	28,071	17,138	20,530	8,559

Table 12 – Number of photons surviving each successive photon cut.

the mass range, one could measure the number of π^0 's in a given sample of the data. Measuring this number before and after some particular cut provided a measure of the number of good photons rejected by the cut. This method was used to calculate the effect of the following cuts:

- veto wall cut
- uncorrelated energy cut
- close track cut

Note that because the last cut acted on individual photons, its effect on the direct photon signal was taken to be half of the effect on the π^0 signal.

This method was ruled out in the case of the directionality cut and the

E_{front}/E_{total} cut. This was because the individual photon showers often coalesced in the back section of the electromagnetic calorimeter, biasing the sample. The effect of the directionality cut was determined by assuming the directionality distribution was symmetric about zero cm and measuring the number of single photons with directionality less than - .4 cm. The effect of the E_{front}/E_{total} cut was determined from a study of fully simulated electromagnetic showers.

The effect of the timing cut was determined by generating the time distribution of photons which formed a π^0 mass and subtracting the time distribution for photons which formed a mass in one of the π^0 sidebands. The resulting distribution was then used to determine the tails of the time distribution and calculate losses.

Table 13 shows the correction which must be applied to the observed number of single photons to correct for good photons rejected by each of the cuts. Corrections for veto wall were calculated separately for negative and positive beam. This is because the muon content was expected to be different in the two cases. However, because most of the events rejected by the veto wall cut are believed to be due to noise in the veto wall counters, the corrections are quite similar.

The efficiency of the vertex detection algorithm was determined as a function of vertex position based on a visual scan of events. It was found to vary linearly from $90.8 \pm 2.0\%$ at the upstream end of the copper target to $96.3 \pm 1.3\%$ at the downstream end of the beryllium target.

7.7 TRIGGER EFFICIENCY

For each event, the state of the trigger logic (see section 5.4) was recorded by the NEU PDP-11; thus, at analysis time it was known which trigger or triggers were satisfied for that event.

To evaluate the performance of the *Single-Local* trigger, a sample of events were used which had satisfied the *Two-Gamma* trigger. Recall that this trigger

Cut	Correction	
	negative beam	positive beam
Veto Wall	$1.111 \pm .003$	$1.099 \pm .006$
Uncorrelated Energy		$1.043 \pm .002$
Close Track		$1.006 \pm .001$
Timing		$1.034 \pm .004$
Directionality		$1.005 \pm .001$
E_{front}/E_{total}		$1.015 \pm .001$
C_{cuts}^{γ} (total correction)	$1.230 \pm .007$	$1.216 \pm .009$

Table 13 – Corrections applied to observed single photons to compensate for losses due to cuts.

required a minimum amount of localized p_T in two opposing EMLAC octants. p_T was summed in the same way for the *Two-Gamma* trigger as for the *Single-Local* trigger, but with a lower threshold. Therefore, for an octant in which the *Two-Gamma* threshold was satisfied, the fraction of events in which the *Single-Local* trigger was also satisfied could be used to calculate the behavior of the *Single-Local* trigger as a function of p_T .

For each of the *Two-Gamma* events, reconstructed photon momenta were used to calculate p_T depositions in each of the triggering octants. The p_T was summed for overlapping groups of 16 r strips to emulate the summing of the online trigger electronics. The ratio

$$\frac{\text{SingleLocal} \bullet \text{TwoGamma}}{\text{TwoGamma}}$$

was studied as a function of highest summed p_T of these groups to determine the efficiency of the *Single-Local* trigger for that octant. Figure 40 shows an example of such a turn-on curve for a typical octant.

It was discovered that image charge effects (see discussion, section 5.2) caused the *Single-Local* trigger to have different behavior in different r regions,

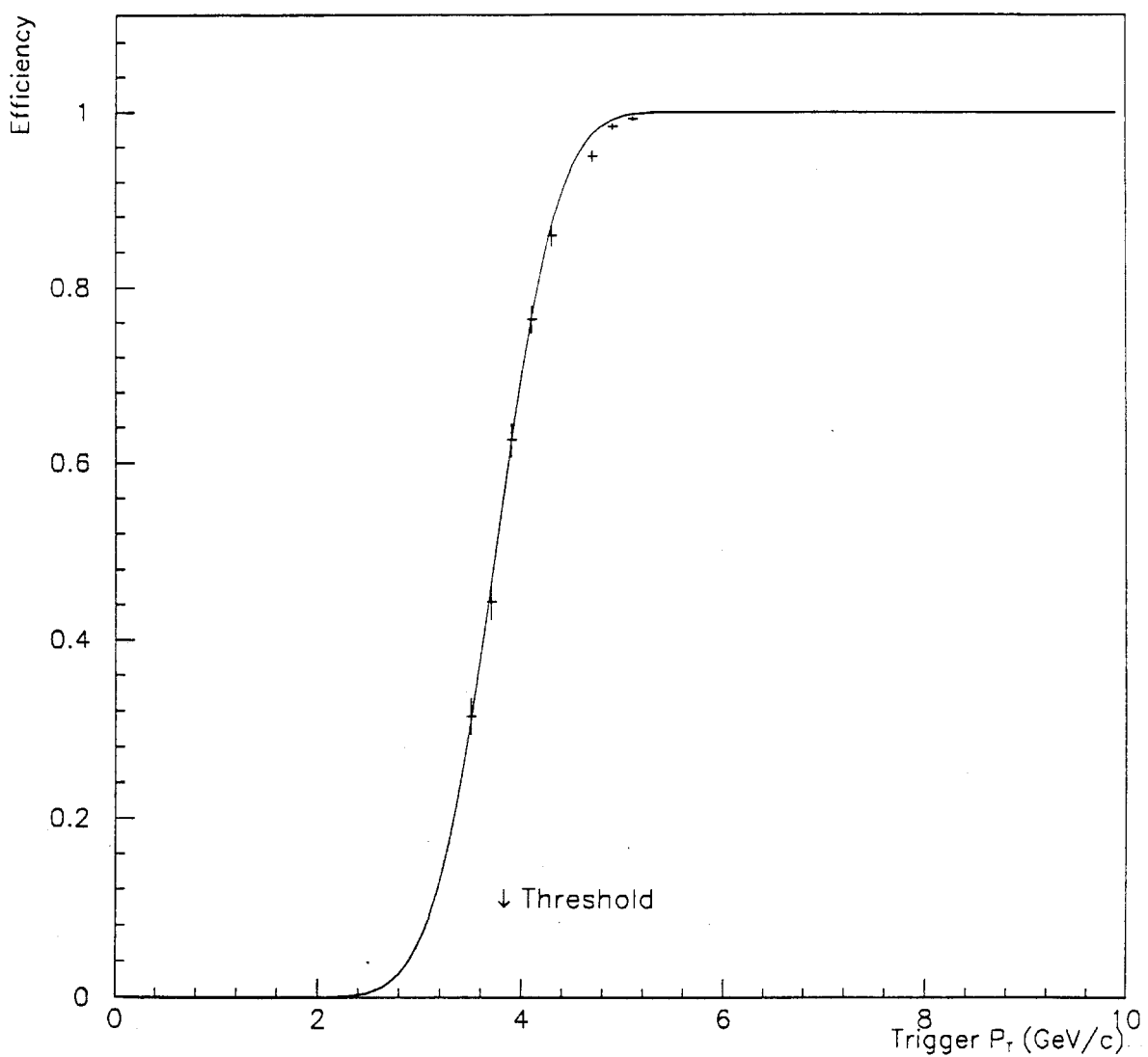


Figure 40 – Single-Local trigger turn-on curve for a typical octant.

so ultimately trigger efficiency was evaluated for three separate r regions in each octant. The first contained the inner 32 r strips; the second contained the next 64; and the third contained the next 128. The resulting set of trigger efficiencies was used in the subsequent analysis. Each region was also assigned a minimum p_T threshold, below which the trigger was not considered reliable. This typically corresponded to p_T ranges where the efficiency of the trigger was below about 80%. Occasionally, this study discovered anomalies within a particular r region of a particular octant. In this case, the region was considered unreliable at all values of p_T .

On an event-by-event basis during the analysis, trigger efficiencies were calculated for each octant which satisfied the *Single-Local* trigger by calculating octant p_T sums, in the manner described above, and then using these to find the proper position on the efficiency curve for the r region appropriate to the particle being considered.

7.8 SINGLE PHOTON CROSS-SECTION

Candidate Selection

In addition to the aforementioned quality and muon rejection cuts, single photon candidates were rejected if they combined with any other photon in the electromagnetic calorimeter, with an asymmetry less than .75, to form a mass in either the π^0 or the η mass range. To statistically correct for losses due to accidental combinations, photons were counted twice if they formed a mass, again with asymmetry less than .75, in the π^0 or the η sideband regions.

All direct photon candidates were required to have a rapidity in the range $-.7 < y < .7$. Again, this corresponded to the sensitive region of the electromagnetic calorimeter.

Direct photon candidates were required to fall within an octant which had satisfied the *Single-Local* trigger. Also, each was required to be above the minimum p_T for the r region on which it fell (see discussion in section 7 of this chapter).

Figure 41 is an illustration of an event containing a direct photon candidate. The lines represent the projections of particle momenta onto the X-Y plane, thus the length of each line represents the relative magnitude of the p_T of that particle. The dashed line represents the direct photon candidate and the solid lines represent the charged tracks in the event. Other electromagnetic objects in the event are represented by dashed lines too short to be visible on the plot. We see that the event shows the expected jet structure balancing the p_T of the photon.

Cross-section Calculation

In general, the invariant differential cross-section per nucleon can be expressed as a function of p_T and rapidity (y) by

$$E \frac{d\sigma}{d^3p}(p_T, y) = \frac{1}{N_{scat} \times B} \frac{dN(p_T, y)}{2\pi p_T dp_T dy} \quad (7.3)$$

where $dN/dp_T dy$ is the differential event distribution, B is the number of incident beam particles, and N_{scat} is the number of target nucleons per cross-sectional area of the beam. The latter is equal to $\rho L N_0$, where ρ and L were the density and length of the target, respectively, and N_0 is Avogadro's number (expressed in nucleons/g). This definition of the cross-section is conceptually quite simple; in practice, however, extracting it from the data is a multi-step process requiring corrections at each step.

A weighted photon count (N_w) is defined within a given p_T band (p_T^{lo} to p_T^{hi}) as

$$N_w(p_T) \Big|_{p_T=p_T^{lo}}^{p_T^{hi}} = \frac{1}{\Delta p_T} \sum_{i=1}^{N_{raw}} \frac{1}{p_{Ti} \times \eta_{det}(p_{Ti}, r_i, z_i)} \quad (7.4)$$

The sum is over single photons surviving all cuts and falling within the specified p_T band. The width of the p_T band (Δp_T) is an approximation to the dp_T term in (7.3). Each photon is assigned a detection efficiency (η_{det}) based on its p_T , radius (r), and vertex position (z). The photon is weighted by the inverse of

this value to correct for similar photons which were not detected. This overall efficiency has several contributions and is broken down as

$$\eta_{det} = \frac{\eta_{acc} \times \eta_{trig} \times \eta_{vx} \times P_{NC}^{\gamma}}{C_{oct}} \quad (7.5)$$

where the individual elements are

- $\eta_{acc}(r)$ – the probability that the photon fell within the EMLAC fiducial volume. At a given radius this is just the fraction of a circle around the beamline which is within the fiducial volume.
- $\eta_{trig}(r)$ – the efficiency of the *Single-Local* trigger for the appropriate r region of the octant.
- $\eta_{vx}(z)$ – the efficiency of the vertex finding program.
- $C_{oct}(p_T, r)$ – the correction for malfunctioning EMLAC octants. This is given by

$$C_{oct}(p_T, r) = \frac{8}{N_{live}(p_T, r)} \quad (7.6)$$

where N_{live} is the number of octants which were reliable at the given r and p_T at the time the event occurred.

- $P_{NC}^{\gamma}(z)$ – the probability that the photon did not pair convert between the vertex and the second PWC station*.

The beam count which is used for normalization is given by

$$B(p_T) = N_{LTB}(p_T) \times P_{NA} \quad (7.7)$$

where N_{LTB} is the “live triggerable beam”, or number of incident beam particles which arrived during times in which the detector was able to be triggered, as calculated from the experimental scalers. Note that this is expressed as a function

* The electrons from conversions before the magnet would be swept away by the magnetic field. Conversions between the magnet and the first PWC station would appear as a single track and be rejected by the close track cut. Those happening after this point would appear as single photons.

	π^- Be	π^- Cu	pBe	pCu
$P_{NA}^{\pi^0}$.949	.986	.934	.981
(no Cu target)	.957	—	.943	—
$N_{scat} (\equiv \rho L N_0) (\text{cm}^{-2})$	4.45×10^{24}	$.862 \times 10^{24}$	4.45×10^{24}	$.862 \times 10^{24}$

Table 14 – Final reaction dependent corrections.

of p_T . For a given p_T region, this value was only integrated over runs for which that p_T was above the minimum p_T at which at least one octant was reasonably efficient. P_{NA} is the probability that a beam particle was not absorbed between the beam counters and the center of the target of interest. Table 14 shows this correction for each reaction type. This table also shows N_{scat} , as defined for (7.3), appropriate to each target.

Finally, the invariant cross-section, averaged over rapidity, is given by

$$\frac{1}{\Delta y} \int_{y=-.7}^{.7} E \frac{d\sigma}{d^3 p}(p_T, y) = \frac{C_{cuts}^\gamma}{N_{scat} \times B(p_T)} \frac{N_w(p_T)}{2\pi\Delta y} \times 10^{36} \quad (7.8)$$

The C_{cuts}^γ term is the correction for good photons rejected by the various quality and muon cuts (see table 13). The Δy ($= 1.4$) term reflects the fact that the cross-section has been averaged over the rapidity region studied by the experiment. The final factor of 10^{36} is to convert the result from cm^2/GeV^2 to picobarns/ GeV^2 .

Figure 42 shows the cross-section for $\pi^- + Be \rightarrow \gamma + \text{anything}$. At this point, no correction has been made for any sort of background. Before calculating background, the π^0 cross-section must be measured. This is described in the following section.

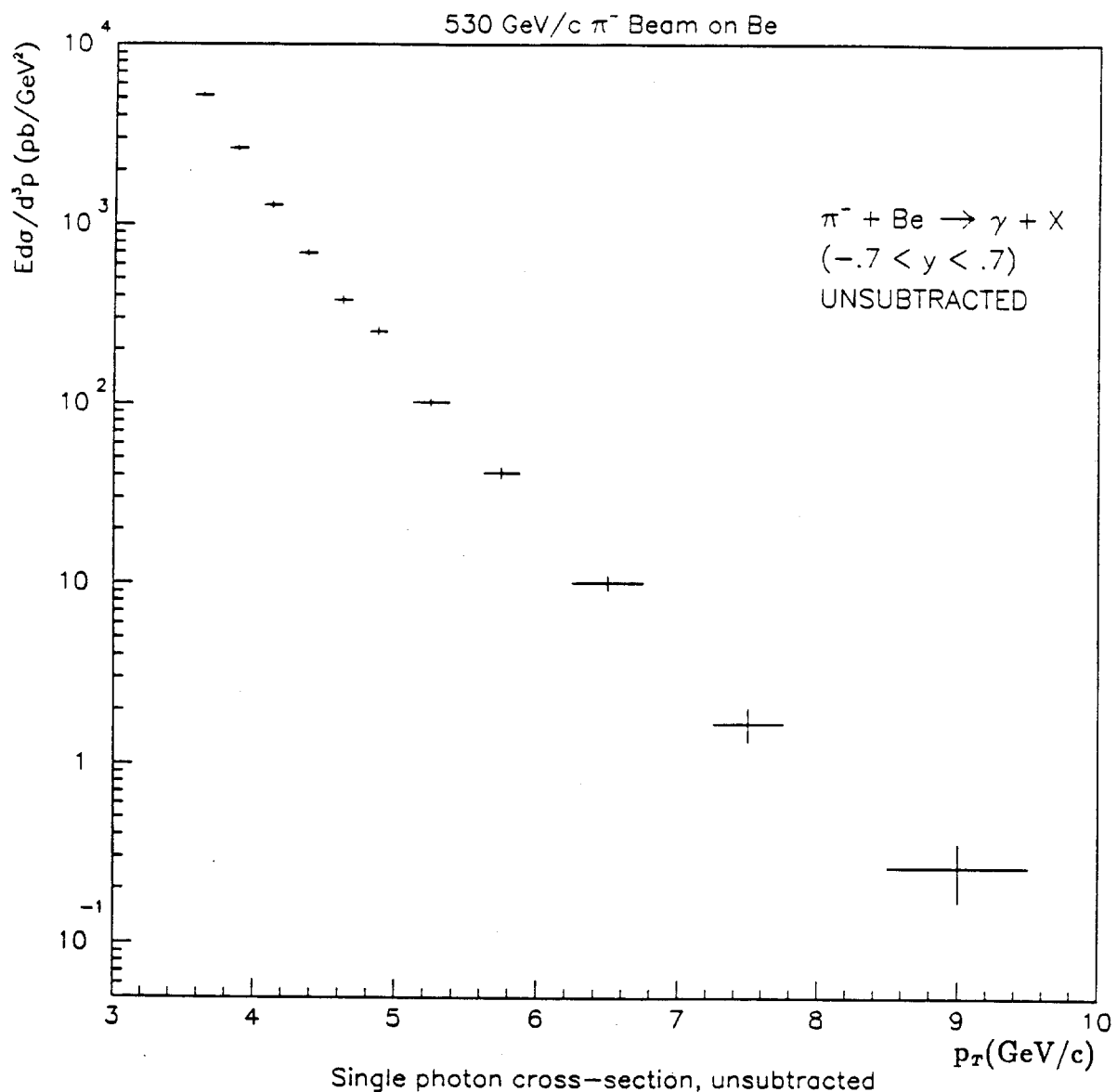


Figure 42 – Cross-section for single photons from π^- incident on beryllium. At this point no background subtraction has been done.

7.9 π^0 CROSS-SECTION

Candidate Selection

Because the muon bremsstrahlung events were not expected to artificially enhance the π^0 signal, the quality cuts imposed on π^0 candidates were somewhat less stringent than those for direct photons. Therefore, the directionality, timing, close track and E_{front}/E_{total} cuts were not applied during the π^0 analysis.

As with the single photon candidates, π^0 candidate pairs were required to fall within a single octant, which satisfied the *Single-Local* trigger. The vector sum p_T of the pair was required to be above the minimum allowable p_T of the appropriate r region of the octant.

Asymmetry

Figure 43 illustrates the asymmetry study for the π^0 candidate events. All events have been weighted by the inverse of the trigger efficiency. 43a and 43b are the distributions for the π^0 mass region and the sideband regions respectively. 43c is the sideband-subtracted distribution. We see that it is relatively flat out to about .75, while falling off rapidly at higher asymmetries. For this reason, π^0 candidates are required to have an asymmetry of $< .75$.

Geometrical Acceptance and Reconstruction Efficiency

Determination of the geometrical acceptance for single photons was a straightforward calculation, requiring no event simulation. For two photon decays, however, the situation was much more complicated, depending not only on the production parameters, but also on decay angles. Thus, direct calculation would have been hopelessly complicated. Also, for single photons, reconstruction efficiency was very close to unity. Because photons tend to be very close together in π^0 decays, π^0 reconstruction efficiency is often much lower.

In order to calculate π^0 geometrical acceptance, Monte Carlo π^0 events were generated with a grid of p_T and rapidity values of interest ($3.0 < p_T < 10.0$ GeV/c and $-.8 < y < .8$) and random azimuthal angles. These were then

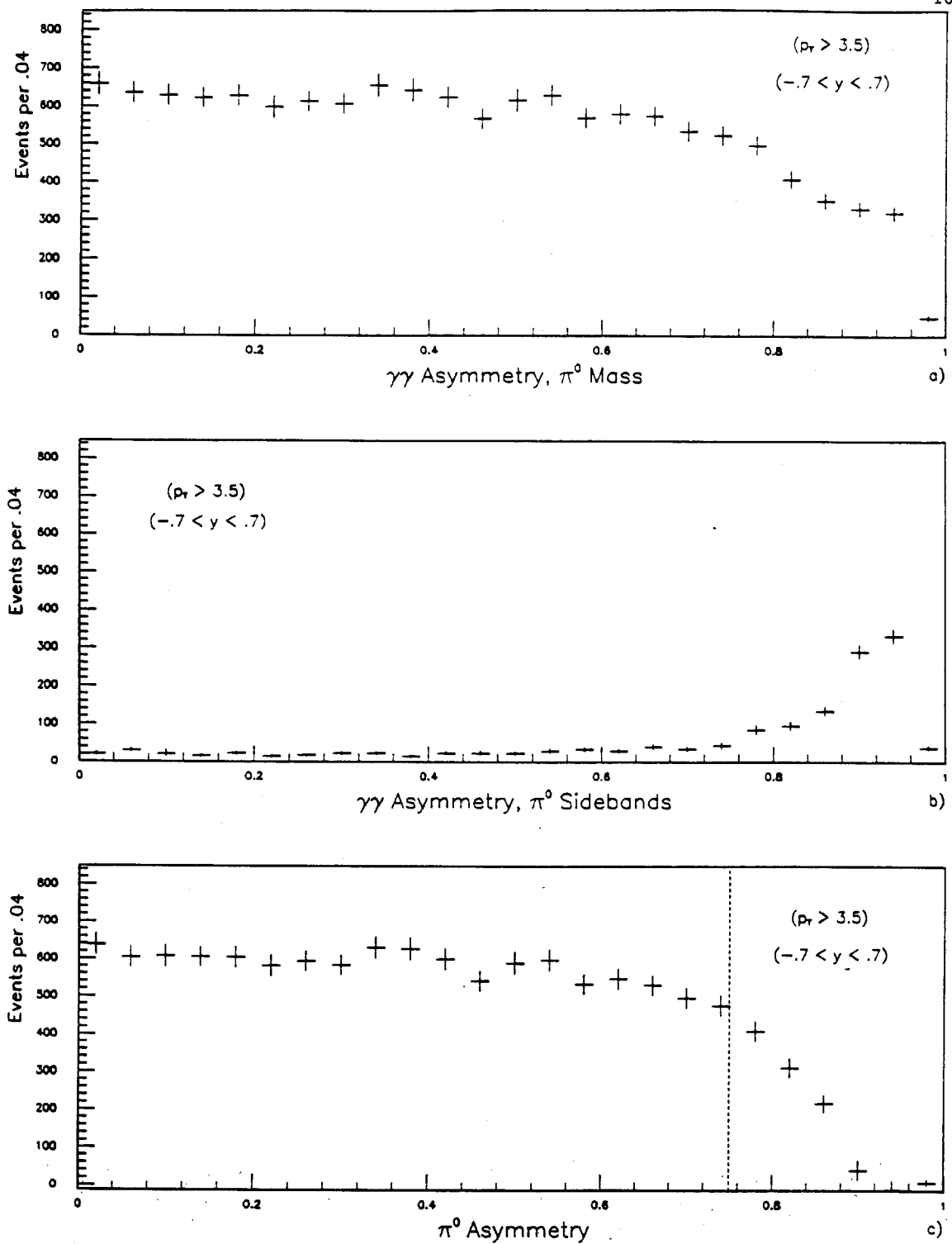


Figure 43 – π^0 asymmetry. Distributions are shown for the mass region (a) and the sideband region (b) separately. The dotted line on the subtracted plot (c) shows the present asymmetry cut.

allowed to decay to two photons with a flat asymmetry distribution in the range $0 < A < .75$. At each grid point, the fraction of events for which both γ 's fell within the fiducial volume of a single EMLAC octant was recorded. Of the events for which both photons fell within the fiducial volume, the parametrized response of the EMLAC was recorded and passed to the reconstruction algorithm. The fraction which were properly reconstructed was measured at each grid point. During the analysis, the arrays resulting from these studies were interpolated to find the geometrical acceptance and reconstruction efficiency for a given π^0 candidate pair.

Cross-section Calculation

The calculation of the π^0 cross-section is very similar to that of the single photon cross-section. In analogy to (7.4), a weighted count is defined within a given p_T band as

$$N_w(p_T) \Big|_{p_T=p_T^{lo}}^{p_T^{hi}} = \frac{1}{\Delta p_T} \sum_{i=1}^{N_{raw}} \frac{1}{p_{Ti} \times \eta_{det}(p_{Ti}, r_i, y_i, z_i)} \quad (7.9)$$

where the sum is over $\gamma\gamma$ pairs falling within the π^0 mass range with a vector sum p_T in the appropriate p_T interval. The detection efficiency is now broken down as

$$\eta_{det} = \frac{\eta_{acc} \times \eta_{trig} \times \eta_{vx} \times \eta_{rec} \times P_{NC}^{\pi^0}}{C_{oct}} \quad (7.10)$$

- $\eta_{acc}(p_T, y)$ – the geometrical acceptance
- $\eta_{trig}(r)$ – the efficiency of the *Single-Local* trigger for the appropriate r region of the octant.
- $\eta_{vx}(z)$ – the efficiency of the vertex finding program.
- $\eta_{rec}(p_T, y)$ – the reconstruction efficiency.
- $C_{oct}(p_T, r)$ – the correction for malfunctioning EMLAC octants. Same as for single photons.

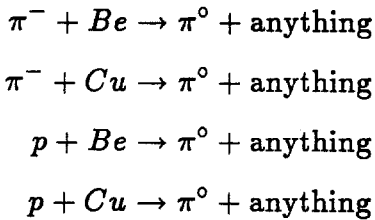
- $P_{NC}^{\pi^0}(z)$ – the probability that neither photon pair converted between the vertex and magnet*

The weighted sum is calculated in the same way for pairs falling in the π^0 sideband regions. The cross-section is then given (in analogy to (7.8)) by

$$\frac{1}{\Delta y} \int_{y=-.7}^{.7} E \frac{d\sigma}{d^3 p}(p_T, y) = \frac{C_{cuts}^{\pi}}{N_{scat} \times B(p_T)} \frac{(N_w(p_T) - N_w^{SB}(p_T))}{2\pi\Delta y} \times 10^{36} \quad (7.11)$$

The N_w^{SB} term is the weighted count for sideband pairs. The correction for cuts (C_{cuts}^{π}) now just contains the correction for the veto wall and uncorrelated energy cuts (found in table 13) multiplied by 4/3 to correct for the .75 asymmetry cut. The result is again in picobarns/GeV².

Figure 44 shows the π^0 inclusive invariant cross-sections per nucleon for the following reactions:



A detailed discussion of the E706 π^0 signal, including comparisons with theory and other experiments, can be found elsewhere^[43].

7.10 DIRECT PHOTON BACKGROUND

π^0 and η Decays

The calculation of direct photon background from π^0 and η decays was somewhat complicated. Because π^0 's (or η 's) at one p_T in general produce false direct photons at a lower p_T , it was necessary to assume some reasonable production spectrum. Also, because the analysis might be subtly affected by

* Because there was no tracking cut imposed on the π^0 sample, photons decaying after the magnet would not be rejected.

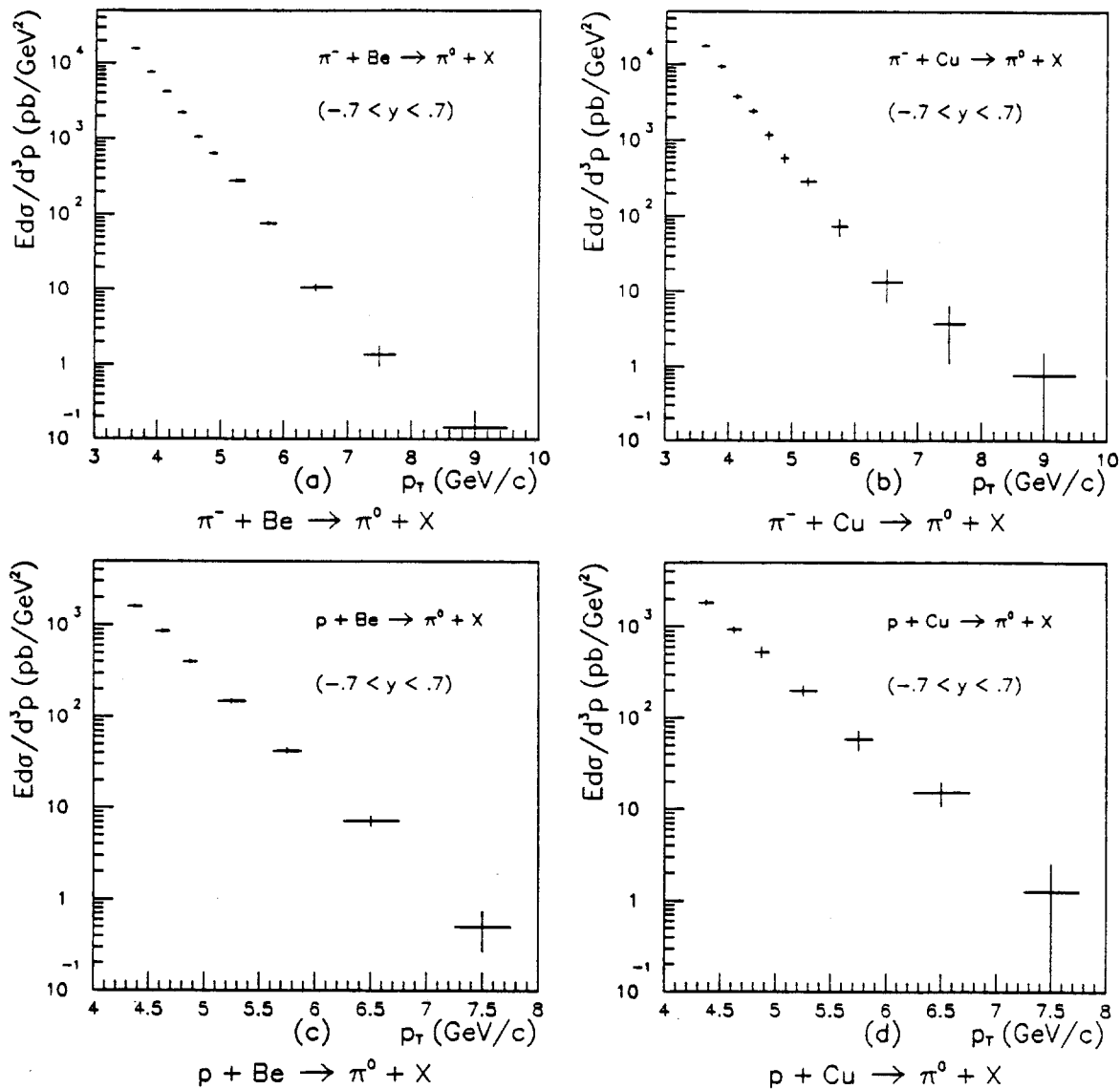


Figure 44 – π^0 invariant cross-section as measured in E706.

other showers within the detector, some reasonable assumption had to be made as to the event topology. It was decided to use the observed π^0 spectrum as a starting point, along with the associated topology. Events were selected with qualified high- p_T π^0 candidates, as described in the last section. The momentum vectors of all reconstructed electromagnetic objects were calculated. The two vectors corresponding to the π^0 decay were eliminated. They were replaced by the vectors resulting from the random isotropic decay of a π^0 with the same kinematic parameters as the observed π^0 . These artificial decay vectors were then randomly eliminated to simulate e^+e^- pair conversion in the target and upstream of the magnet. The set of remaining vectors was then given a random azimuthal rotation and stored, along with the vertex position and the detection efficiency (η_{det}) for the event. This procedure was repeated four times for each real π^0 event. Using GEANT, the parametrized response of the EMLAC to these events was recorded. Only the EMLAC was simulated, as only photons were used in the simulation and pair conversion was already considered.

The observed π^0 spectrum was also used to model η production. This was done because of the lower statistics on actual η production in the experiment. The η cross-section has been measured to be a constant fraction of the π^0 cross-section in this p_T range^[44], so this is a valid model for purposes of background calculation. The procedure followed was virtually identical to that followed for the π^0 's. In this case, however, when the π^0 decay photons were removed from original event, they were replaced with photons resulting from the isotropic decay of an η . The resulting events were weighted by the ratio of the η cross-section to the π^0 cross-section (.5), and by the branching ratio for $\eta \rightarrow \gamma\gamma$ (= .39). These weighted events were then added into the sample of simulated π^0 events.

From this point, the Monte Carlo data were reconstructed and analyzed with exactly the same procedures used for the real data, except that in all cross-section calculations, the trigger efficiency was replaced by the total detection efficiency of the original π^0 event. In this way the true π^0 (+ η) spectrum was simulated.

Because there were no real direct photons in this sample, any which were found by the direct photon analysis represented the background due to π^0 and η decays. In general, this false background was expressed as a fraction of the π^0 cross-section, measured from the same Monte Carlo sample.

A good measure of the performance of this Monte Carlo study is how well it reproduces the observed π^0 asymmetry spectrum. This distribution is sensitive both to geometric effects and to the detector response at low energies. Figure 45 shows a comparison of the observed π^0 asymmetry distribution with the asymmetry distribution predicted by this Monte Carlo procedure. Trigger corrections have been applied to the data plot. Detection efficiencies have been applied to both plots. Note that the agreement is quite good.

Figure 46 shows the inclusive invariant cross-section per nucleon for $\pi^- + Be \rightarrow \gamma + \text{anything}$ as a fraction of the cross-section for $\pi^- + Be \rightarrow \pi^0 + \text{anything}$. The dashed line represents the ratio one would expect from π^0 and η decays, as calculated with the method described above. It is important to notice that the predicted false background is more than half the measured signal in the low p_T region. Clearly the final result is very sensitive to one's estimate of this background.

To correct the direct photon cross-section for this background, the observed π^0 cross-section is multiplied by the predicted false γ/π ratio. The result is then subtracted from the observed single photon cross-section.

Residual Muon Background

Because muon induced events are more likely to have occurred out of time with the interaction, the time profile of events was studied to estimate the residual muon contamination. Figure 47 shows the time distribution, as measured by the TVCs, for photons which formed a π^0 mass with asymmetry less than .75, in the entire negative beam data sample. All single photon cuts have been applied to the sample (except timing of course). The distribution for photons forming pairs with masses in the π^0 sidebands, with asymmetry less than .75,

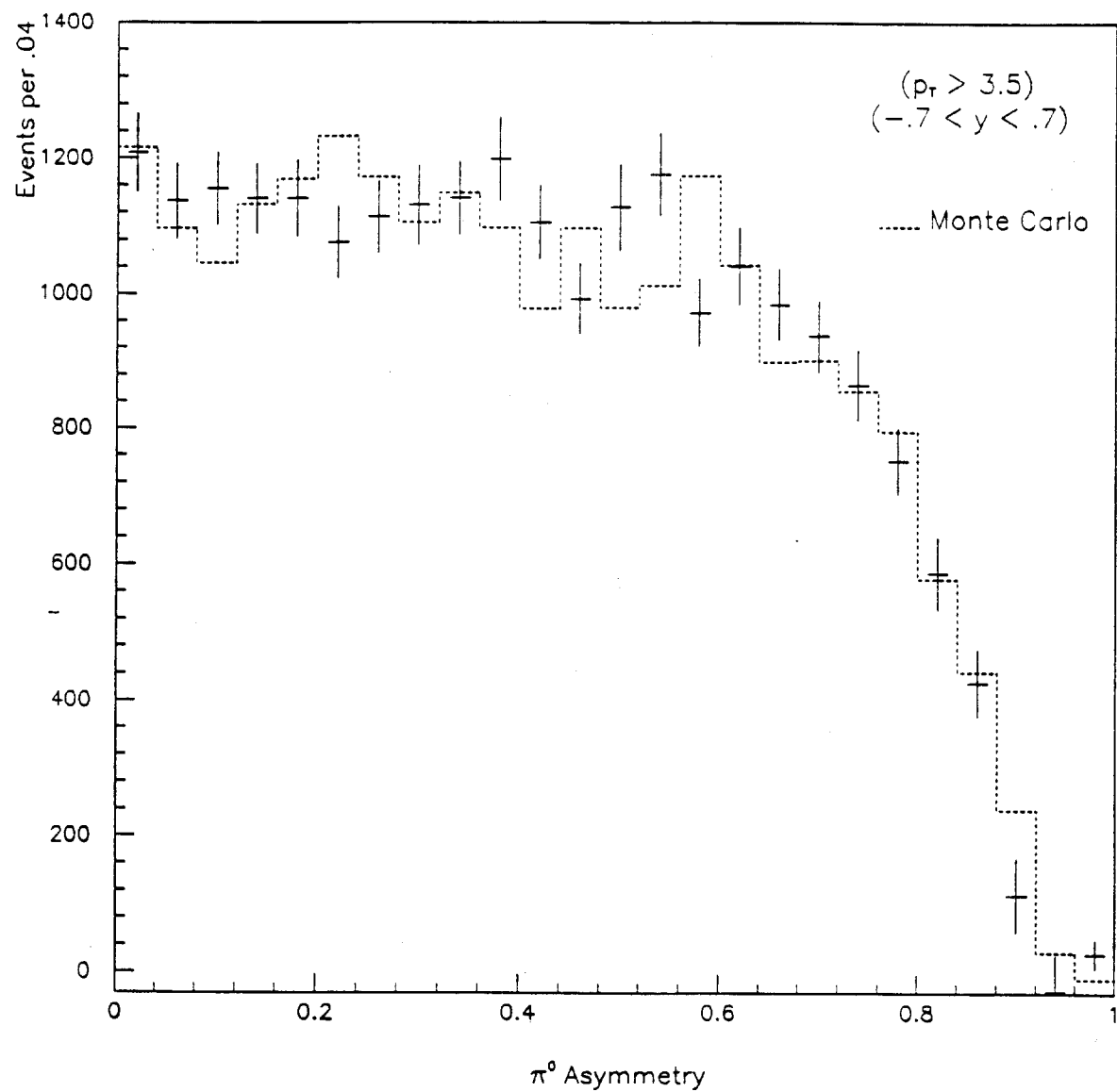


Figure 45 – π^0 asymmetry distribution. The points represent the measured asymmetry distribution for a sample of the data. The dashed line is the asymmetry distribution predicted by Monte Carlo. Detection efficiency corrections have been applied to both plots.

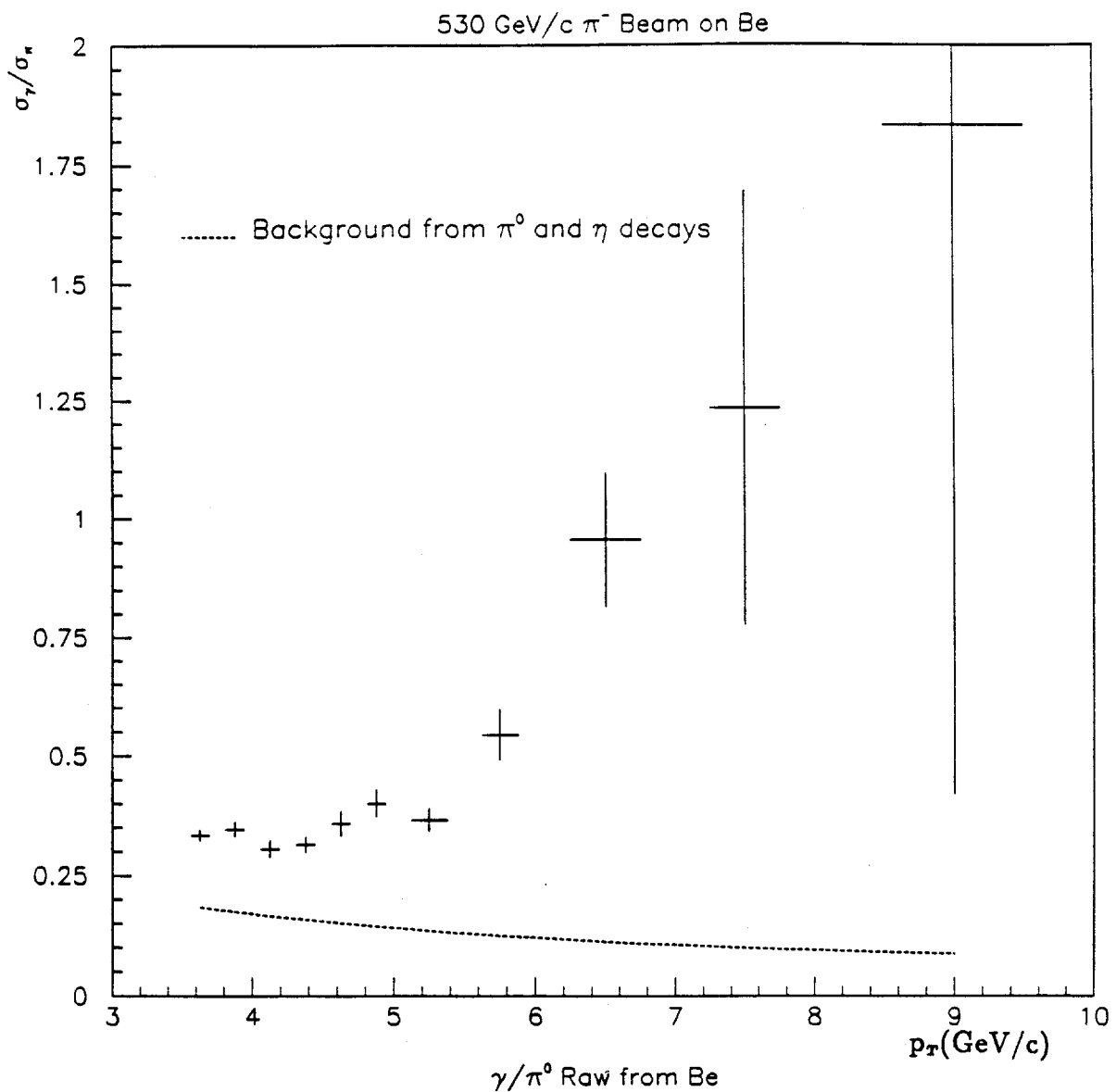


Figure 46 – Ratio of single photons to π^0 's. Background expected from misidentified π^0 's and η 's is indicated.

has been subtracted. The resulting distribution is used to estimate the number of good photons falling outside of the timing cut. For the purpose of this study, out-of-time sidebands are defined as $-100 < t < -15$ ns and $40 < t < 100$ ns. In this plot, 1377 photons fall within the cuts, and 48 fall in the out-of-time sidebands. Thus it is calculated that $3.5 \pm .5\%$ of good photons are expected to fall within the out-of-time sidebands.

Figure 48 shows the time distribution for direct photon candidates which did not form a π^0 or η mass with any asymmetry. Again, all cuts except timing have been applied. In this plot, 151 photons fall in the out-of-time bands. This compares to the 135.3 ± 19.3 predicted by the π^0 photon distribution. This indicates a residual contamination in the tails of 15.7 ± 22.8 , or consistent with zero.

Of course any residual out-of-time muons would be cut from the sample by the timing cut. To relate this out-of-time limit to in-time contamination, it is necessary to get a time profile for muon induced events. To do this, all direct photon cuts are removed except the veto wall cut*. In order to select muons from this sample, directionality is required to be greater than .4 cm. This insures a virtually pure sample of muons.

Figure 49 shows the time profile of muon induced events. By using this plot, the fraction of muons falling within the timing cut can be calculated. The ratio of muons falling within the timing cut to muons falling in the sidebands is measured to be $.80 \pm .11$. Applying this to the time profile comparison described above, the muon contamination in the direct photon sample is estimated to be 12.6 ± 18.2 events or a fraction $.3 \pm .5\%$ of the total in-time signal for $p_T > 3.5$ GeV/c. To test the effect in the high- p_T region alone, the time distribution is plotted in figure 50 for single photon candidates with $p_T > 6.0$ GeV/c. Based

* Leaving in the veto wall cut may seem a bit strange at first, but recall that while taking data the veto wall rejected events with certain time characteristics (see figure 34). Thus the only way to get a truly unbiased sample offline is to cut on the veto wall signal and rely on the veto wall inefficiency.

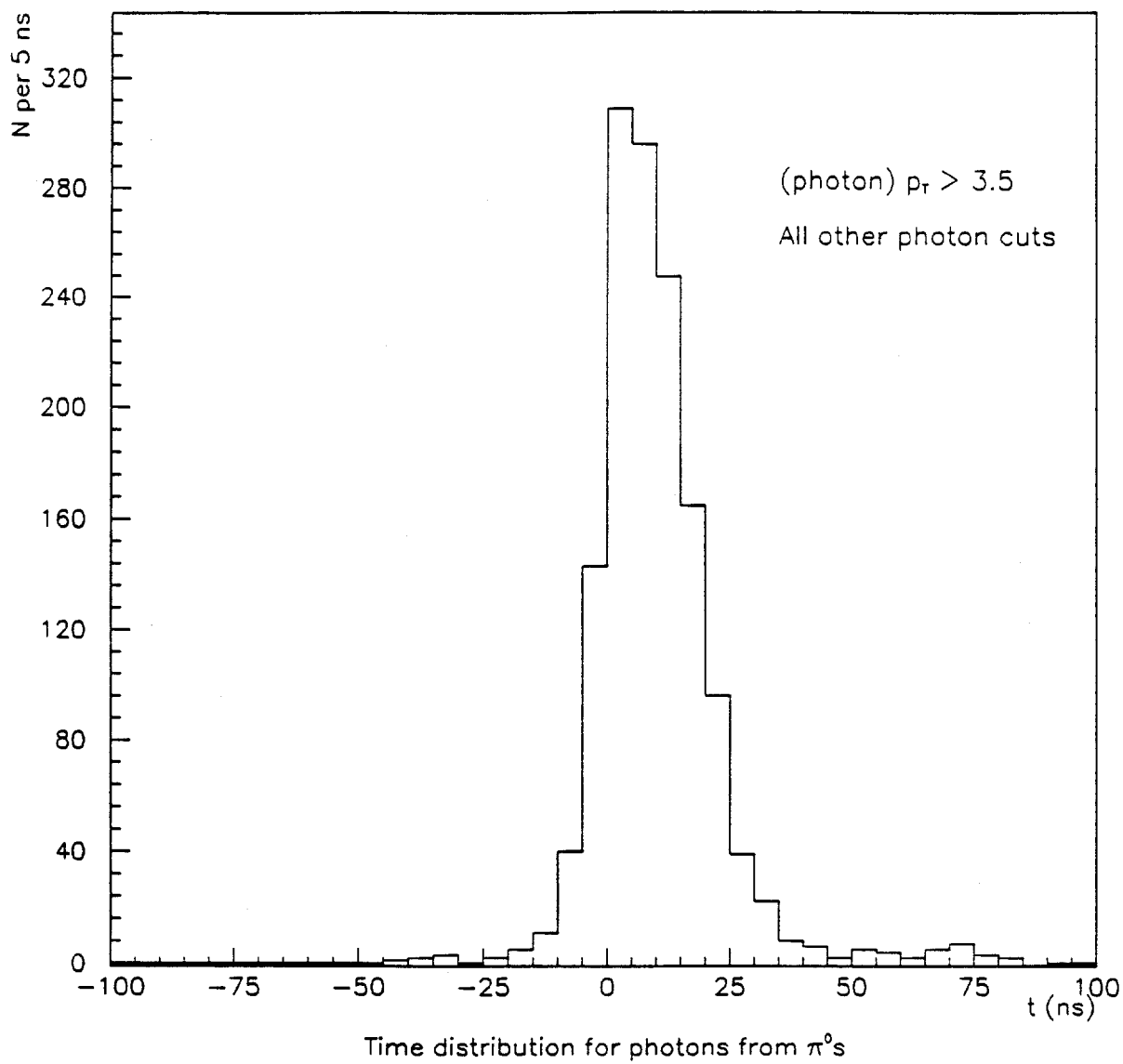


Figure 47 – Time distribution for photons which formed a π^0 mass with an asymmetry less than .75. The p_T cut is on the individual photon p_T . All direct photon cuts have been applied to this distribution.

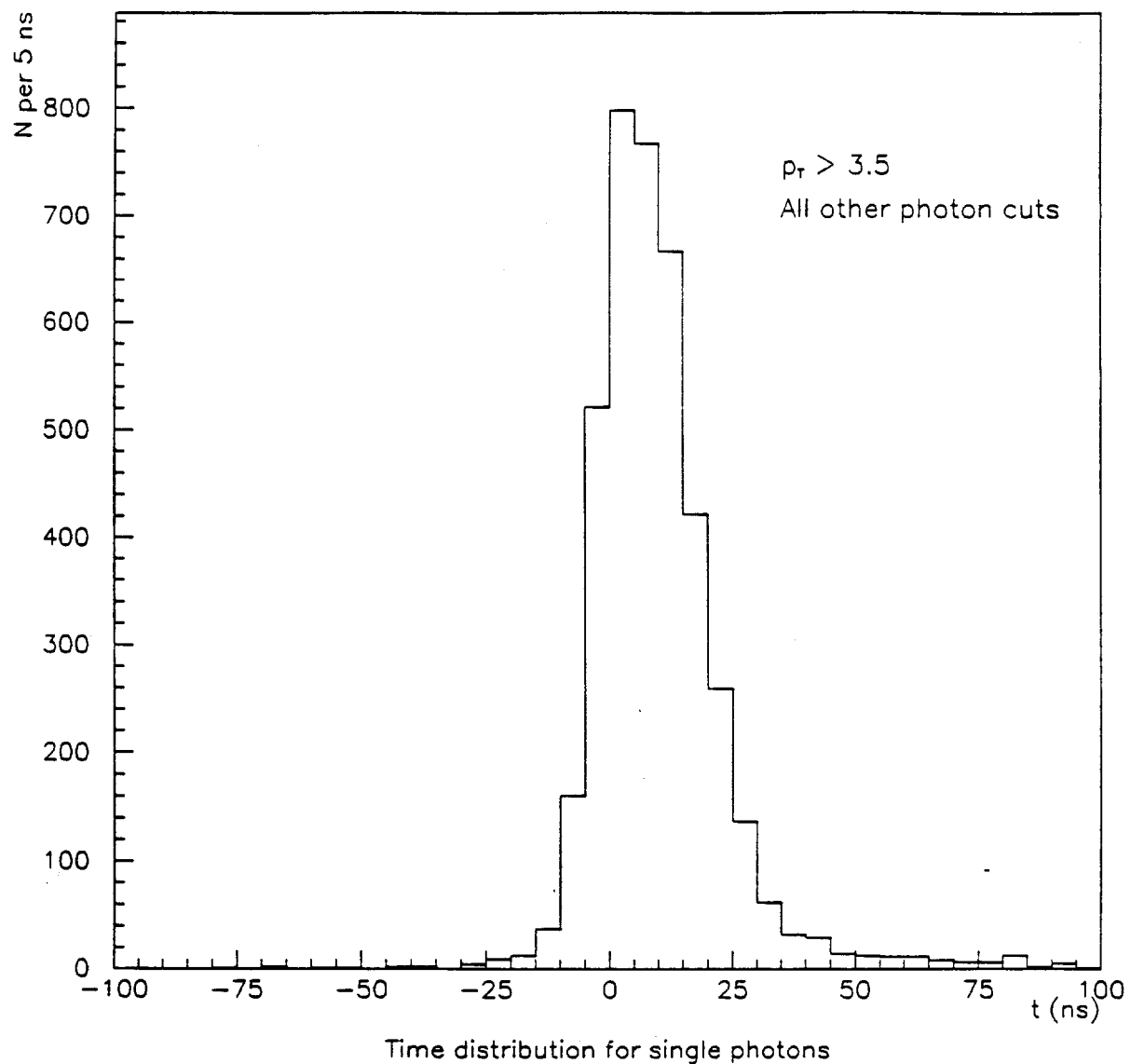


Figure 48 – Time distribution for photons which did not combine with any other photon to form a π^0 mass.

on this plot, muon contamination is estimated to be $-1.3 \pm 1.2\%$ for $p_T > 6.0$ GeV/c.

A similar study was performed on the data from positive beam. The muon contamination was found to be $.4 \pm .9\%$ in the range $p_T > 4.25$ GeV/c and $1.0 \pm 3.0\%$ for $p_T > 6.0$ GeV/c.

In summary, this study indicates that muon contamination is negligible within statistical errors.

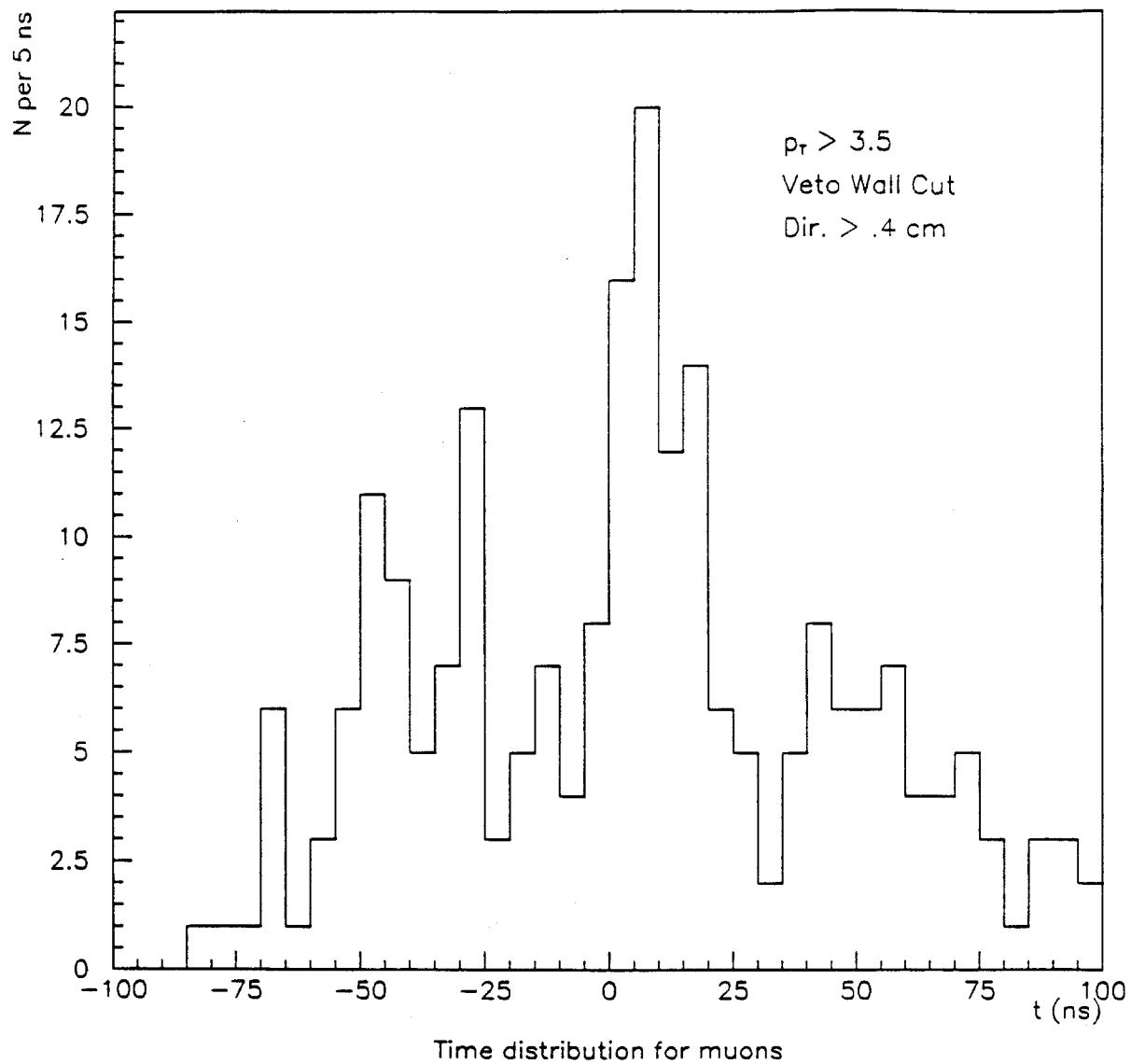


Figure 49 – Time profile for muon induced events. A high directionality is required to select muons. The veto wall cut has been imposed to insure an unbiased time distribution. This has the unfortunate effect of reducing statistics.

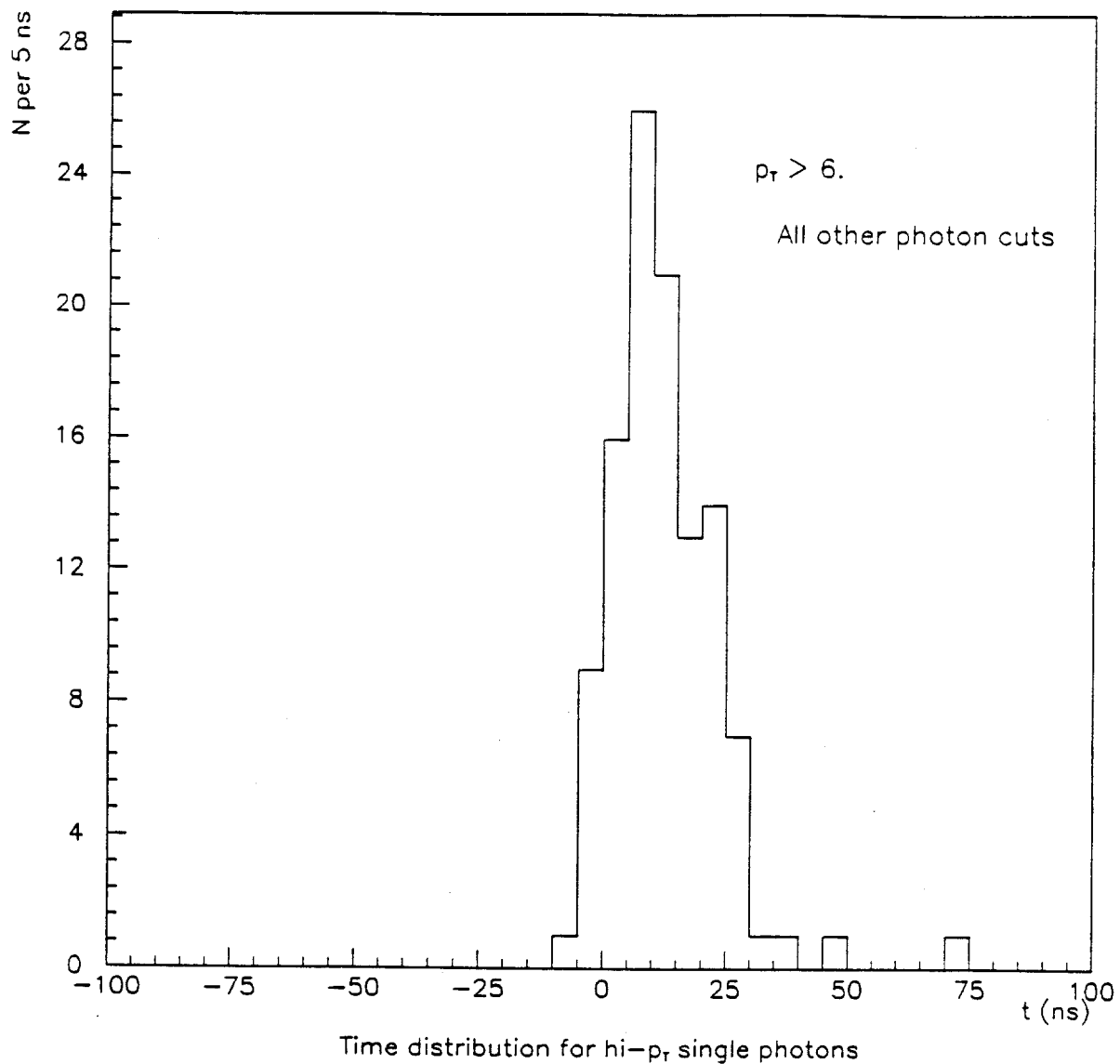


Figure 50 – Time profile for high- p_T photons. Tails are consistent with tails from π^0 photons, indicating negligible muon contamination.

8. Results

8.1 DIRECT PHOTON CROSS-SECTION

Results for direct photon production from incident π^- ^{*}, in the range $3.5 < p_T < 10$ GeV/c, are shown in figure 51 through figure 54. Figure 51 shows the inclusive invariant cross-section per nucleon for $\pi^- + Be \rightarrow \gamma + X$ [†] as a fraction of the cross-section for $\pi^- + Be \rightarrow \pi^0 + X$, measured in the same sample. The contribution due to π^0 and η decays has been subtracted from this “ γ/π ” plot. The background subtracted cross-section per nucleon for $\pi^- + Be \rightarrow \gamma + X$ is shown in figure 52. Similarly, for the $\pi^- + Cu$ data, figures 53 and 54 show the background subtracted γ/π ratio and direct photon cross-section per nucleon respectively. All results are averaged over the rapidity interval $-.7 < y < .7$.

For the data from incident proton beam, results are shown in figure 55 through figure 58, in the range $4.25 < p_T < 8$ GeV/c. Figures 55 and 56 show the γ/π ratio and inclusive invariant cross-section per nucleon for $p + Be$, respectively. These plots are shown for $p + Cu$ in figures 57 and 58. Again, all results are averaged over the rapidity interval $-.7 < y < .7$.

The γ/π plots are a traditional way to study direct photon data. For the $\pi^- + Be$ data, we see a rise with increasing p_T . This is what one expects based on the fact that the photons are produced directly in the reaction, while the π^0 's are the result of parton fragmentation. The other reactions show some indication of a rising trend, but statistics are limited at the higher points.

Cross-section results are summarized in table 15 and table 16, which list both the measured direct photon cross-sections, and these values as a fraction of the corresponding π^0 cross-sections. The average p_T value for each point represents the weighted center of photon cross-section distribution for each p_T bin.

* Recall from chapter 3 that the π^- beam had a contamination of 2.9% K^- and .2% \bar{p} .
 The proton beam had a contamination of 7.2% π^+ and 1.5% K^+ .

† “X” refers to anything else produced in the reaction.

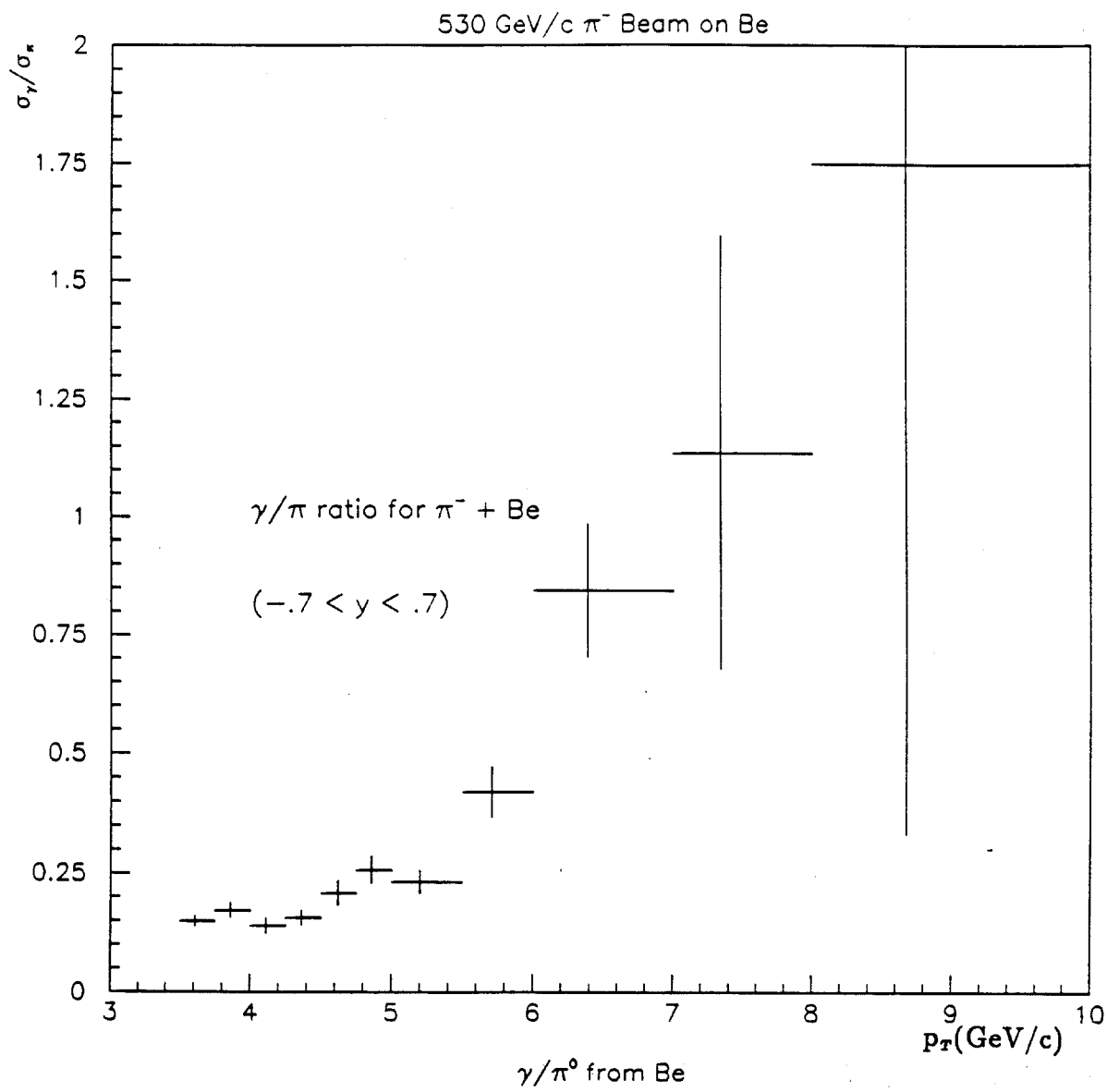


Figure 51 – Ratio of the cross-section for $\pi^- + \text{Be} \rightarrow \gamma + X$ to the cross-section for $\pi^- + \text{Be} \rightarrow \pi^0 + X$.

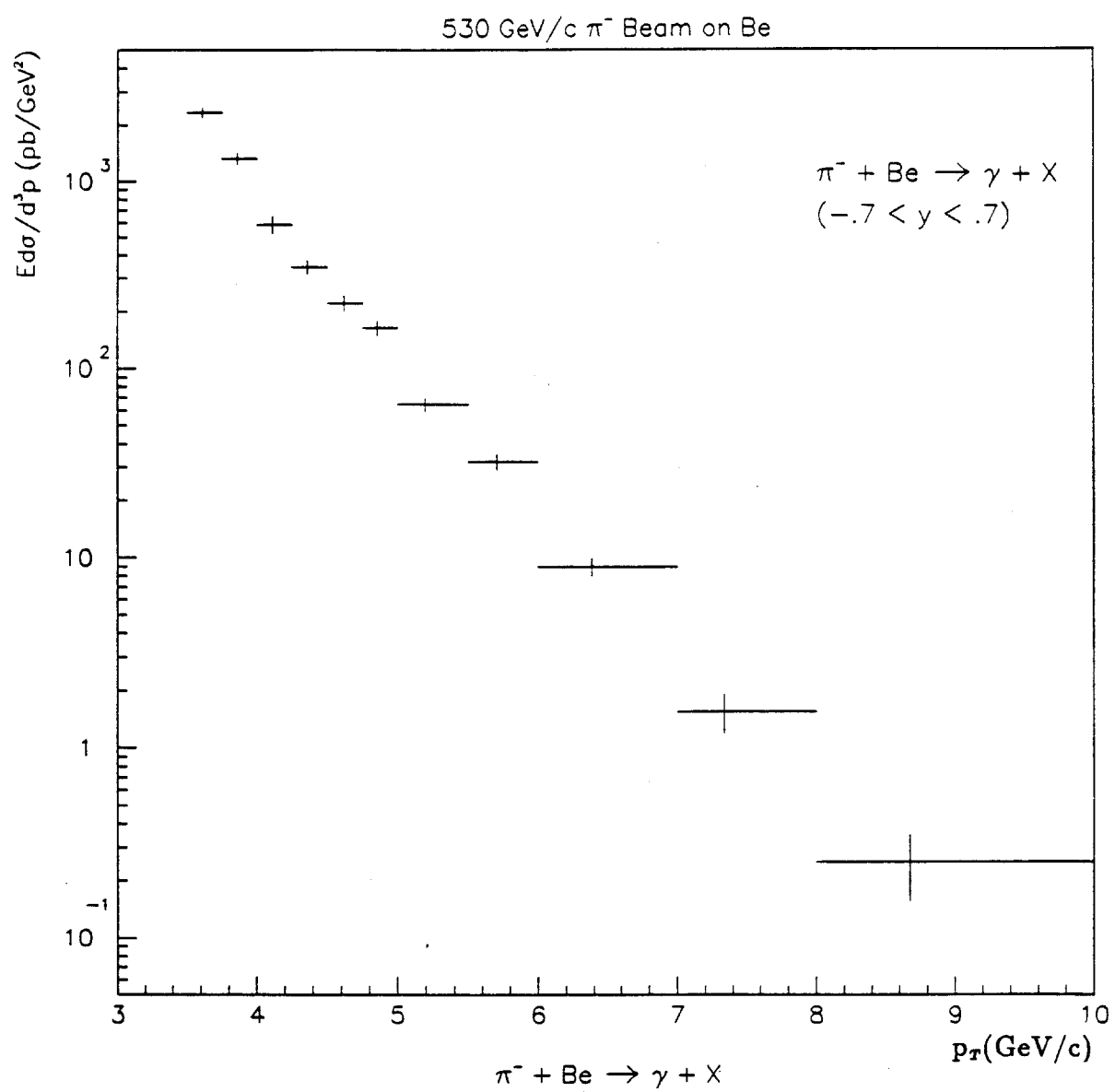


Figure 52 – Direct photon inclusive invariant cross-section per nucleon for π^- beam on beryllium.

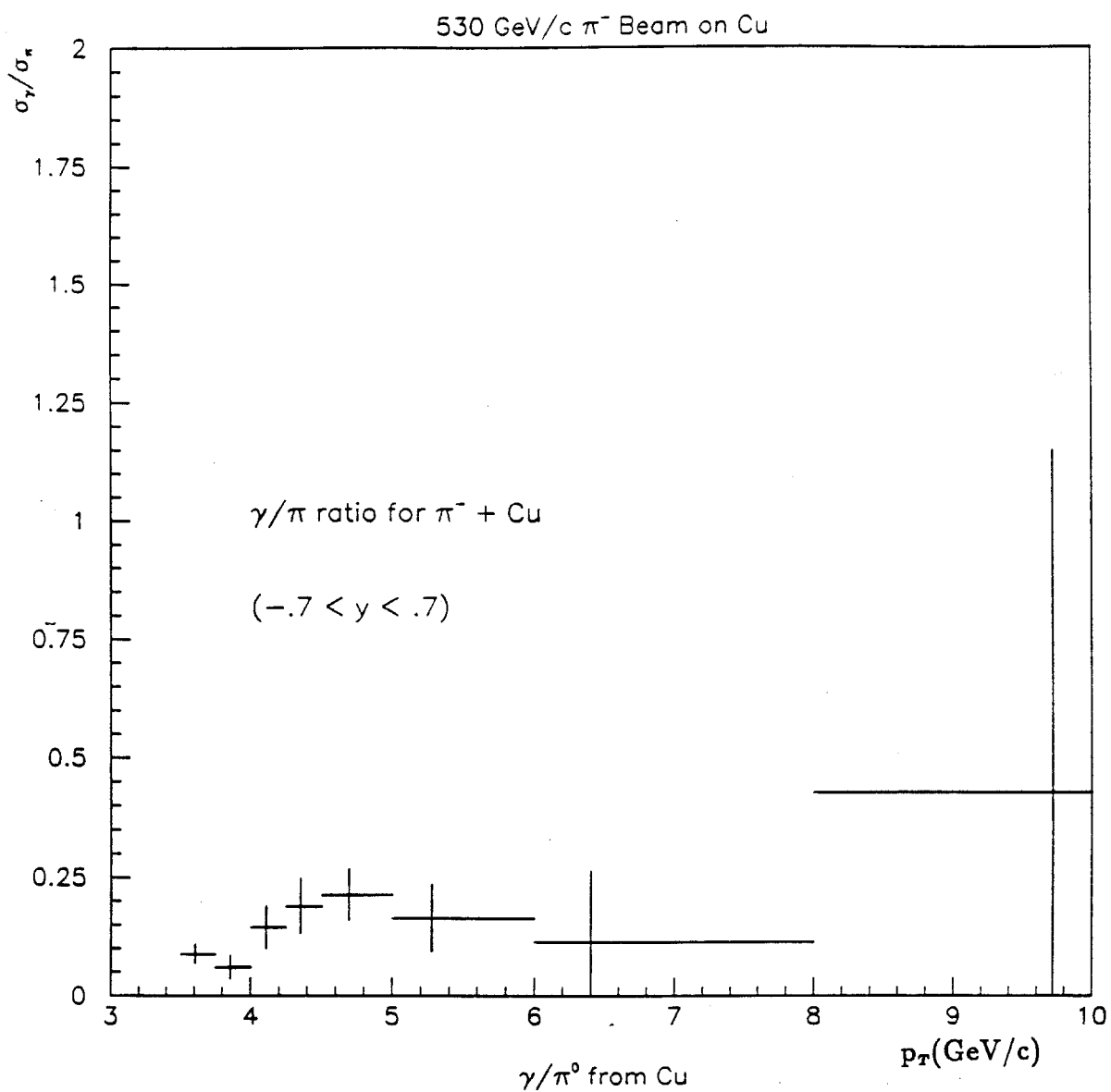


Figure 53 – Ratio of the cross-section for $\pi^- + \text{Cu} \rightarrow \gamma + X$ to the cross-section for $\pi^- + \text{Cu} \rightarrow \pi^0 + X$.

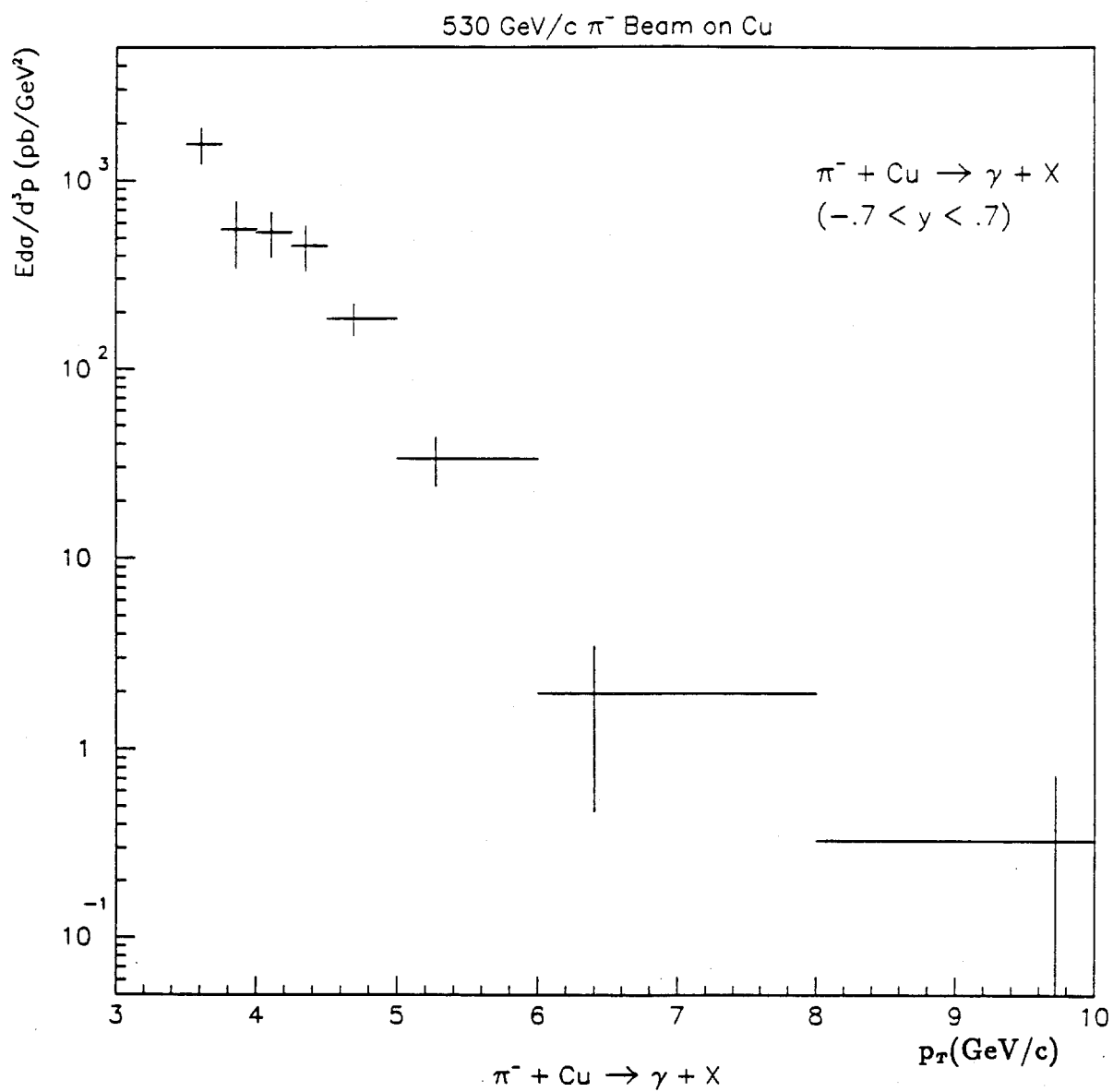


Figure 54 – Direct photon inclusive invariant cross-section per nucleon for π^- beam on copper.

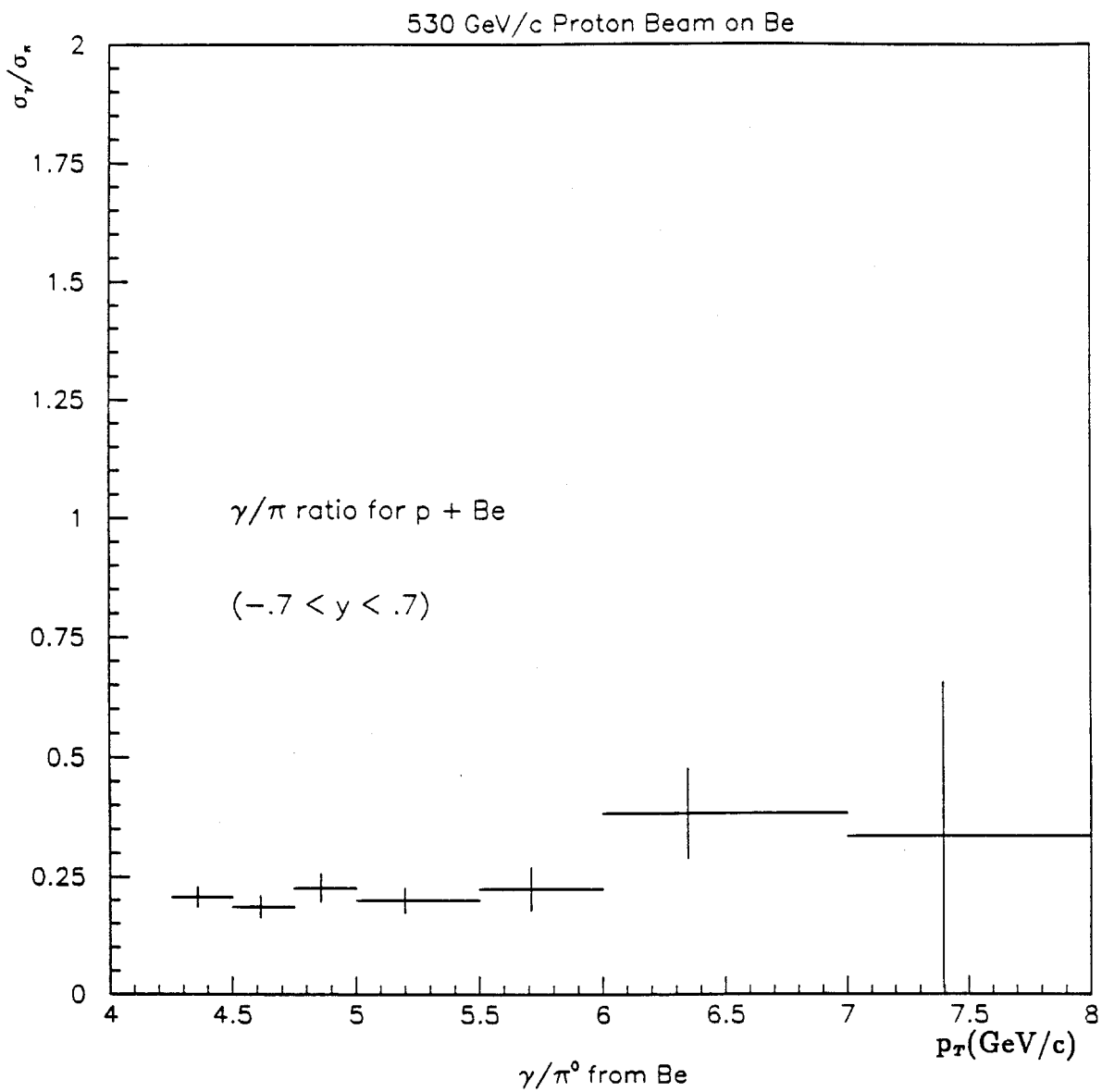


Figure 55 – Ratio of the cross-section for $p + Be \rightarrow \gamma + X$ to the cross-section for $p + Be \rightarrow \pi^0 + X$.

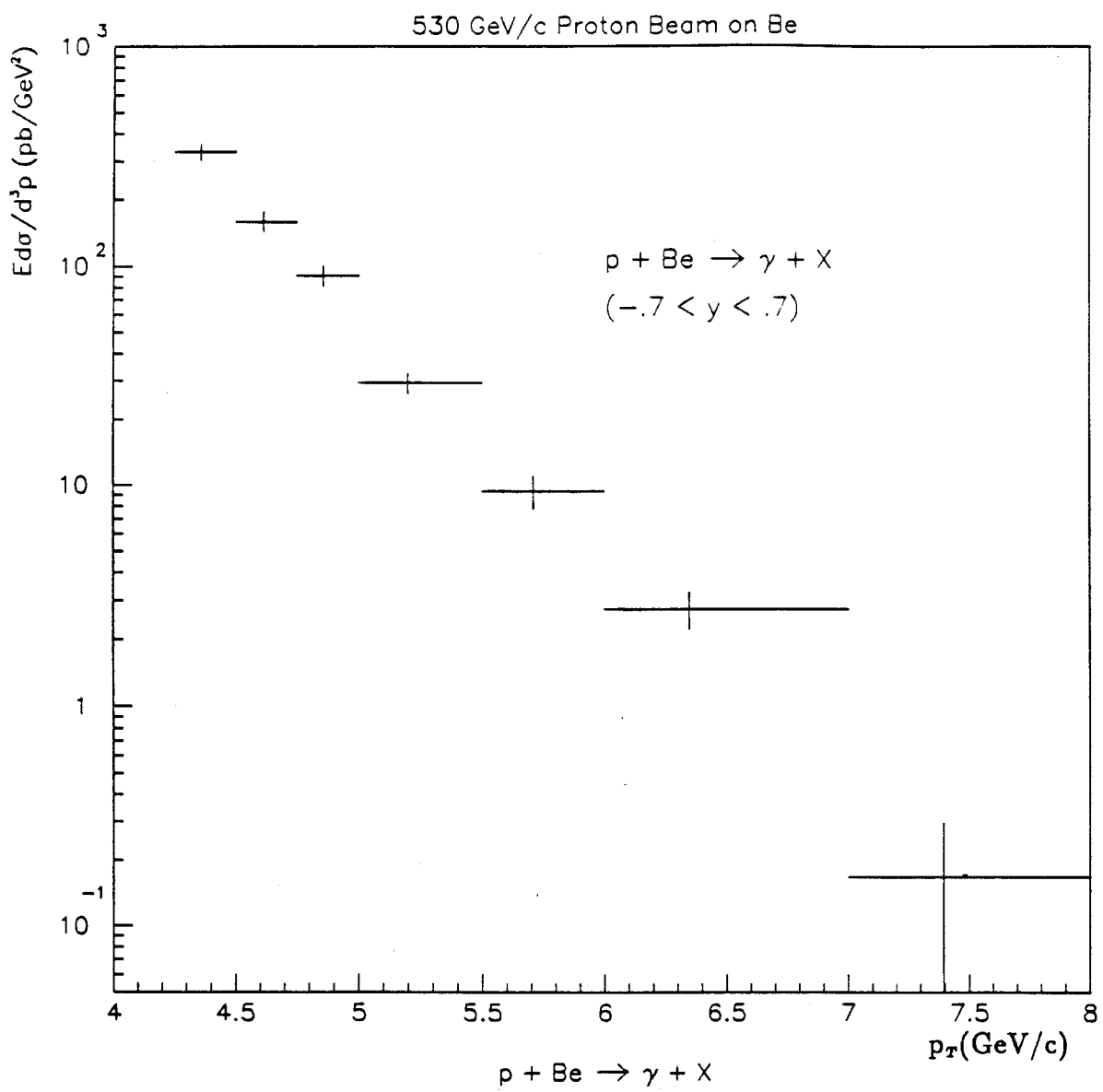


Figure 56 – Direct photon inclusive invariant cross-section per nucleon for proton beam on beryllium.

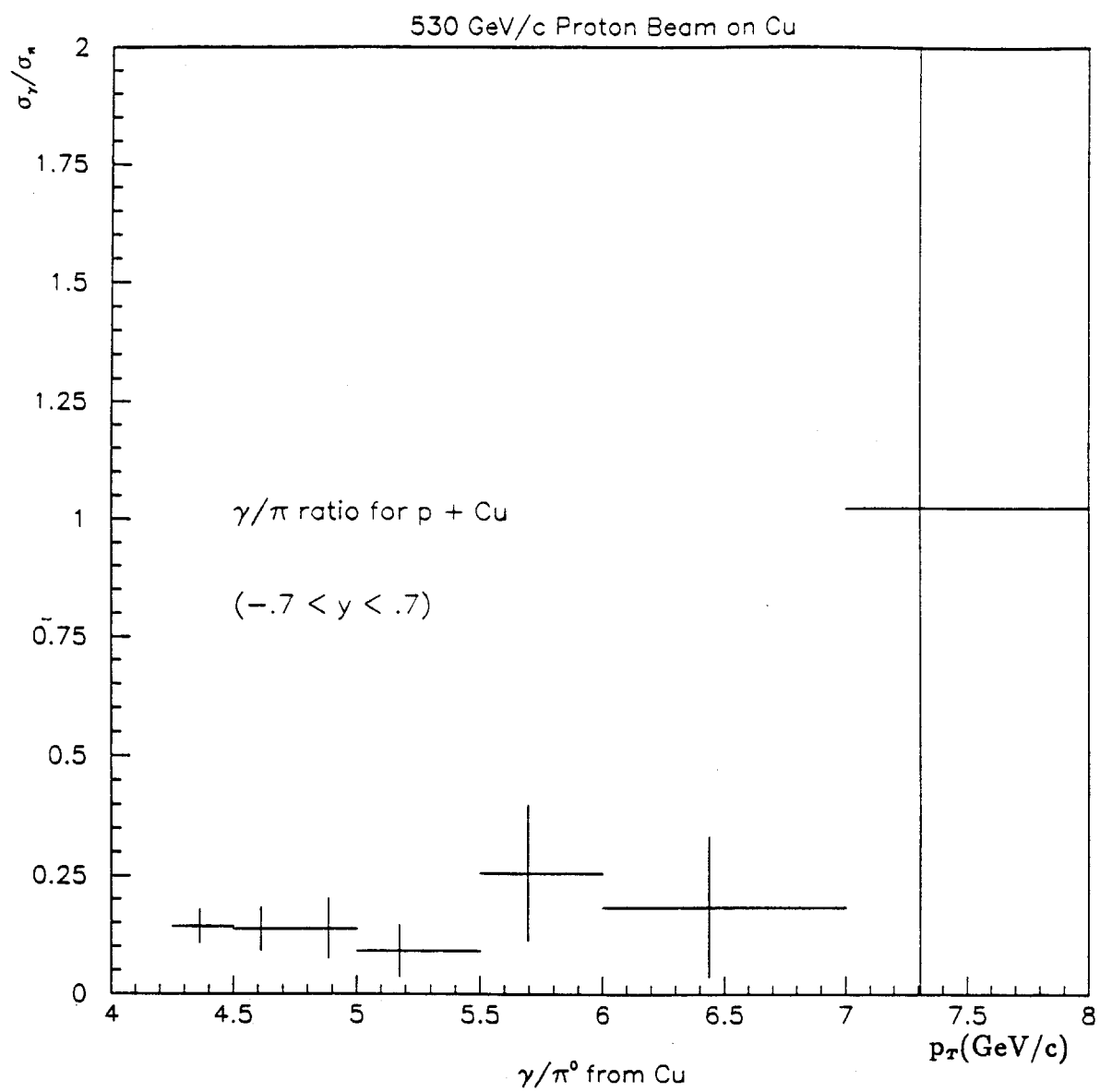


Figure 57 – Ratio of the cross-section for $p + Cu \rightarrow \gamma + X$ to the cross-section for $p + Cu \rightarrow \pi^0 + X$.

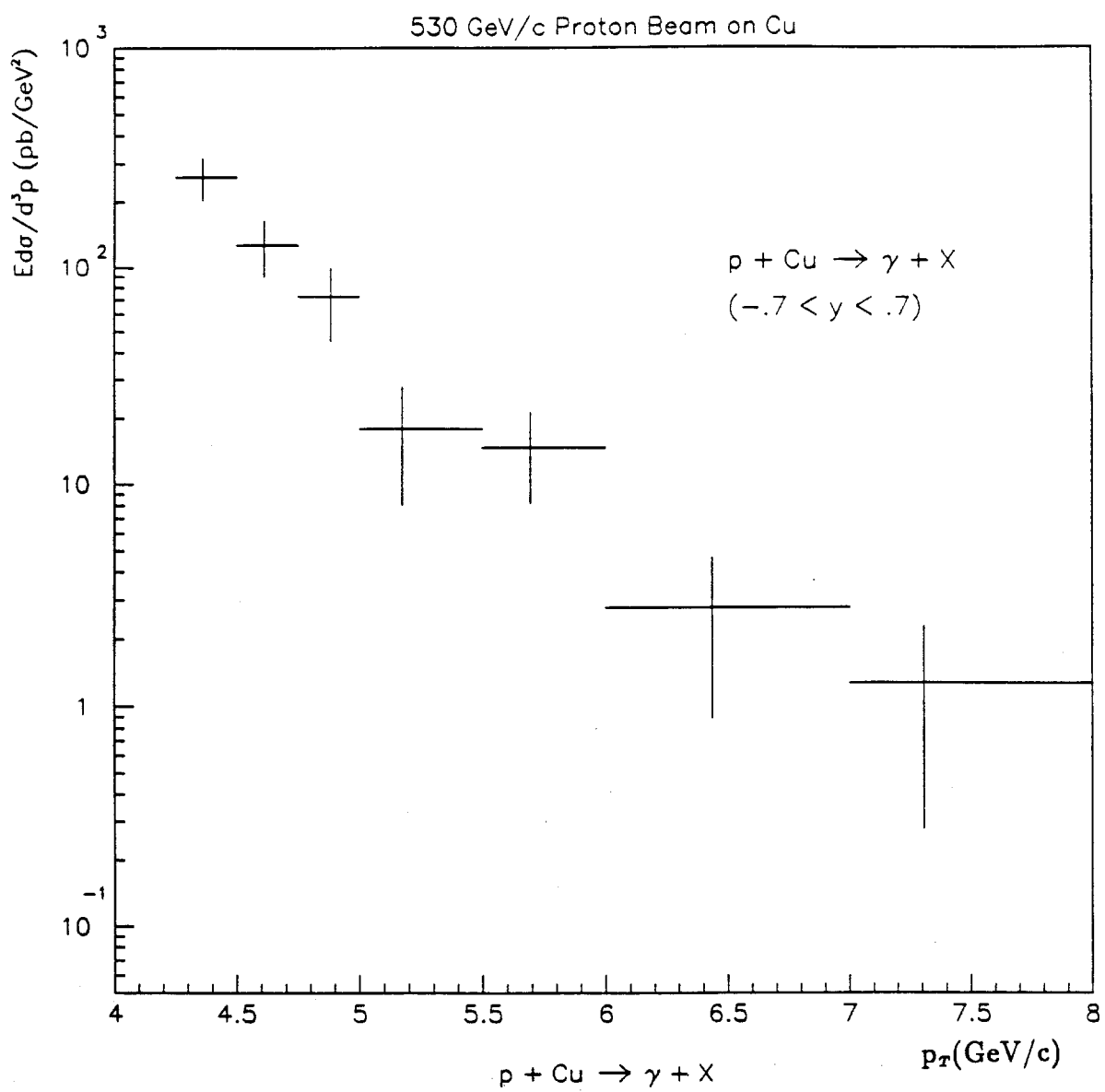


Figure 58 – Direct photon inclusive invariant cross-section per nucleon for proton beam on copper.

$\pi^- + Be \rightarrow \gamma + X$				
Low p_T (GeV/c)	High p_T (GeV/c)	Avg. p_T (GeV/c)	" γ/π " —	$E \frac{d\sigma}{d^3p}$ (pb/GeV ²)
3.50	3.75	3.61	.149 ± .011	2334.5 ± 147.9
3.75	4.00	3.86	.171 ± .015	1322.6 ± 95.4
4.00	4.25	4.11	.140 ± .017	588.0 ± 62.9
4.25	4.50	4.36	.157 ± .016	348.4 ± 29.1
4.50	4.75	4.62	.208 ± .027	222.0 ± 22.7
4.75	5.00	4.86	.257 ± .028	165.3 ± 14.5
5.00	5.50	5.20	.232 ± .025	65.2 ± 5.4
5.50	6.00	5.71	.420 ± .053	32.3 ± 3.0
6.00	7.00	6.39	.846 ± .142	8.98 ± .97
7.00	8.00	7.34	1.138 ± .460	1.55 ± 0.36
8.00	10.00	8.67	1.748 ± 1.41	0.251 ± .094
$\pi^- + Cu \rightarrow \gamma + X$				
Low p_T (GeV/c)	High p_T (GeV/c)	Avg. p_T (GeV/c)	" γ/π " —	$E \frac{d\sigma}{d^3p}$ (pb/GeV ²)
3.50	3.75	3.60	.088 ± .021	1556.9 ± 337.4
3.75	4.00	3.86	.060 ± .025	558.3 ± 216.4
4.00	4.25	4.11	.145 ± .046	537.0 ± 146.3
4.25	4.50	4.35	.189 ± .058	456.2 ± 124.9
4.50	5.00	4.70	.213 ± .055	185.8 ± 36.5
5.00	6.00	5.28	.164 ± .071	33.8 ± 9.98
6.00	7.00	6.40	.113 ± .151	1.96 ± 1.50
7.00	10.0	9.72	.427 ± .725	0.33 ± 0.40

Table 15 – Direct photon cross-sections for incident π^- beam. The background due to π^0 and η decays has been subtracted.

$p + Be \rightarrow \gamma + X$				
Low p_T (GeV/c)	High p_T (GeV/c)	Avg. p_T (GeV/c)	“ γ/π ” —	$E \frac{d\sigma}{d^3 p}$ (pb/GeV ²)
4.25	4.50	4.36	.207 ± .022	332.4 ± 29.0
4.50	4.75	4.62	.186 ± .024	160.1 ± 16.7
4.75	5.00	4.86	.226 ± .031	91.2 ± 10.0
5.00	5.50	5.20	.199 ± .027	29.6 ± 3.2
5.50	6.00	5.71	.223 ± .047	9.39 ± 1.63
6.00	7.00	6.35	.382 ± .096	2.74 ± 0.52
7.00	8.00	7.39	.334 ± .322	0.168 ± 0.128
$p + Cu \rightarrow \gamma + X$				
Low p_T (GeV/c)	High p_T (GeV/c)	Avg. p_T (GeV/c)	“ γ/π ” —	$E \frac{d\sigma}{d^3 p}$ (pb/GeV ²)
4.25	4.50	4.36	.143 ± .036	260.8 ± 56.9
4.50	4.75	4.61	.137 ± .046	127.3 ± 37.5
4.75	5.00	4.88	.137 ± .064	72.8 ± 27.8
5.00	5.50	5.17	.091 ± .056	18.0 ± 10.0
5.50	6.0	5.70	.256 ± .144	14.8 ± 6.6
6.00	7.00	6.44	.184 ± .149	2.79 ± 1.90
7.00	8.00	7.31	1.03 ± 1.38	1.29 ± 1.01

Table 16 – Direct photon cross-sections for incident proton beam. The background due to π^0 and η decays has been subtracted.

8.2 SYSTEMATIC ERRORS

Errors quoted in this chapter are statistical only. Several possible sources of systematic error are discussed in this section.

Because of the steep p_T dependence of the cross-section distributions, these measurements are very sensitive to uncertainties in the p_T scale. To estimate this effect, a parametrized fit of the form

$$E \frac{d\sigma}{d^3 p} = \frac{A}{p_T^n} \quad (8.1)$$

is applied to the $\pi^- + Be$ cross-section. The best fit gives $A = (8.25 \pm 1.74) \times 10^8$ and $n = 9.91 \pm .02$, with a χ^2 per degree of freedom of 2.25. This indicates that

$$\frac{\Delta(E \frac{d\sigma}{d^3 p})}{E \frac{d\sigma}{d^3 p}} \approx 10 \times \frac{\Delta p_T}{p_T} \quad (8.2)$$

The uncertainty in the p_T measurement can be written as

$$\left(\frac{\Delta p_T}{p_T} \right)^2 = \left(\frac{\Delta E}{E} \right)^2 + \left(\frac{\Delta \sin(\theta)}{\sin(\theta)} \right)^2 \quad (8.3)$$

where E is the energy of the photon and θ is the production angle in the lab frame. Because the position resolution of the EMLAC is better than 1 mm, the contribution from the $\sin(\theta)$ term is negligible.

The energy scale was determined on an octant by octant basis by requiring the π^0 mass to have a value of 135 MeV. The uncertainty in the energy scale can be estimated by measuring the remaining variation in the π^0 mass measurement at different points in each octant. The variation of the π^0 mass with radial position after rescaling was found to be 1.3%. Using this as a measure of the uncertainty in the energy scale indicates a systematic cross-section uncertainty on the order of 15%.

The overall normalization error arising from the various global cross-section corrections (C_{cuts}^γ) is determined by adding the errors of each of the terms in quadrature and found to be about 1%. The beam normalization error has been estimated to be on the order of .2%^[45], or negligible compared to statistical errors.

Of the errors in the various efficiency corrections, the largest is in the vertex efficiency, with an error of 2%. A detailed study of the error in the trigger efficiency correction is still underway, but because this correction was usually below 10% in the p_T range studied, this is not expected to be a major source of systematic error.

A large source of systematic uncertainty comes from the correction for π^0 and η background. The fit used to generate the false γ/π background returned an absolute error of $\pm .01$. A more conservative worst-case estimation, based on assuming different functional forms for the fit, would be $\pm .02$ for $p_T < 5.5$ GeV/c and $\pm .03$ for $p_T \geq 5.5$ GeV/c. The exact effect on the measured cross-section depends on the γ/π ratio at a given point, but in general this represents about a 20% worst-case uncertainty.

8.3 NUCLEAR DEPENDENCE

Figure 59 shows a comparison of direct photon production from copper and beryllium targets as a function of p_T . The ratio of the cross-section per nucleon is shown for incident π^- beam in 59a. This ratio is shown for incident proton beam in 59b. Within errors, there are no obvious p_T dependencies in either plot. We see that the values in both plots are systematically less than one. This is interesting because it would seem to indicate nuclear effects. However, the error bars are large. Assuming a scaling for the cross-section per nucleus of the form A^α , α is related to the cross-section per nucleon by

$$\alpha = \frac{\log(\sigma_{Cu}/\sigma_{Be})}{\log(A_{Cu}/A_{Be})} + 1 \quad (8.4)$$

where σ_x is the cross-section per nucleon for a given target. Figures 59c and

59d show this alpha representation for the data from the π^- beam and proton beam respectively.

8.4 BEAM DEPENDENCE

The ratio of the direct photon invariant cross-sections for $\pi^- + Be$ to $p + Be$ is shown in figure 60 as a function of p_T . We see that this ratio increases with increasing p_T . The ratio is near unity at a p_T of about 4.5 GeV/c, rising to nearly four at 7.5 GeV/c. This is the behavior one expects based on the fact that the individual partons in the π^- beam have a higher average fraction of total beam momentum than the partons in the proton beam. Also, the $u\bar{u}$ annihilation diagram contributes in the case of the incident π^- , but not in the case of the incident proton. These data are summarized in table 17.

p_T (GeV/c) :	4.25 - 4.5	4.5 - 4.75	4.75 - 5.0	5.0 - 6.0	6.0 - 8.0
$\frac{\pi^- + Be \rightarrow \gamma + X}{p + Be \rightarrow \gamma + X}$	$1.05 \pm .13$	$1.39 \pm .20$	$1.81 \pm .25$	$2.50 \pm .28$	$3.62 \pm .76$

Table 17 – Dependence of direct photon production on beam type.

8.5 COMPARISON WITH OTHER EXPERIMENTS

Figure 61 shows the E706 cross-section per nucleon for $\pi^- + Be \rightarrow \gamma + X$ compared to previous measurements from $\pi^- +$ nucleon reactions (refer to the discussion of previous experiments, section 2.4). All of the other experiments shown had energies in the center of mass (\sqrt{s}) near 20 GeV, so it is not surprising that the E706 data are systematically higher. Figure 62 shows a similar comparison for between the $p + Be$ data and previous $p +$ nucleon results. Of these, the other fixed target experiments (WA70, NA24, NA3, and E629) again all had \sqrt{s} near 20 GeV, while the collider experiments (R108 and R806) had \sqrt{s} near 65 GeV/c. As expected, the E706 data lie between these two groups; however, there does seem to be a steeper p_T dependence to the E706 data.

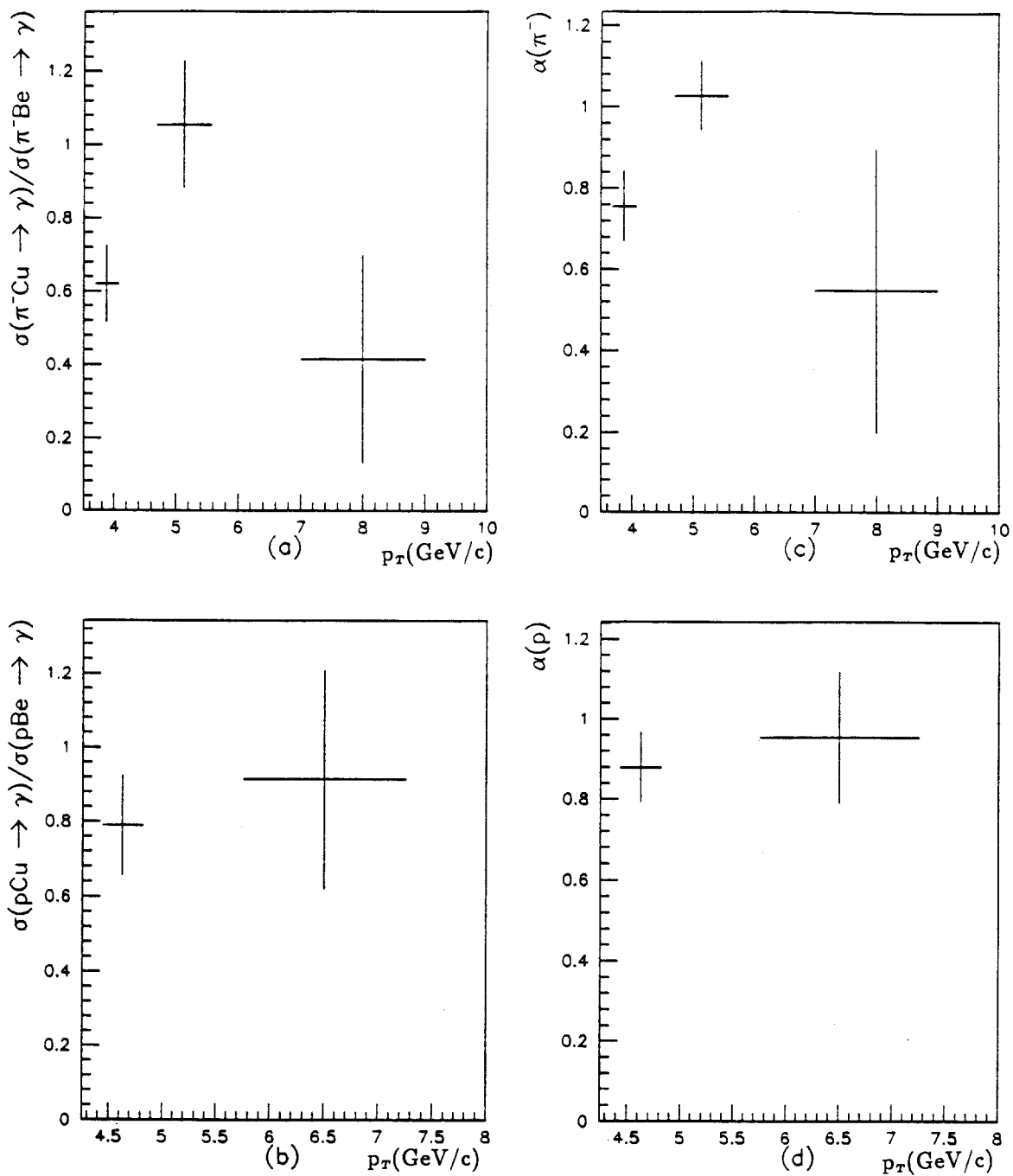


Figure 59 – Nuclear dependence of direct photon production. The ratio of the invariant cross-section per nucleon from a copper target to that from a beryllium target is shown in (a) for incident π^- and (b) for incident proton. Assuming a scaling of the form A^α , the equivalent α representations are shown in (c) and (d) respectively.

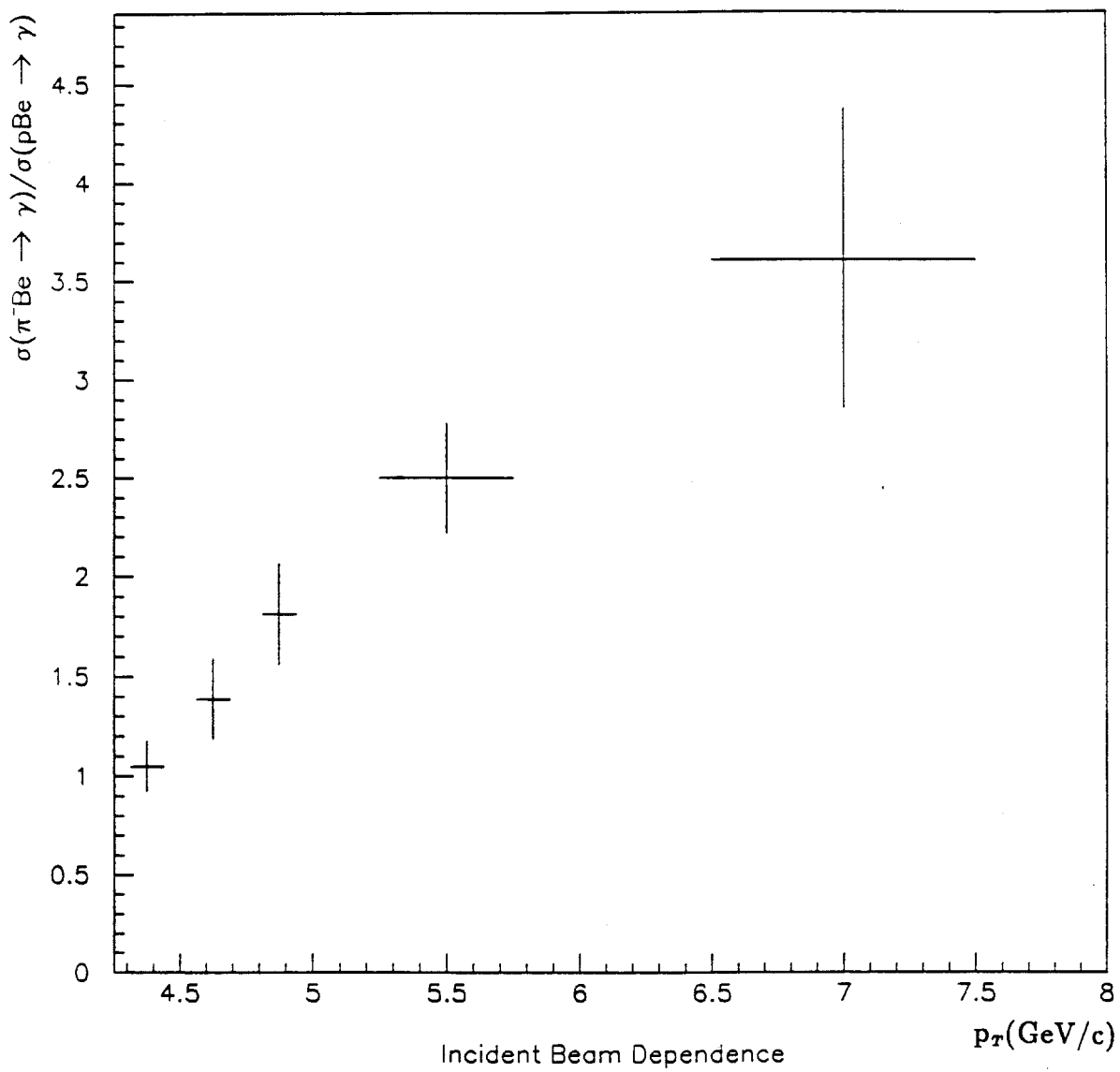


Figure 60 – Comparison of direct photon cross-sections between incident π^- and incident proton.

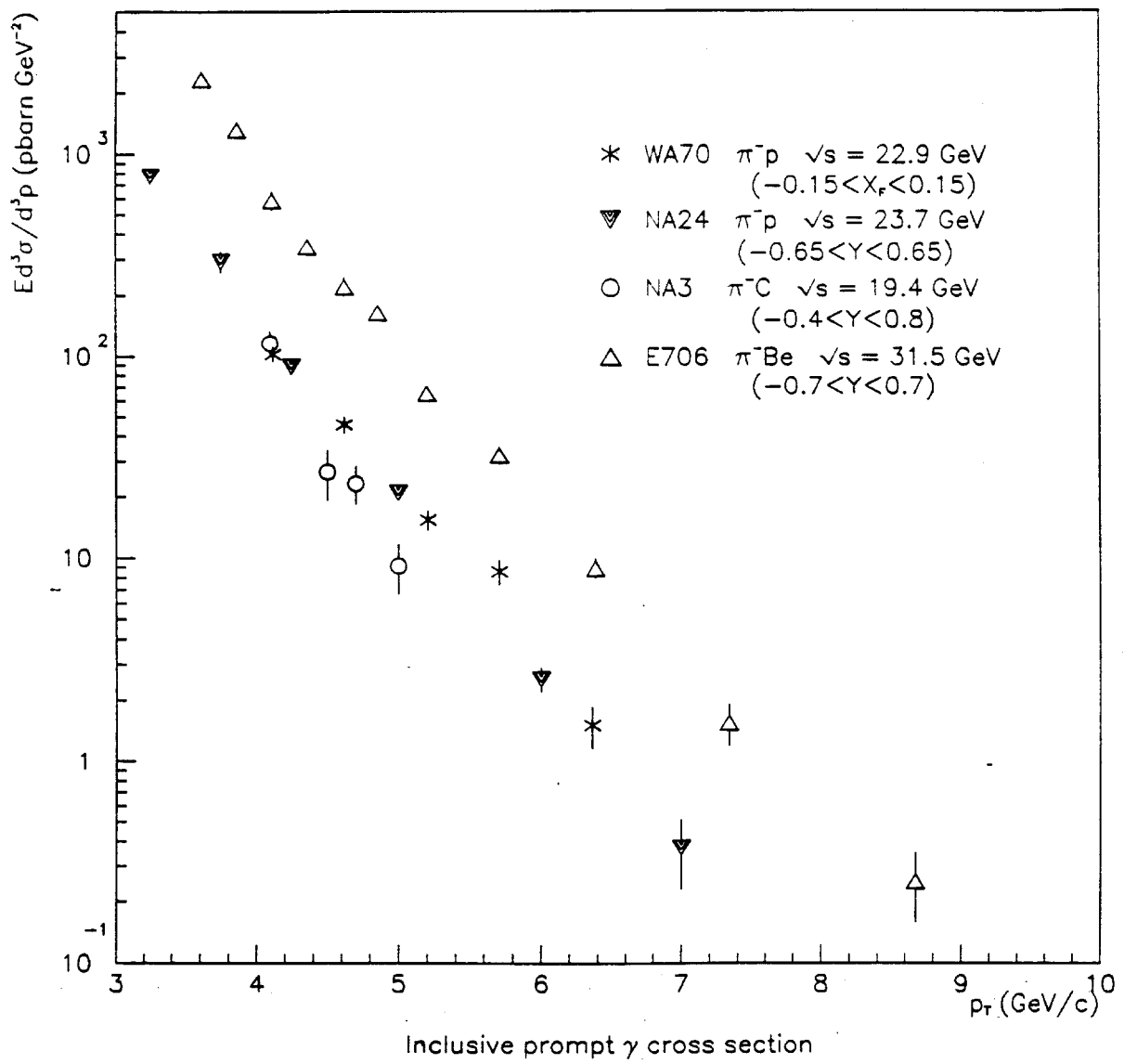


Figure 61 – Comparison of π^- data with previous results.

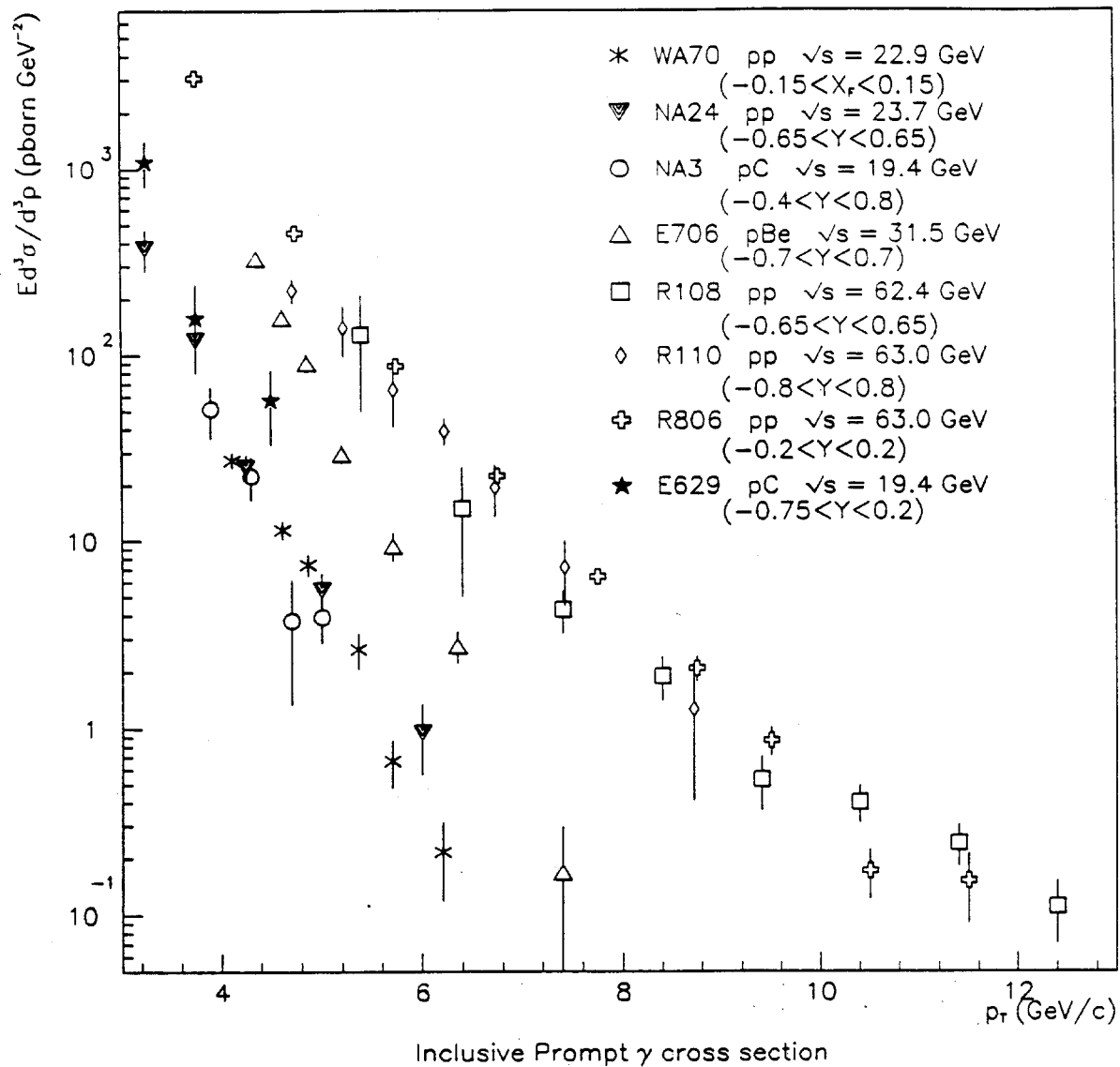


Figure 62 – Comparison of proton data with previous results.

To make a more direct comparison between direct photon data at various energies, some assumption must be made as to the dependence on \sqrt{s} . In the past, there has been success fitting direct photon data at very different energies with the form^[46]

$$E \frac{d\sigma}{d^3 p} = \frac{C}{p_T^n} x_T^a (1 - x_T)^b \quad (8.5)$$

where $x_T \equiv 2p_T/\sqrt{s}$, and C, n, a , and n are free parameters. It must be stressed that this is a purely phenomenological function with no theoretical basis.

A least-squares fit of this form to the data from incident π^- shown in figure 61 yields the following function:

$$E \frac{d\sigma}{d^3 p} = \frac{3.34 \times 10^2}{p_T^{3.61}} x_T^{-4.72} (1 - x_T)^{2.05} \quad (8.6)$$

with a χ^2 per degree of freedom of 6.1. This is not a particularly good fit, but again there is no fundamental basis for this form. Because of the high χ^2 , the fitting algorithm did not return meaningful errors for the parameters.

Figure 63 shows the $\pi^- +$ nucleon comparison again, this time as a function of x_T . In an attempt to cancel \sqrt{s} dependence, the cross section at each point has been multiplied by $p_T^{3.61}$, as indicated by (8.6). The curve predicted by the fit is shown by the dashed line. The fit seems in fair agreement with the E706 points.

A best fit of this type to the $p+$ nucleon data gives the following function:

$$E \frac{d\sigma}{d^3 p} = \frac{1.96 \times 10^6}{p_T^{5.77}} x_T^{-1.05} (1 - x_T)^{8.38} \quad (8.7)$$

with a χ^2 per degree of freedom of 8.1. The comparison with the other experiments, with this scaling, is shown in Figure 64. In this case, there are many more points with which to compare. The E706 data are in reasonable agreement with the fit above $x_T \approx .35$. However, these data clearly exhibit a steeper slope for the lower x_T points, ultimately exceeding the fit by more than a factor of two at $x_T = .25$.

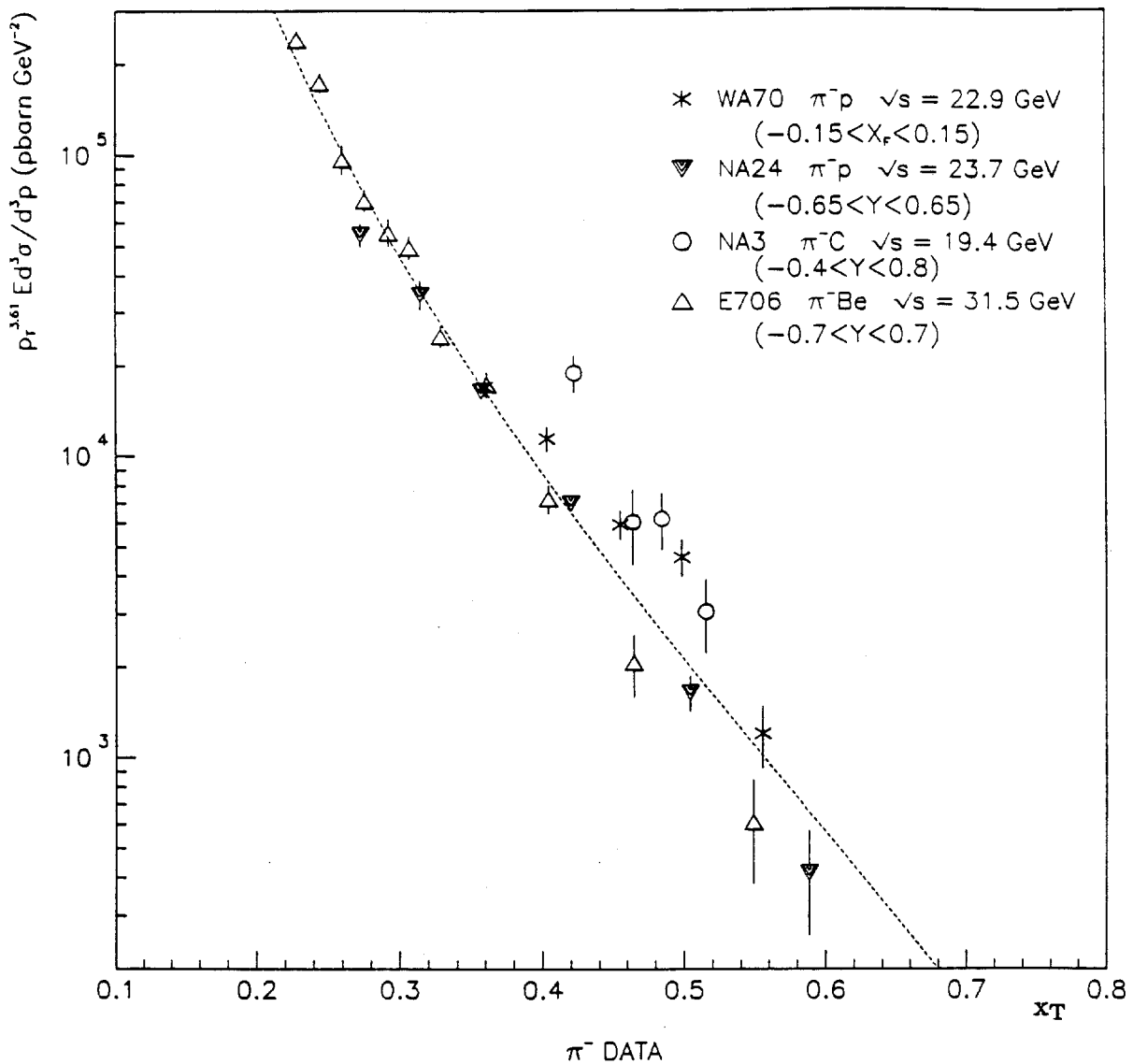


Figure 63 – Comparison of direct photon production from incident π^- . Cross-sections have been scaled in an attempt to cancel \sqrt{s} dependence.

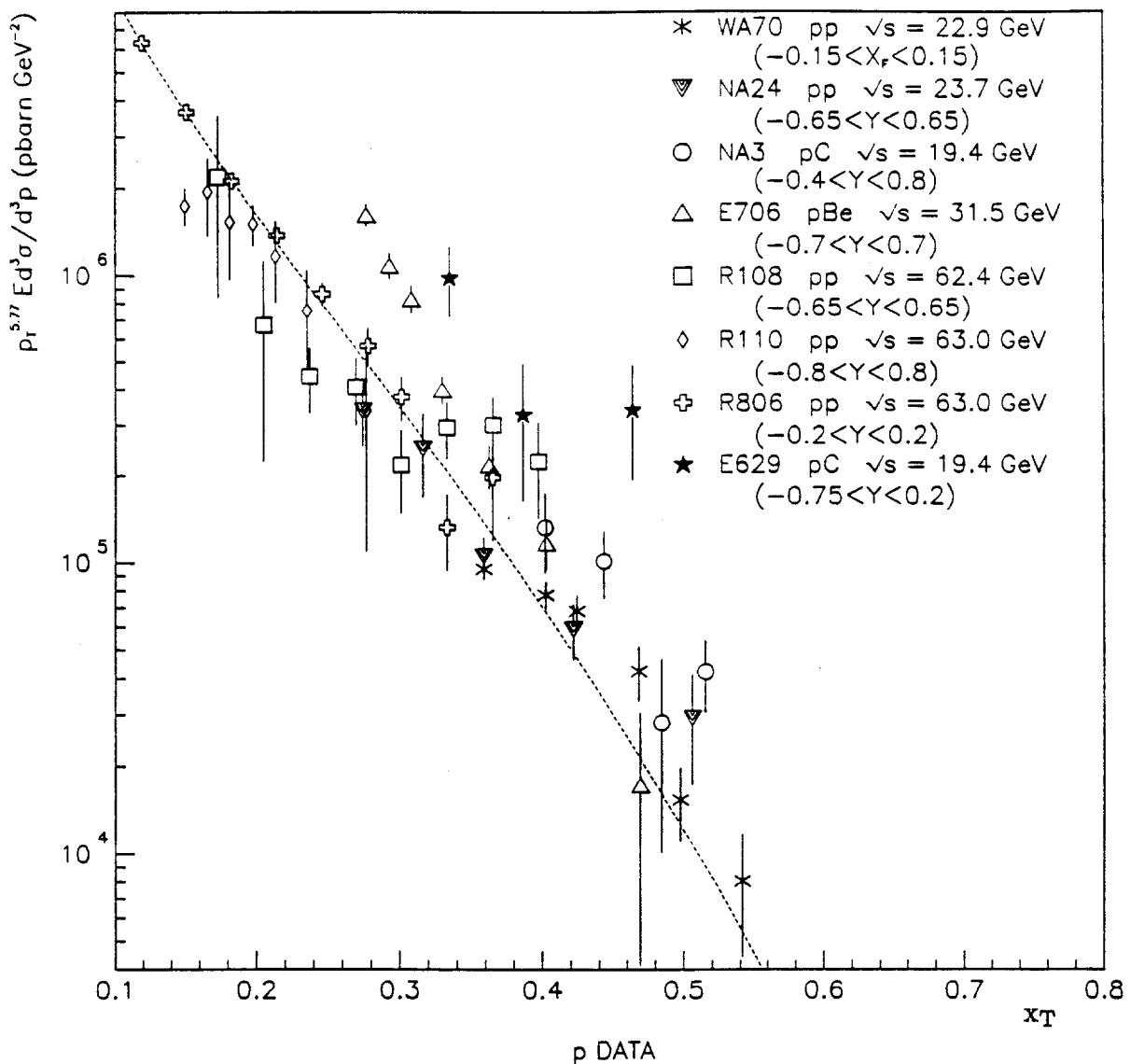


Figure 64 – Comparison of direct photon production from incident proton. Cross-sections have been scaled in an attempt to cancel \sqrt{s} dependence.

One explanation for this discrepancy is that nuclear effects are involved. Notice that in both plots, other data from nuclear targets are systematically high, relative to the data from hydrogen targets or pp colliders. Of course, only NA3 and E629 have reported cross-sections for direct photon production from nuclear targets. These were both relatively low statistics experiments, so it is unclear what conclusions, if any, may be drawn from this comparison. Nevertheless the nuclear target is the most obvious difference between the E706 experimental configuration and the other high-statistics experiments.

8.6 COMPARISON WITH QCD

Next to leading order ($O(\alpha_s^2)$) direct photon cross-section calculations have been available for some time^[47]. In order to predict actual measurements, one must make some assumption as to the relationship between the momentum transfer Q^2 , used in the evaluation of α_s , and in the factorization of the structure functions, and p_T , as measured in the experiment.

One method is to assume a simple $Q = c \times p_T$ scaling. Figure 65 shows a comparison between the measured direct photon cross-section per nucleon for π^- on beryllium, and theoretical predictions using $Q = .5p_T$ *. In this case, structure functions are to order α_s^2 , as calculated by Duke and Owens^[48]. Set 1 structure functions were calculated with Λ , as used in the calculation of α_s , equal to 200 MeV, while Set 2 points were calculated with $\Lambda = 400$ MeV. In both theoretical curves, the p_T dependence is less steep than that of the data. In the lower p_T range, the measured cross-section is about a factor of three higher than the Set 2 prediction and a factor of five higher than the Set 1 prediction. Changing the scale factor in the Q^2 definition shifts the scale of the prediction for both sets, but has little effect on the relative p_T dependence. In all likelihood, a functional form could be chosen for Q^2 which would fit the observed spectrum. However, such an ad-hoc definition would be of dubious significance. Figure 66 shows an analogous comparison for the $p + Be$ data. Again, the theory fails to

* All theoretical calculations were made using a program written by Patrick Aurenche.

predict the observed p_T dependence. This time the theoretical predictions are slightly higher than the measured values in the higher p_T range, but again the measured values exceed both sets of predictions for $p_T < 5$ GeV/c. We see that, within errors, both sets of predictions are roughly consistent with the data in the highest p_T range.

Another method of defining Q^2 is offered by the Principle of Minimum Sensitivity (PMS)^{[49][50][51]} whereby the factorization and the renormalization scales are chosen at each point such that the sensitivity of the result to this choice is minimized. The rationale for this is that if the calculation were done to all orders, the result would be completely independent of the choice of these scales.

Figure 67 shows attempts to predict the measured $\pi^- + Be$ cross-sections using PMS optimization for the Q^2 scales. Again, the predictions with Duke-Owens Set 1 and Set 2 structure functions are both shown. In both cases, the predictions are similar to those for $Q = .5p_T$ in the high- p_T region, rising slightly faster with falling p_T . Notice that there are no predictions for the lower p_T region. For these points an optimized scale could not be found for Q^2 . The predictions of Duke-Owens set 2 seem to match the data quite well in the range where PMS scaling worked. However, because the lowest p_T prediction is just above the point where the optimization fails, the interpretation of this is unclear.

Figure 68 shows the PMS predictions for the $p + Be$ data. In this case, the optimized predictions are slightly higher than those of the $Q = .5p_T$ model. The data lie between the two predictions in the intermediate p_T range. For $p_T < 5$ GeV/c, optimization again failed for the Set 1 case.

To summarize, all of the theoretical predictions were in rough agreement with the data in the highest p_T regions. None predicted the steeper p_T dependence of the observed cross-sections, and so underestimated the measured signal at low p_T . Returning to the issue of nuclear dependence, the theoretical calculations made no provision for the nuclear effects, and simply represented the target by the appropriate number of protons and neutrons.

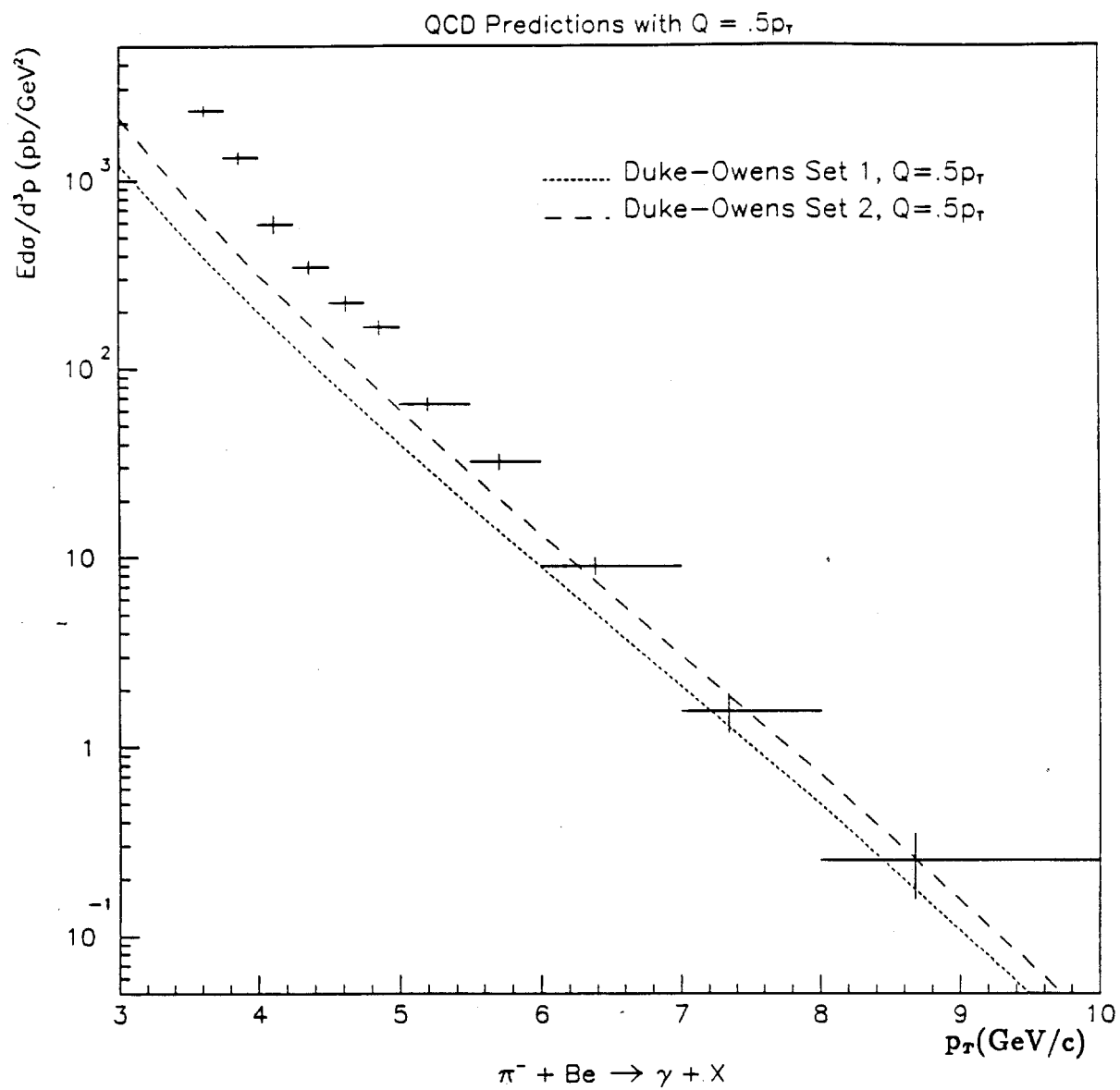


Figure 65 – QCD predictions for $\pi^- + Be \rightarrow \gamma + X$ with arbitrary scaling ($Q = .5p_T$).

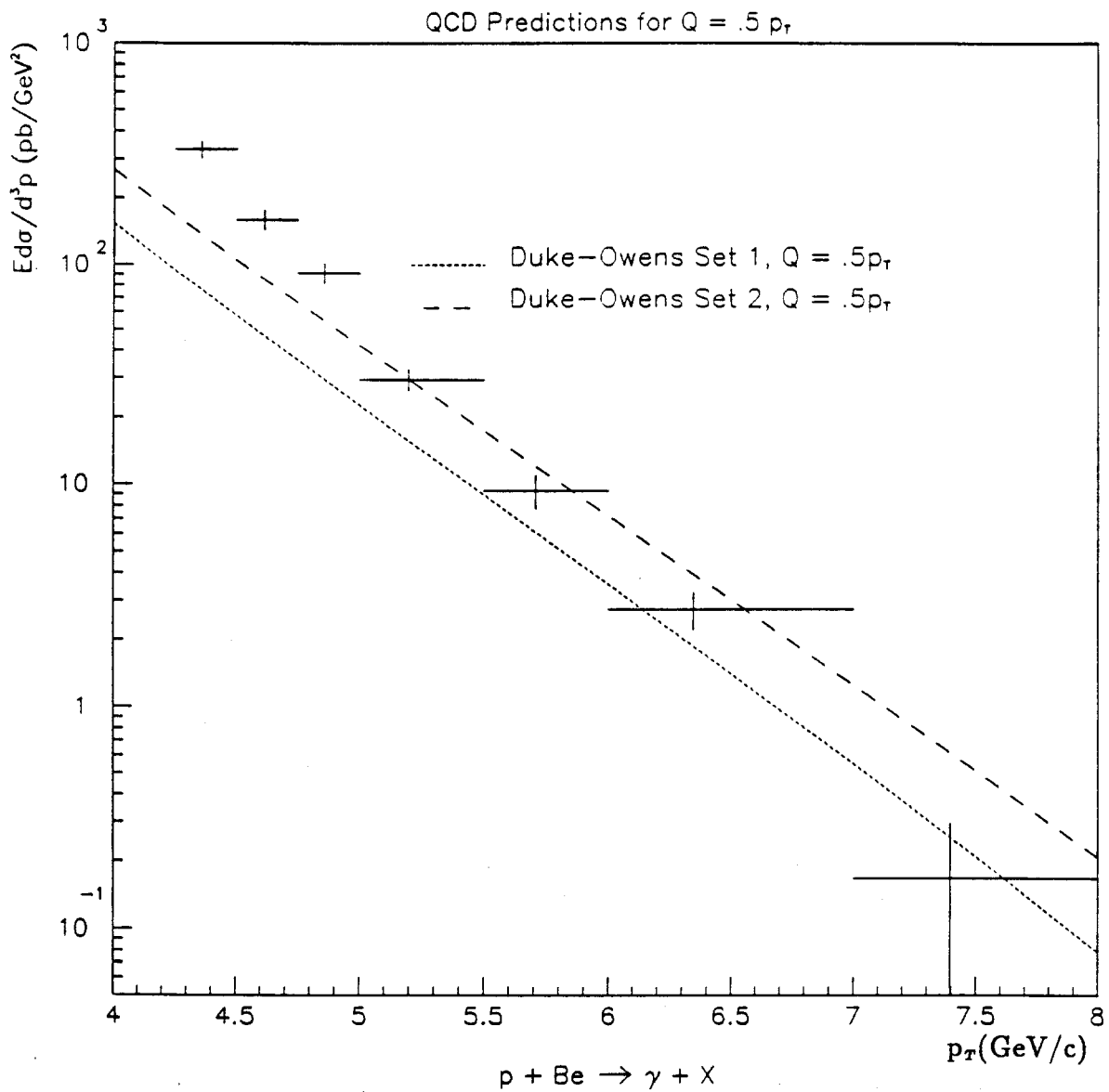


Figure 66 – QCD predictions for $p + Be \rightarrow \gamma + X$ with arbitrary scaling ($Q = .5 p_T$).

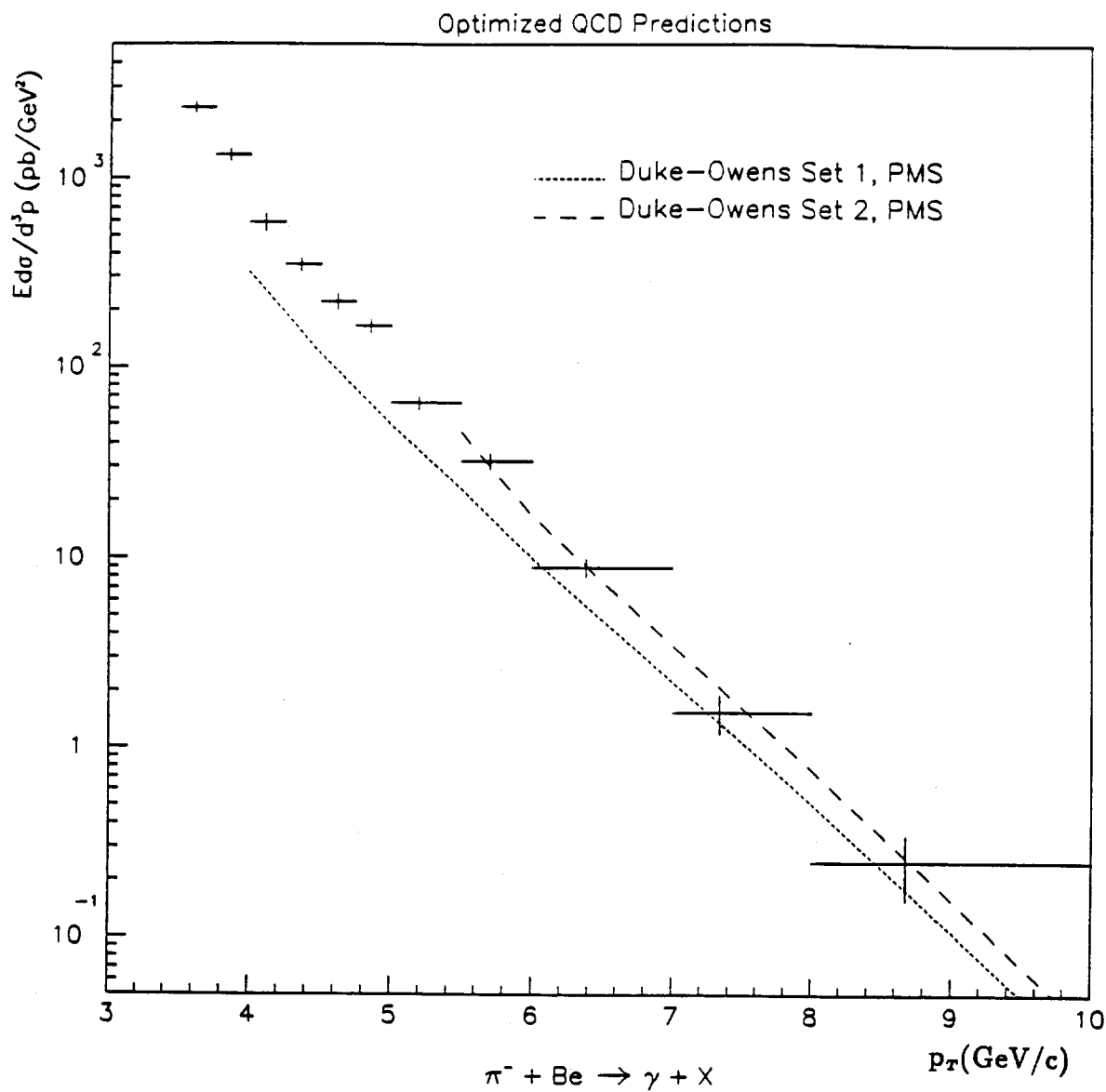


Figure 67 – QCD predictions for $\pi^- + Be \rightarrow \gamma + X$. In this case, the Q^2 dependence has been determined using PMS optimization.

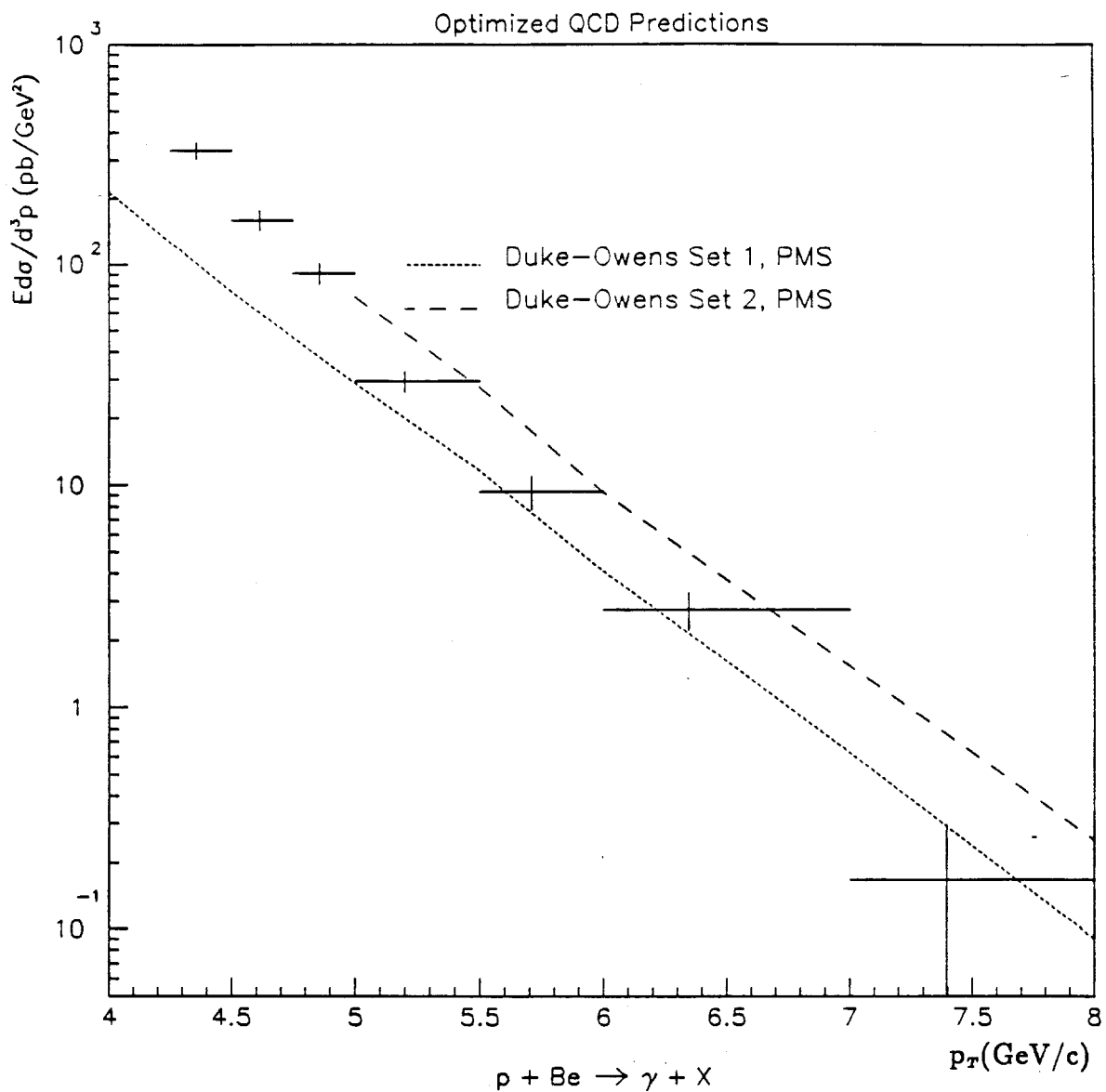


Figure 68 – QCD predictions for $p + Be \rightarrow \gamma + X$. In this case, the Q^2 dependence has been determined using PMS optimization.

9. Summary

Measurements of the inclusive cross-section per nucleon have been made for 530 GeV/c π^- and proton beams incident on copper and beryllium targets. Cross sections were in the region $3.5 < p_T < 10.0$ GeV/c for the data from incident π^- and $4.25 < p_T < 8.0$ GeV/c in the case of incident proton. All results were averaged over the rapidity interval $-.7 < y < .7$. The ratio of the direct photon cross-section to the measured π^0 cross-section was seen to be on the order of 10% in the lower p_T range, rising steeply for $p_T > 5.5$ GeV/c in the case of π^- beam on beryllium to a value on the order of 1 at $p_T \approx 9.0$ GeV/c. Some indication of a rise with p_T was seen for the other reactions studied, but statistics were limited for the higher p_T points.

The ratio of the invariant cross-sections per nucleon for direct photon production from copper and beryllium targets was measured for both types of incident beam. In the case of π^- beam, this was found to have an average value $.69 \pm .09$ with no obvious p_T dependence over the range $3.5 < p_T < 10.0$ GeV/c. For incident proton beam the average value was $.80 \pm .12$ over the range $4.25 < p_T < 8.0$ GeV/c, again with no obvious p_T dependence. Assuming an atomic number dependence of the form A^α , these ratios correspond to α values of $.81 \pm .07$ and $.89 \pm .08$ respectively. These results would seem to indicate coherent nuclear effects.

In comparing data from incident π^- and proton beams on beryllium, the ratio of the cross-section for direct photon production from $\pi^- + Be$ to the cross-section from $p + Be$ was seen to rise with increasing p_T , from a value near 1 at $p_T \approx 4.5$ GeV/c to a value on the order of 4 at $p_T \approx 7$. This is the behavior one would expect, based on the fact that the average momentum carried by individual partons is higher in the case of π^- beam than proton beam.

A phenomenological scaling was applied in an attempt to compare these results to previous experiments as a function of $x_T \equiv 2p_T/\sqrt{s}$. In the case of the incident π^- data, this showed qualitative agreement between this experiment

and previous results. In the case of the incident proton data, the cross-sections measured in this experiment showed a steeper dependence on p_T than the previous results, ultimately showing an excess of data in the low p_T regions. Most of the previous incident proton data were taken with hydrogen targets or in pp colliders. In general, previous data involving nuclear targets also tended to deviate from this scaling, but not in a way obviously consistent with the E706 data.

Next to leading order ($O(\alpha_s^2)$) predictions were tested against the data from the beryllium target for both beam signs. These predictions were made using both optimized Q^2 scaling (PMS) and a naive $Q = .5p_T$ model. In each of these cases, both Duke-Owens Set 1 and Duke-Owens Set 2 standard structure functions were tested. Although the predictions all tended to be in rough agreement with the data in the higher p_T regions, none of the predictions were in very persuasive agreement with the measured cross-sections over any large fraction of p_T range studied, and none predicted the large cross-sections measured in the lower p_T region.

To summarize, direct photon cross-sections measured in this experiment showed a steeper p_T dependence than was expected based on theoretical predictions and the extrapolation of previous experimental results. Measured values significantly exceeded expectations for $p_T < 5.5$ GeV/c. At the present time, we attribute this to nuclear effects, which have never been accurately measured for direct photon data. We look forward to the next run of E706, which, in addition to the nuclear targets, will implement a hydrogen target, thus enabling more direct comparison with previous experiment, as well as conclusive measurement of nuclear dependence.

REFERENCES

1. J.F. Owens, *Rev. of Mod. Phys.* **59** (1987), 465.
2. M. Fritzsh and M. Minkowski, *Phys. Lett.* **B69** (1977), 316.
3. T. Ferbel and W.R. Molzon, *Rev. Mod. Phys.* **56** (1984), 181.
4. Aguilar-Benitez, *et al.* (Particle Data Group), *Particle Properties Data Booklet* (1988), 13.
5. Aguilar-Benitez, *op. cit.*, 14.
6. D. Skow, Ph.D. Dissertation, University of Rochester (1990), 130.
7. P. Darriulat, *et al.*, *Nucl. Phys.* **B110** (1976), 365.
8. E Amaldi, *et al.*, *Phys. Lett.* **B77** (1978), 240.
9. R. Baltrusaitis, *et al.*, *Phys. Lett.* **B88** (1979), 372.
10. M. McLaughlin, *et al.*, *Phys. Rev. Lett.* **51** (1983), 971.
11. J. Badier, *et al.*, *Z. Phys.* **C31** (1986), 341.
12. C. De Marso, *et al.*, *Phys. Rev.* **D36** (1987), 8.
13. M. Bonesini, *et al.*, *Z. Phys.* **C37** (1988), 535.
14. G. Zioulas, American Physical Society Meeting, Baltimore, May 1989.
15. A. Bernasconi, *et al.*, *Phys. Lett.* **B206** (1988), 163.
16. A.L.S. Angelis, *et al.*, *Phys. Lett.* **B94** (1980), 106.
17. C.W. Salgado-Galeazzi, Ph.D. Dissertation, Michigan State University (1988).
18. E. Annassontzis, *et al.*, *Z. Phys.* **C13** (1982), 277.
19. T. Akesson, *et al.*, *Phys. Lett.* **B158** (1985), 282.
20. J.A. Appel, *et al.*, *Phys. Lett.* **B176** (1986), 239.
21. C. Albajar, *et al.*, *Phys. Lett.* **B209** (1988), 385.

22. H. Frisch, *XIX International Symposium on Multiparticle Dynamics, Arles, France*, 1988.
23. W. Desoi, Ph.D. Dissertation, University of Rochester (1990), 27.
24. W.J. Willis and V. Radeka, *Nucl. Inst. and Meth.* **120** (1974), 221.
25. E. Prebys and F. Lobkowicz, *E706 Internal Note* **163** (1988).
26. L.S. Miller, *et al.*, *Phys. Rev.* **166** (1968), 871.
27. W. Desoi, *op. cit.*, 153.
28. R. Benson, Ph.D. Dissertation, University of Minnesota (1989).
29. E. Engels Jr., *et al.*, *Nucl. Inst. and Meth. in Phys. Res.* **A253** (1987), 523.
30. S. Easo, Ph.D. Dissertation, Pennsylvania State University (1989), 106.
31. I. Kourbanis, Ph.D. Dissertation, Northeastern University (1989).
32. G. Drake, *et al.*, *Nucl. Inst. Meth. in Phys. Res.* **A269** (1988), 68.
33. *Multi Wire Proportional Chamber Readout System - MWPC-1*, Nanometric Systems, Inc., Oak Park, IL.
34. *CAMAC Instrumentation and Interface Standards*, IEEE 1982, ISBN 0-471-89737-X.
35. R. Brun, *et al.*, *ZEBRA User's Guide*, CERN Computer Centre Program Library DD/EE/85-6.
36. *ACP Software User's Guide for Event Oriented Processing*, FNAL Computer Department Publication # GA0001.
37. J. Mansour, Ph.D. Dissertation, University of Rochester (1990), 46.
38. S. Easo, *op. cit.*
39. J. Huston, *private communication*.
40. J. Mansour, *op. cit.*, 79.

41. R. Brun, *et al.*, *GEANT3 User's Guide*, CERN Data Handling Division, DD/EE/84-1 (1987).
42. P. Lukens, *private communication*.
43. J. Mansour, *op. cit.*
44. D. Skow, *op. cit.*
45. A. Lanaro, Ph.D. Dissertation, University of Rochester (1989), 176.
46. P. Aurenche and M. R. Whalley, *A Compilation of Data on Single Prompt Photon Production in Hadron-Hadron Interactions*, Fermilab Library Preprint RAL-89-106 (1989), 38.
47. P. Aurenche, *et al.*, *Phys. Lett.* **140B** (1984), 87.
48. D.W. Duke and J.F. Owens, *Phys. Rev.* **D30** (1984), 49.
49. P.M. Stevenson, *Phys. Rev.* **D23** (1981), 2916.
50. P.M. Stevenson, *Nucl. Phys.* **B203** (1982), 472.
51. P.M. Stevenson, H.D. Politzer, *Nucl. Phys.* **B277** (1986), 758.